Speed Effects on Moving Cracks in Nonlinear/Ductile Materials

by

Jian Wu

A thesis submitted in partial fulfillment of the requirements for the degree of

Doctor of Philosophy

Department of Mechanical Engineering
University of Alberta

Abstract

Speed effects on moving cracks in ductile or nonlinear materials are studied with newly developed theoretical models in the present thesis. Speed-dependent stress field, traction distribution and fracture energy are discussed in detail in four chapters.

1) An asymptotic analysis near the tip of a steady-state moving crack in a compressible hyperelastic material is given based on a finite plane strain model. The crack tip deformation and stress fields are derived up to the third order which meets the strict positivity of Jacobian determinant in the vicinity of the moving crack tip. Comparison with the experimental data shows that the crack-face profile and the energy release rate predicted by the present model are in reasonable agreement with experiments and several recent nonlinear elastic models. In addition, the crack branching angle predicted by the present model also agrees well with some known experimental data.

2) Steady-state moving crack under mode-I loading is studied with a modified cohesive zone model which addresses speed-dependent role of the normal stress parallel to the crack axis and the non-uniformity of traction force in cohesive zone. Unlike the classical Dugdale model which predicts independence of the cohesive zone length on crack speed, the present modified model predicts that the cohesive zone length strongly depends on crack speed. Comparison with some known experimental data suggests that the present modified model has the potential to capture the speed effects on moving cracks in ductile materials especially at high crack speed.

3) The modified cohesive zone model is then applied to a self-similar high-speed expanding crack problem. Numerical results show that the normal stress parallel to the crack face increases with increasing crack speed and can be even larger than the normal traction in the cohesive zone,

which justifies the necessity of including the normal stress parallel to the crack faces in the yielding condition at high crack speed. Strain hardening effect is also examined based on a non-uniform traction distribution given by a polynomial whose coefficients are to be determined as part of the solution.

4) A simple mass-spring model is presented to study inertia effect of cohesive zone for a Yoffe-type mode-I steady-state moving crack of constant length. Traction distribution surrounding the cohesive zone and fracture energy at high crack speed are solved numerically by a proposed numerical method. Results show that fracture energy predicted by the present model increases significantly at high crack speed, which defines a limiting crack speed above that fracture energy tends to infinity. Reasonable agreement with some known experimental data suggests that the present model has the potential to catch inertia effect of cohesive zone of a high-speed moving crack which has not been considered by existing cohesive zone models.

The theoretical models and numerical results achieved in this thesis contribute new ideas and insights into the study of high-speed dynamic fracture of nonlinear and ductile materials, and some results predicted by the present models provide plausible explanations for a few important phenomena of moving cracks at high crack speed which have not been well explained by the existing models.

Preface

The main body of this thesis is composed by four published/unpublished journal papers. See below for details.

Chapter 2 of this thesis has been published as J. Wu and C.Q. Ru, Speed-dependent tip fields of a moving crack in a hyperelastic material, Mathematic and Mechanics of Solids, 2013 (18):285-300. I was responsible for all math derivations, results analysis and writing manuscript. C.Q. Ru is the supervisory author who presented the research topic, checked results, and revised the manuscript.

Chapter 3 of this thesis has been published as J. Wu and C.Q. Ru, A speed-dependent cohesive zone model for moving cracks with non-uniform traction force, Engineering Fracture Mechanics, 2014(117):12-27. I was responsible for presenting research topic, all math derivations, results analysis and writing manuscript. C.Q. Ru is the supervisory author who presented the research area, checked results, and revised the manuscript.

Chapter 4 of this thesis has been published as J. Wu and C.Q. Ru, A modified cohesive zone model for a high-speed expanding crack, Fatigue & Fracture of Engineering Materials & Structures, 2014 (online available). I was responsible for presenting research topic, all math derivations, results analysis and writing manuscript. C.Q. Ru is the supervisory author who presented the research area, checked results, and revised the manuscript.

Chapter 5 of this thesis has been submitted to Engineering Fracture Mechanics for review as J. Wu and C.Q. Ru, Inertia effect of cohesive zone on a high-speed moving crack. I was responsible for all math derivations, results analysis and writing manuscript. C.Q. Ru is the supervisory author who presented the research topic, checked results, and revised the manuscript.

Acknowledgements

I sincerely thank my supervisor Dr. Chongqing Ru for his guidance, support, advice, and encouragement. I am very thankful to all of my supervisory committee members, Dr. Peter Schiavone and Dr. Xiaodong Wang for their valuable suggestions on both my research and course studies. I would also like to thank NSERC for providing financial support during my PhD program.

Table of contents

List of figures

List of tables

Nomenclature

a^+	y-directional acceleration of the upper cohesive zone face
a_2, b_1, c_2	real constants measuring asymptotic finite deformation field
A_0, A_1,..., A_n	coefficients of polynomial traction function $P(x)$
$A(V)$	a function of crack speed
b	cohesive zone thickness parameter
B_0, B_1, ..., B_n	coefficients of polynomial function $Q(x)$
c	half length of a moving crack
c'	length of cohesive zone
C_d, C_s	longitudinal and transverse elastic wave speeds
C_R	Rayleigh wave speed
$f(u_y)$	inner traction inside the cohesive zone
$F(I)$	a real material response function
F_{11}, F_{12}, F_{21}, F_{22}	deformation gradients
F_{xx}, …, G_{xt}	eight analytic functions
G	dynamic fracture energy
G_0	static fracture energy
I, J	two scalar invariants
m	hardening parameter
$M(x)$	mass distribution of cohesive zone
M_1, M_2	real speed-dependent constants
r, θ	polar coordinates in the original plane
R, φ	polar coordinates in the transformed plane
$R_I(V)$, $R_I(V_a)$	Rayleigh wave function
$R_a(V)$	a function of crack speed
$P(x)$	a polynomial traction function
P_{11}, P_{12}, P_{21}, P_{22}	components of Piola stress tensor
$Q(x)$	a real polynomial function
s	the quantity $[1-\rho V^2/(2\mu_h)]^{1/2}$

S	a uniform speed-dependent traction force without hardening
S_0	speed-dependent traction force at initial yielding
S_{max}	maximum inner traction inside cohesive zone
S_y	normal traction surrounding cohesive zone
t	time coordinates
T	remote mode-I tensile loading
$T_1(\theta)$, $T_2(\theta)$, $T_3(\theta)$	real functions near crack tip
u_0	half of cohesive zone separation at the location of maximum traction
u_x, u_y	components of displacement vector
V	crack speed of a moving crack
V_a, V_c	crack tip speed and cohesive zone tip speed of an expanding crack
w	a complex variable with $w = y_1 + iy_2$
x', y'	coordinates in the fixed coordinate system
x, y	coordinates in the moving coordinate system
x_m	location of maximum traction in cohesive zone
x_1, x_2	moving coordinate system
X_1, X_2	initial coordinate in undeformed configuration
y_1, y_2	coordinate after deformation
Y	yielding stress of material
Y_0	initial yielding stress of material of hardening
y_d, y_s	coordinates in the transformed plane with $y_d = \beta_1 y$, $y_s = \beta_2 y$
z_1, z_2	complex variables with $z_1 = x+iy_d$, $z_2 = x+iy_s$
α, β	two material constants of harmonic material
β_1, β_2	the quantities $(1-V^2/C_d^2)^{1/2}$ and $(1-V^2/C_s^2)^{1/2}$
Δ	material ductility parameter
ζ, ζ_d, ζ_s	complex variables
κ	dimensionless elastic parameter defined by v
μ	elastic shear modulus
μ_h	a positive material constant of harmonic material
v	Poisson's ratio
ξ, η_1, η_2	rectangular coordinates in the transformed plane

ξ, η'	transformed coordinates system
ρ	mass density
σ_{xx}, σ_{xy}, σ_{yy}	components of stress tensor
σ_{11}, σ_{12}, σ_{22}	components of Cauchy stress tensor
ς, ψ	two wave functions
$\Phi(z_1)$, $\Psi(z_2)$	two analytic functions of z_1 and z_2
CTOD, δ	crack tip opening displacement
LEFM	linear elastic fracture mechanics
H(*)	Heaviside step function
T-S law	traction-separation law

Chapter 1: Introduction

1.1 Introduction

Crack growth is a common cause of material failure. The speed of crack propagation could be as high as 1000m/s in ductile fracture (Zehnder and Rosakis, 1990) and even higher in brittle materials (e.g., 1500m/s in glass (Anthony et al., 1970)), and the associated dynamic effects (such as inertia effect) can play a decisive role in both crack-tip field and fracture energy. For example, some recent experiments have shown that the crack-tip profiles of gels (Bouchbinder et al., 2008, 2010; Livne et al., 2010) and fracture toughness of structural steels (Rosakis and Zehnder, 1985; Zehnder and Rosakis, 1990) can strongly depend on crack speed, as shown in Fig. 1.1 and Fig. 1.2. In addition, at high crack speed, in brittle materials, crack branches and propagates along a direction inclined to its original path (Murphy et al., 2006); in ductile materials, a terminal crack speed is observed beyond that fracture energy G increases dramatically with crack speed (see Fig 1.3) (Rosakis and Zehnder, 1985). Unfortunately, by far, little effort has been made to investigate the above-mentioned high-speed related phenomena in dynamic fracture of nonlinear and ductile materials and little has been known about how crack speed affects the crack-tip field and fracture energy at high crack speed.

The present thesis aims to develop new theoretical models (such as modified cohesive zone models or hyperelastic model) for high-speed moving cracks, to study the effect of crack speed on crack-tip field and fracture energy and explore its implications to dynamic fracture of nonlinear and ductile materials. Incorporating the inertia effect in newly developed models, speed-dependent crack-tip field and fracture energy are studied in detail in the following 4 chapters, and high-speed related phenomena such as crack branching and dramatically increasing fracture energy with increasing high crack speed are examined for nonlinear and ductile materials.

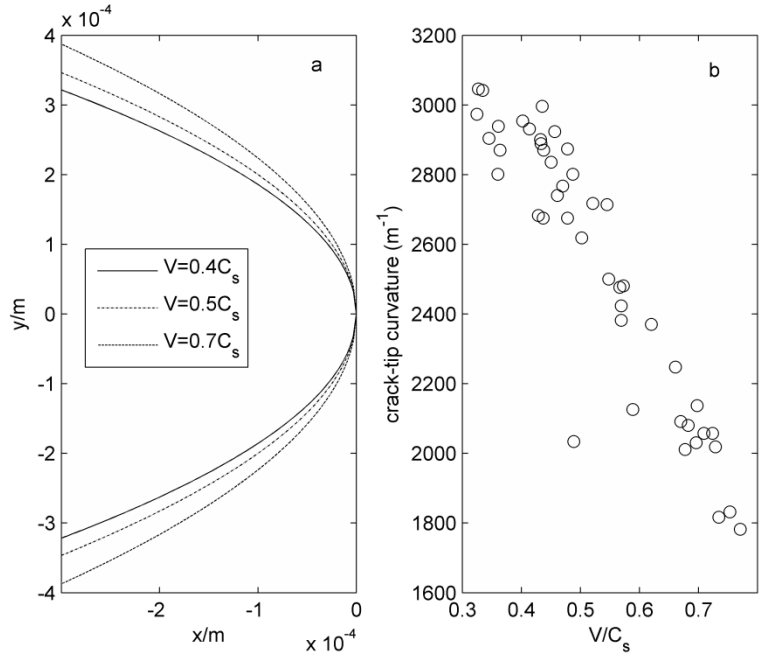

Fig. 1.1 The dependence of crack-tip profiles on crack speed V for gels (Livne et al., 2010). Fig. 1.1a shows crack-tip profiles at different crack speed and Fig. 1.1b shows that the crack-tip curvature decreases with increasing crack speed. C_s is the transverse elastic wave speed.

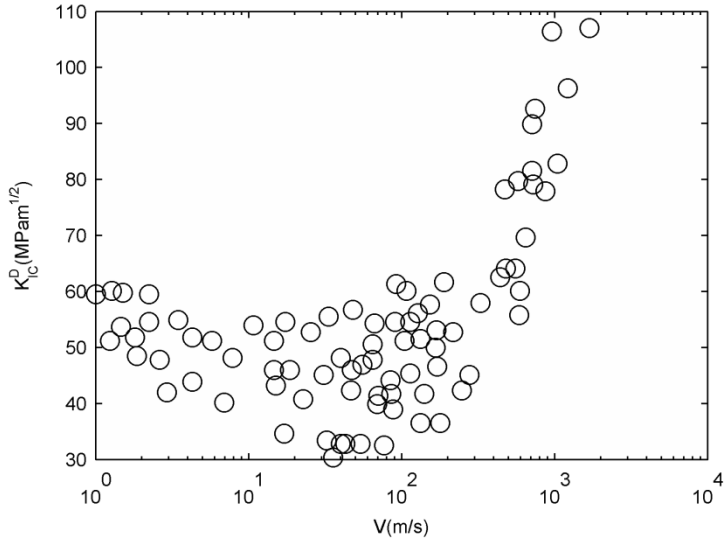

Fig. 1.2 The dependence of fracture toughness K^D_{IC} on crack speed V for structural steels (Rosakis and Zehnder, 1985). K^D_{IC} is the dynamic stress intensity factor at which crack starts to propagate.

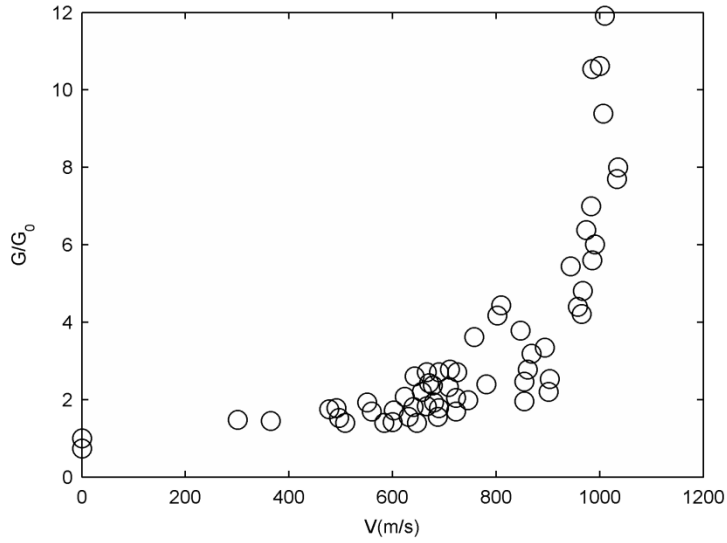

Fig. 1.3 The fracture energy of structural steels G increases dramatically when crack speed V > 900m/s (Zehnder and Rosakis, 1990). G_0 is the fracture energy at $V = 0$.

1.2 Linear elastic models for moving cracks

Linear elastic fracture mechanics (LEFM) (Irwin, 1957; Williams, 1957), which predicts an inverse square root singularity of stress field near a static crack tip, is the most common tool in fracture analysis and has been successfully extended to a moving crack by Yoffe (Yoffe, 1951), who studied a steady-state moving crack of constant length in an infinite elastic media. Furthermore, Craggs (Craggs, 1960) studied a semi-infinite steady-state moving crack using complex variable methods. A self-similar crack expanding at both tips from zero initial length was studied by Broberg (Broberg, 1960) using Fourier transformation and by Craggs (Craggs, 1963) based on dynamic similarity. In addition, Rice (Rice, 1968) derived an asymptotic solution near a propagating crack tip using Williams eigen-expansion method (Williams, 1957). In these studies, under mode-I remote loading, the crack-tip stress field can be given by

$$\sigma_{ij} = \frac{K_I(t)}{\sqrt{2\pi r}} f_{ij}^I(\theta, V) + O(1), \qquad r \to 0, \qquad i = x, y, \qquad j = x, y \tag{1.1}$$

where, r is distance to crack tip and θ is the associated angle inclined to x-axis (see Fig. 1.4), $K_I(t)$ is the stress intensity factor at time t under mode-I remote loading, and f_{ij}^I are universal functions of θ at crack speed V and their specific value can be found in (Freund, 1990).

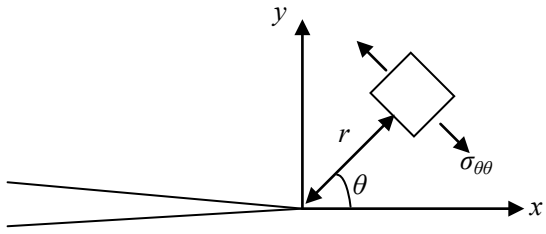

Fig. 1.4 Hoop stress $\sigma_{\theta\theta}$ at crack tip.

In addition, the hoop stress is

$$\sigma_{\theta\theta} = \sigma_{xx} \sin^2 \theta + \sigma_{yy} \cos^2 \theta - 2\sigma_{xy} \sin\theta \cos\theta \tag{1.2}$$

Thus, taking Eq. (1.1) into (1.2), based on LEFM, it is found that when crack speed exceeds about 0.6 of elastic transverse wave speed, the singular hoop stress near the mode-I crack tip is no longer maximized at its original propagation direction, instead the hoop stress is maximized at an angle inclined to the crack faces, which could define a crack branching angle (Yoffe, 1951). However, this predicted branching angle of about 60^o (Craggs, 1960) is clearly larger than experimental results of about 25^o for PMMA (Murphy et al., 2006) and Homalite-100 (Ramulu et al., 1984) and about 30^o for bursting steels (Ramulu et al., 1982).

1.3 Hyperelastic models for moving cracks

At the actual crack tip, nonlinear or plastic deformation is dominant. Indeed, a nonlinear zone near a moving crack tip is observed in recent experiments (Livne et al., 2010). As a consequence, some results such as crack-tip deformation field given by LEFM are in direct contradiction with experimental data of a moving crack tip for some brittle materials (Bouchbinder et al., 2008, 2010; Livne et al., 2010).

Different than linear elastic models which neglect the second-order terms of Lagrangian

finite strain tensor and are limited to small strain condition, hyperelastic models account for higher order terms of Lagrangian strain tensor and can be applied in large deformation problems, thus provide a theoretical tool to study deformation field near a crack tip. From the definition of elastic materials, the Piola stress **P** in undeformed configuration is equal to the derivative of strain energy density function W with respect to deformation gradient tensor **F**

$$\mathbf{P} = \frac{\partial W}{\partial \mathbf{F}} \tag{1.3}$$

And the Cauchy stress in deformed configuration is given by

$$\boldsymbol{\sigma} = \frac{1}{J}\frac{\partial W}{\partial \mathbf{F}}\mathbf{F}^{\mathrm{T}} \tag{1.4}$$

where, J is the determinant of deformation gradient tensor **F** and measures the volume change after deformation, $\mathbf{F}^{\mathrm{T}}$ is the transpose of **F**. Based on different definitions of strain energy density function W, different types of hyperelastic models are developed, such as Mooney-Rivlin model (Mooney, 1940; Rivlin, 1948), Neo-Hookean model (Knowles and Sternberg, 1983) and Harmonic model (John, 1960) which is employed in chapter 2 of this thesis.

Since finite deformation near crack tips is often involved in brittle fracture, Hyperelastic models have drawn considerable attentions and have the potential to predict a more reasonable crack-tip field compared with LEFM. For example, it is well known that LEFM predicts oscillatory singularities at an interface crack tip which lead to physically inadmissible interpenetration of crack faces (England, 1965). To remove this physically inadmissible result, hyperelastic models have been successfully developed in static interface crack problem (Geubelle, 1995; Geubelle and Knauss, 1994; Knowles and Sternberg, 1975, 1983; Ru, 1997; Ru, 2002). Recently, a few hyperelastic models were employed to investigate dynamic fracture at finite deformation of nonlinear elastic materials. For instance, Tarantino (Tarantino, 2005) derived a second-order asymptotic stress field near a moving crack tip in a compressible Mooney-Rivlin material. A Moving crack in an incompressible Neo-Hookean material was studied by Livne et al. (Livne et al., 2010) and the obtained theoretical crack-tip field is in good agreement with experimental data.

1.4 Cohesive zone models for moving cracks

To account for the plastic or nonlinear deformation near the crack tip, cohesive zone models were first presented by Barenblatt (Barenblatt, 1959) and Dugdale (Dugdale, 1960) for static cracks. In the concept of cohesive zone models, a fracture process zone with zero thickness is defined collinear with (or inclined to) actual crack faces (see Fig. 1.5). The constitutive relation in cohesive zone representing real mechanical behaviour such as strain hardening and softening are defined separately from surrounding bulk materials.

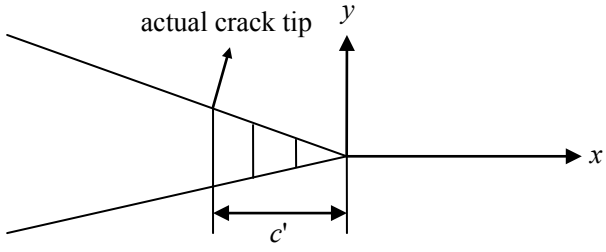

Fig. 1.5 A cohesive zone of length c' near a semi-infinite crack tip.

The traction on cohesive zone, which prevents the crack to propagate, results in a negative singular stress near the cohesive zone tip. Thus, the length of cohesive zone c' can be determined by the stress singularity cancelation condition. And the fracture energy G dissipated in cohesive zone is given by (Embley and Sih, 1972)

$$G = \frac{2}{V}\int_{-c'}^{0} S_y \frac{\partial u}{\partial t}\mathrm{d}x \tag{1.5}$$

where, S_y is the traction in cohesive zone, V is the crack speed, t is the time and u is the displacement of cohesive zone faces (x-directional for mode-II loading and y-directional for mode-I loading).

Supported by reasonable agreement with experimental data (Dugdale, 1960) and its great potential in numerical simulations (Needleman, 1987; Xu and Needleman, 1994), the cohesive

zone model has become one of the most popular nonlinear models for fracture analysis of nonlinear and ductile materials. For elastic-perfectly plastic materials under mode-I remote loading, Dugdale (Dugdale, 1960) assumed that the plastic deformation is confined to a line strip collinear with the actual crack and the normal traction on plastic strip is equal to the yielding stress of the material. Thus the length of confined strip, which represents plastic zone size, is found to depend on the yielding stress, crack length, and remote loading. The cohesive zone model was first extended to dynamic fracture by Goodier and Field (Goodier and Field, 1963) for a semi-infinite steady-state moving crack. Atkinson (Atkinson, 1968) determined the cohesive zone length near a self-similar expanding crack tip. A steady-state moving crack was studied by Kanninen (Kanninen, 1968). In these studies, a common key assumption is that the normal traction on cohesive zone is equal to the yielding stress of the material and independent of crack speed.

Different value of uniform traction force was studied by Becker and Gross (Becker and Gross, 1988) for a multiaxial loading fracture problem by assuming that the constitutive relation in cohesive zone is governed by von Mises criterion. Yao and Huang (Yao and Huang, 2011) established a relation between the uniform traction force and crack tip opening displacement (CTOD) based on nonlocal continuum mechanics. Instead of considering the cohesive zone collinear with the actual crack, inclined strip yielding models were studied in (Atkinson and Kanninen, 1977; Rice, 1974; Vitek, 1976).

Strain hardening in cohesive zone near a static crack tip was studied in (Daniewicz, 1994; Harrop, 1978; Isherwood and Williams, 1970; Siegmund and Brocks, 2000; Theocaris and Gdoutos, 1974) by assuming that the traction force is an unknown function of the coordinate in the cohesive zone. Alternatively, nowadays, with the development of computer power and numerical techniques, the traction are commonly defined by a function of separation of cohesive zone faces and the associated traction-separation law (T-S law) defining strain hardening in cohesive zone are widely employed in both analytic analysis (Kubair et al., 2002; Zhang et al., 2003) and numerical simulations (Needleman, 1987; Tvergaard and Hutchinson, 1994; Xu and

Needleman, 1994; Zhou et al., 2005) of moving cracks. The T-S law is thought to be a material property and its implication to ductile fracture has been studied recently. For example, Williams and Hadavinia (Williams and Hadavinia, 2002) considered the maximum value of traction and the separation work as two major parameters characterizing the cohesive zone model, while the shape of T-S law is considered as secondary importance. However, Volokh (Volokh, 2004) showed that the shape effect of the T-S law significantly affects the fracture energy in cohesive zone through a block-peel test. The link between T-S law of a macro crack and the nucleation and growth of micro voids is established by Siegmund and Brocks (Siegmund and Brocks, 2000) and Scheider (Scheider, 2009) via Gurson model (Gurson, 1977).

The constitutive relation in cohesive zone is also influenced by other factors. For instance, the effect of specimen thickness and in-plane constraint on traction force on cohesive zone was studied by Neimitz (Neimitz, 2004). Thermal effect in cohesive zone was studied by Costanzo and Walton (Costanzo and Walton, 2002) for a steady-state moving crack. Strain rate effect was studied by Kanninen (Kanninen, 1968) with a uniform rate-dependent traction force for a mode-I steady-state moving crack, Kubair et al. (Kubair et al., 2002) with a strain softening model for a mode-III steady-state moving crack, and Zhang et al. (Zhang et al., 2003) with a strain hardening-softening model for a mode-I steady-state moving crack.

1.5 Limitations of the existing models

In recent years, although hyperelastic models and cohesive zone models have drawn considerable attention and been extensively applied for static cracks in nonlinear and ductile materials, little attention has been paid to the studies on moving cracks. Actually, a number of key questions have remained unanswered regarding the speed effect on high-speed fracture of nonlinear and ductile materials. In particular,

1) the speed dependence of crack tip field and energy release rate on crack speed in

hyperelastic materials are not well studied. For example, compared with experimental value of crack branching angle of about 25^o for PMMA (Murphy et al., 2006) and Homalite-100 (Rosakis and Zehnder, 1985) and about 30^o for bursting steels (Ramulu et al., 1982) , LEFM predicts a much larger crack branching angle of about 60^o (Craggs, 1960), and little effort has been made to resolve this discrepancy between LEFM and experiment;

2) the dependence of fracture energy on crack speed for ductile and nonlinear materials, especially the dramatically increasing fracture energy at high crack speed, is not well explained by the existing cohesive zone models. To better understand the high-speed fracture in nonlinear and ductile materials, refined cohesive zone models are needed which account for high-speed effect (particularly inertia effect) more carefully, for example,

2.1) in existing cohesive zone models for mode-I moving cracks, the traction force on the cohesive zone is usually assumed to be uniform and equal to the yielding stress of the material and the influence of normal stress parallel to the crack axis is completely ignored (Atkinson, 1968; Goodier and Field, 1963; Kanninen, 1968). At high crack speed, however, inertia effect significantly influences crack tip stress state (Freund, 1990). As a result, other stress components, especially the normal stress parallel to the crack axis, could come to play an important role in the cohesive zone. By far, the speed-dependent role of the normal stress parallel to the crack axis and its implication to the cohesive zone models remains unclear; in particular, speed-dependent crack tip field and fracture energy of a self-similar expanding crack at high crack speed raise even more challenging research topics;

2.2) in existing cohesive zone models, the cohesive zone is simplified as a line segment without a volume and mass. Since the cohesive zone actually represents a region near the crack tip in which plastic or nonlinear deformation dominates (Livne et al., 2010; Rosakis and Freund, 1982), the inertia of this region, which has been ignored in the previous existing cohesive zone models, could have a significant effect on dynamic fracture. It is of great interest to study the inertia effect of cohesive zone on high-speed moving cracks in nonlinear and ductile materials.

1.6 Objectives of the thesis

Dynamic fracture of nonlinear and ductile materials is an important topic in engineering design and material selection. When crack propagates at high speed, the dynamic effect, particularly the inertia effect, will come to play a decisive role. Despite the practical importance, as mentioned in section 1.5, the speed effects on crack-tip field and fracture energy, as well as its implication to dynamic fracture of nonlinear and ductile materials have not been well addressed in the literature. Aiming at investigating the role of crack speed in dynamic fracture of nonlinear/ductile materials, my research is to achieve the following objectives:

1) achieve a finite plane strain analysis of a high-speed moving crack in a compressible hyperelastic material and, particularly, study the speed effect on fracture energy and achieve a crack branching angle in reasonable agreement with experimental results;

2) develop a more accurate speed-dependent cohesive zone model which accounts for the effect of normal stress parallel to the crack-faces and strain hardening-caused non-uniform traction, and use the developed model to investigate speed-dependent traction and fracture energy for a steady-state moving crack of constant length;

3) similarly, develop speed-dependent cohesive zone models for a self-similar expanding crack, and investigate the difference between a Yoffe-type steady-state moving crack of constant length and a self-similar expanding crack in a ductile material;

4) develop a cohesive zone model which accounts for the inertia of cohesive zone, in particular, use the developed model to investigate limiting terminal crack speed above that fracture energy tends to infinity.

1.7 Thesis layout

Inspired by the above-mentioned limitation of existing models, more accurate models will

be developed in the present thesis to study high-speed moving cracks in nonlinear and ductile materials, and the obtained theoretical predictions will be discussed with comparison to known experiment data available in the literature. The present thesis is organized as follows:

Chapter 1 provides a general introduction of the involved research topics, the limitations of the existing models and the objectives of my research.

Chapter 2 derives a third-order asymptotic stress field near a moving crack tip based on a plane strain hyperelastic model of harmonic materials. Speed-dependent crack faces profile, energy release rate are studied in detail, and the results obtained are in good agreement with some known experimental data and other existing nonlinear models. In particular, the predicted crack branching angle is in reasonable agreement with known experimental observation.

Chapter 3 presents a modified speed-dependent cohesive zone model for a steady-state moving crack of constant length. Strain hardening is studied by considering a non-uniform traction given by an arbitrary polynomial. Compared with classical cohesive zone model (Dugdale model), the present modified cohesive zone model predicts a more reasonable fracture energy especially at high crack speed.

Chapter 4 extends the modified cohesive zone model proposed in chapter 3 to a self-similar expanding crack. Speed-dependences of traction force, cohesive zone length, CTOD and fracture energy are discussed in detail. In particular, results show that the dependence of traction on crack speed near a self-similar expanding crack tip is similar to the one near the tip of a Yoffe-type steady-state moving crack of constant length.

Chapter 5 presents a new cohesive zone model to investigate the inertia effect of cohesive zone on a high-speed moving crack. The inertia effect of cohesive zone on traction distribution and fracture energy is studied numerically. Results show that the inertia effect of cohesive zone leads to a practically infinite fracture energy as a finite limiting speed is approached, which could define a limiting terminal crack speed for a ductile material.

Chapter 6 summarizes the major conclusions of this research and suggests a few research topics for future studies.

Chapter 2: Speed-dependent tip fields of a moving crack in a hyperelastic material

2.1 Introduction

Crack growth is a common cause of material failure. LEFM predicts an inverse square root singularity near a static or moving crack tip (Williams, 1957; Yoffe, 1951). At the actual crack tip, however, large deformation is involved and finite elasticity theory is more relevant. Recently, some research results (Bouchbinder et al., 2008; Livne et al., 2010) addressed that finite strain analysis near a moving crack tip is essential for a physically realistic description of the crack-tip stress and deformation fields.

Finite strain analysis of static cracks in hyperelastic materials has attracted considerable attention in the past decades. For example, Knowles and Sternberg (Knowles and Sternberg, 1983) studied crack tip fields near an interface crack tip in a Neo-Hookean material. Ru (Ru, 2002) derived a complete solution for an interface crack in a harmonic elastic material. For dynamic crack in hyperelastic materials, more recently, Bouchbinder et al. (Bouchbinder et al., 2010) showed that some predictions given by linear elasticity are in direct contradiction with experiment observation of the moving crack's tip fields. These authors stressed the importance of finite strain analysis for physical phenomena of moving cracks in hyperelastic materials.

This chapter aims to study finite strain tip fields near a steadily propagating crack in a compressible hyperelastic material of harmonic-type. The harmonic material model was first presented by John (John, 1960), and studied by a number of authors (Knowles and Sternberg, 1975; Li and Steigmann, 1993; Ru, 1997; Varley and Cumberbatch, 1980). The model of harmonic materials and the formulation of a moving crack are described in sections 2.2.1 and 2.2.2. Detailed analysis of the tip asymptotic fields up to the third order is given in sections 2.2.3-2.2.5. In section 2.3, the tip stress and deformation fields are analyzed based on the

asymptotic solutions obtained in sections 2.2.3-2.2.5. The results obtained are applied to a specific hyperelastic material in section 2.4 for which some recent experimental data are available. Implications of the present solutions are further discussed in section 2.5. Finally, the main conclusions are summarized in section 2.6.

2.2 Asymptotic solution near a moving crack tip in a harmonic material

2.2.1 Harmonic materials

Let (X_1,X_2) be the initial coordinate of a material point in undeformed configuration, and (y_1,y_2) be the coordinate of the point after deformation at time t under condition of plane strain, defined by the fixed coordinate system (X_1,X_2) (see Fig. 2.1)

$$\begin{cases} y_1 = y_1(X_1, X_2, t) = X_1 + u_1(X_1, X_2, t) \\ y_2 = y_2(X_1, X_2, t) = X_2 + u_2(X_1, X_2, t) \end{cases} \tag{2.1}$$

where, u_1, u_2 are the displacements of material point (X_1,X_2) at time t. Then, the deformation gradient is given by

$$[\mathbf{F}] = [F_{ij}] = \begin{bmatrix} \dfrac{\partial y_1}{\partial X_1} & \dfrac{\partial y_1}{\partial X_2} \\ \dfrac{\partial y_2}{\partial X_1} & \dfrac{\partial y_2}{\partial X_2} \end{bmatrix} \tag{2.2}$$

Here, we employ the model of harmonic hyperelastic materials, which is introduced by John (John, 1960), and is shown to be relevant for some nonlinear elastic materials, such as rubber (Varley and Cumberbatch, 1980). The strain energy density function of harmonic hyperelastic materials in plane-strain has the following form:

$$W(I,J) = 2\mu_h[F(I) - J] \tag{2.3}$$

in which μ_h is a positive material constant of harmonic material, I and J are two scalar invariants

$$I = \lambda_1 + \lambda_2 = \sqrt{F_{ij}F_{ij} + 2J}, \quad J = \lambda_1\lambda_2 = F_{11}F_{22} - F_{12}F_{21} \tag{2.4}$$

where λ_1 and λ_2 are the two principal stretches, and $F(I)$ is a real material response function of I. In addition, J measures the volume change after deformation so we require $J > 0$. Equation of motion can be expressed as (John, 1960)

$$\begin{cases} \rho u_{1,tt} = \dfrac{\partial P_{11}}{\partial X_1} + \dfrac{\partial P_{12}}{\partial X_2} = P_{11,1} + P_{12,2} \\ \rho u_{2,tt} = \dfrac{\partial P_{21}}{\partial X_1} + \dfrac{\partial P_{22}}{\partial X_2} = P_{21,1} + P_{22,2} \end{cases} \tag{2.5}$$

where P_{ij} are Piola stress components, ρ is the mass density, and a comma stands for partial derivative with respect to t, X_1 or X_2. Introducing a complex variable

$$w = y_1 + iy_2 \tag{2.6}$$

the Piola stresses of a harmonic material are given by (John, 1960)

$$\begin{aligned} P_{12} + iP_{22} &= 2\mu_h \left[\frac{F'(I)}{I}(w_{,2} + iw_{,1}) - iw_{,1} \right] \\ P_{11} + iP_{21} &= 2\mu_h i \left[w_{,2} - \frac{F'(I)}{I}(w_{,2} + iw_{,1}) \right] \end{aligned} \tag{2.7}$$

Combining Eq. (2.5) and (2.6), we get the complex form of the equation of motion as

$$\left[2\mu_h \frac{F'(I)}{I}(w_{,1} - iw_{,2}) \right]_{,1} + i \left[2\mu_h \frac{F'(I)}{I}(w_{,1} - iw_{,2}) \right]_{,2} = \rho u_{1,tt} + i\rho u_{2,tt} \tag{2.8}$$

which is equivalent to Eq. (2.18) in (John, 1960).

2.2.2 A steadily moving crack

In this chapter, we consider a moving crack, steadily propagating at a constant velocity V in an infinite plane of a homogeneous harmonic material under a constant remote mode-I loading (see Fig. 2.1). This type of steady-state crack propagation is convenient to be analyzed in a moving coordinate system (x_1, x_2) defined by

$$x_1 = X_1 - Vt, \quad x_2 = X_2 \tag{2.9}$$

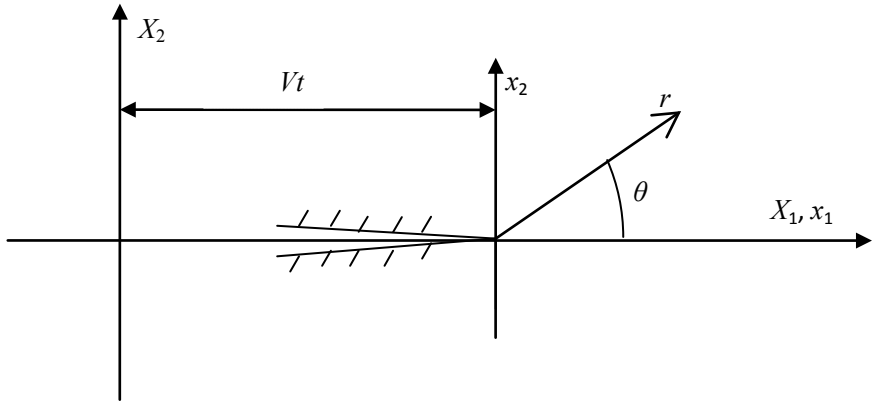

Fig. 2.1 A moving crack of speed V in a plane of harmonic material under steady propagation condition.

As in Fig. 2.1, we introduce polar coordinate system (r, θ), defined by $r = (x_1^2+x_2^2)^{1/2}$ and $\theta = \arctan(x_2/x_1)$. Under steady-state propagation condition, $w(X_1,X_2,t)$ will not explicitly depend on time t in the moving frame (x_1, x_2), and then $w(X_1,X_2,t) = w(x_1, x_2)$. Putting $w(x_1, x_2)$ into Eq. (2.8) and noticing

$$u_{1,tt} = V^2 y_{1,11}, \quad u_{2,tt} = V^2 y_{2,11} \tag{2.10}$$

the equation of motion (2.8) is expressed as

$$[2\mu_h \frac{F'(I)}{I}(w_{,1} - iw_{,2})]_{,1} + i[2\mu_h \frac{F'(I)}{I}(w_{,1} - iw_{,2})]_{,2} = V^2 \rho w_{,11} \tag{2.11}$$

Here, without any confusion, a comma stands for partial derivative with respect to x_1 or x_2. In the present problem, traction-free boundary condition on the crack faces and the remote loading condition are given by

$$\begin{cases} P_{12}(x_1, 0) = 0, & \theta = \pm\pi \\ P_{22}(x_1, 0) = 0, & \theta = \pm\pi \\ \mathbf{P}^{\infty} = \mathbf{P_0}^{\infty}, & |\mathbf{x}| \to \infty \end{cases} \tag{2.12}$$

in which $\mathbf{P_0}^{\infty}$ is a given constant mode-I remote stress at infinity.

2.2.3 First order solution

It is expected that singularity exists near the crack tip. Thus, the first-order asymptotic form of w is given by

$$w = r^m G_1(\theta) + o(r^m), \quad 0 < m < 1 \quad \text{as} \quad r \to 0, \quad \theta \in [-\pi, \pi] \tag{2.13}$$

where $G_1(\theta)$ is an undetermined complex-valued function of θ. In addition, we assume that $F(I)$, as well as its asymptotic behaviour for large values of I is described by (Ru, 2002)

$$F'(I) = \frac{1}{4\alpha}\left[I + \sqrt{I^2 - 16\alpha\beta} \right] \quad \text{and} \quad \frac{F'(I)}{I} \approx \frac{1}{2\alpha} - \frac{2\beta}{I^2}, \ \text{as} \ I \to \infty \tag{2.14}$$

where α and β are two material constants. Knowles and Sternberg (Knowles and Sternberg, 1983) showed that $F'(I)/I$ should approach unity when I tends to infinity, which implies $\alpha = 1/2$. In addition, to get a negative Piola stress at large compression, $\beta > 0$ is required. Therefore, from Eq. (2.14), one gets the first order expansion of response function $F(I)$

$$\frac{F'(I)}{I} = 1, \ \text{as} \quad I \to \infty \tag{2.15}$$

In view of Eq. (2.13) and (2.15), the lowest-order form of Eq. (2.11) is

$$\left(\frac{\partial^2}{\partial {x_1}^2} + \frac{\partial^2}{s^2 \partial {x_2}^2} \right) w = 0 \tag{2.16}$$

where s is defined in terms of crack speed V, the density ρ and the material constant μ_h as

$$s = \sqrt{\frac{2\mu_h - \rho V^2}{2\mu_h}} > 0 \tag{2.17}$$

If we use new variables

$$\xi' = x_1, \ \ \eta' = s x_2 \tag{2.18}$$

Eq. (2.16) becomes

$$\frac{\partial^2 w}{\partial \xi'^2} + \frac{\partial^2 w}{\partial \eta'^2} = 0 \tag{2.19}$$

In the polar coordinates of (ξ', η'), Eq. (2.19) has the following form:

$$\left(\frac{\partial^2}{\partial R^2} + \frac{\partial}{R \partial R} + \frac{\partial^2}{R^2 \partial \varphi^2}\right) w = 0 \tag{2.20}$$

where

$$R = \sqrt{\xi'^2 + \eta'^2}, \quad \varphi = \arctan(\eta'/\xi') \tag{2.21}$$

On the other hand, it follows from Eq. (2.7) and (2.12) that the traction-free boundary condition on the crack faces are given by

$$\frac{F'(I)}{I}(w_{,2} + iw_{,1}) - iw_{,1} = 0, \quad \varphi = \pm\pi \tag{2.22}$$

Solving Eq. (2.20) with the boundary condition (2.22), we find

$$\sin(2m\pi) = 0 \tag{2.23}$$

From Eq. (2.13), one gets $m = 1/2$ and

$$w = R^{1/2} C_1 \sin(\varphi/2) \tag{2.24}$$

where $C_1 = a_1 + \mathrm{i}a_2$ is an arbitrary complex constant. In view of the symmetric condition of the mode-I crack: $y_2(R, \varphi) = -y_2(R,-\varphi)$, $y_1(R, \varphi) = y_1(R,-\varphi)$, one gets

$$w = iR^{1/2} a_2 \sin(\varphi/2) \tag{2.25}$$

where a_2 is an arbitrary positive constant defining the intensity of the lowest-order tip field, and the restriction $a_2 > 0$ reflects the fact that the remote mode-I stress is tensile.

Unfortunately, it can be verified that this lowest order approximation of w leads an identically vanishing Jacobian determinant J. Therefore, we have to seek second order solution of w, in order to ensure the kinematic condition $J > 0$.

2.2.4 Second order solution

To get the second-order tip field, we now seek the solution of the form

$$w = w^{(1)} + w^{(2)} \quad \text{and} \quad w^{(1)} = ia_2 R^{\frac{1}{2}} \sin(\frac{1}{2}\varphi), \; w^{(2)} = R^n G_2(\varphi) \tag{2.26}$$

with $n > 1/2$. The second order expansion of $F(I)$ is

$$\frac{F'(I)}{I} = 1 - \frac{2\beta}{I^2}, \quad \beta > 0 \tag{2.27}$$

Equation of motion (2.11) up to the second-order is given by

$$2\mu_h w^{(2)}{}_{11} + 2\mu_h w^{(2)}{}_{,22} - V^2 \rho w^{(2)}{}_{,11} = 4\mu_h \beta \left[\frac{(w^{(1)}{}_{,1} - i w^{(1)}{}_{,2})}{I^2} \right]_{,1} + 4\mu_h \beta i \left[\frac{(w^{(1)}{}_{,1} - i w^{(1)}{}_{,2})}{I^2} \right]_{,2} \quad (2.28)$$

First, the RHS of Eq. (2.28) can be expressed as a product of $R^{-1/2}$ and a function of φ. So, if $n < 3/2$, the RHS of (2.28) are higher-order small quantities and then should be neglected within the second-order solution. Therefore Eq. (2.28) becomes a homogeneous equation

$$\frac{\partial^2 w^{(2)}}{\partial \xi'^2} + \frac{\partial^2 w^{(2)}}{\partial \eta'^2} = 0 \quad (2.29)$$

And from Eq. (2.22), the boundary condition for the second-order solution is

$$\frac{\partial w^{(2)}}{\partial \eta'} = 0, \qquad \varphi = \pm\pi \quad (2.30)$$

Therefore, the second order solution is obtained with $n = 1$ as $w^{(2)} = C_2 R\cos(\varphi)$, where $C_2 = b_1 + ib_2$ is an arbitrary complex constant. In view of the symmetric condition, one gets $b_2 = 0$ and

$$w^{(2)} = b_1 R\cos(\varphi) \quad (2.31)$$

where b_1 is an arbitrary real constant which determines the second-order tip field. For the mode-I loading, the symmetry implies that $b_1 > 0$.

Up to the second-order solution, taking Eq. (2.25) and (2.31) into (2.4), in view of (2.9) and (2.18), one gets

$$J = \frac{1}{2} a_2 b_1 s R^{-1/2} \cos\left(\frac{\varphi}{2}\right) \quad (2.32)$$

Therefore, $J > 0$ can be met everywhere except on the two crack surfaces $\varphi = \pm\pi$, which leaves us have to pursue the third order solution.

2.2.5 Third order solution

To get the third-order tip solution, we now seek the solution of the form

$$w = w^{(1)} + w^{(2)} + w^{(3)} \quad \text{and} \quad w^{(3)} = R^p T_1(\varphi) + i(R^p T_3(\varphi) \ln R + R^p T_2(\varphi)) \quad (2.33)$$

Here, similar to (Knowles and Sternberg, 1975), we introduce ln$R$ term in imaginary part because only $R^p T_2(\varphi)$ term cannot satisfy the boundary condition. In Eq. (2.33), $T_1(\varphi)$, $T_2(\varphi)$ and $T_3(\varphi)$ are real functions and $p > 1$. Thus, omitting all higher order terms, Eq. (2.11) becomes

$$2\mu_h w^{(3)}{}_{11} + 2\mu_h w^{(3)}{}_{,22} - V^2 \rho w^{(3)}{}_{,11} = 4\mu_h \beta \left[\frac{(w^{(1)}{}_{,1} - i w^{(1)}{}_{,2})}{I^2} \right]_{,1} + 4\mu_h \beta i \left[\frac{(w^{(1)}{}_{,1} - i w^{(1)}{}_{,2})}{I^2} \right]_{,2} \quad (2.34)$$

Noticing that the first order approximation of I is

$$I = \frac{1}{2} a_2 R^{-\frac{1}{2}} \sqrt{\sin^2(\frac{\varphi}{2}) + s^2 \cos^2(\frac{\varphi}{2})} \quad (2.35)$$

putting Eq. (2.35) into (2.34), one gets equation for the third-order solution

$$\frac{\partial^2 w^{(3)}}{\partial \xi'^2} + \frac{\partial^2 w^{(3)}}{\partial \eta'^2} = R^{-1/2} \left[f_1(\varphi) + i f_2(\varphi) \right] \quad (2.36)$$

where, $f_1(\varphi)$ is a real symmetric function and $f_2(\varphi)$ is a real anti-symmetric function, given by

$$\begin{aligned} f_1(\varphi) = {} & \frac{2\beta}{a_2} \frac{\left[2\cos(\varphi)(\sin^2(\frac{\varphi}{2}) + s^2 \cos^2(\frac{\varphi}{2})) + (1 - s^2)\sin^2(\varphi) \right] s \cos(\frac{\varphi}{2})}{\left[\sin^2(\frac{\varphi}{2}) + s^2 \cos^2(\frac{\varphi}{2}) \right]^2} \\ & + \frac{2\beta s}{a_2} \frac{\left[2\sin(\varphi)(\sin^2(\frac{\varphi}{2}) + s^2 \cos^2(\frac{\varphi}{2})) - (1 - s^2)\sin(\varphi)\cos(\varphi) \right] \sin(\frac{\varphi}{2})}{\left[\sin^2(\frac{\varphi}{2}) + s^2 \cos^2(\frac{\varphi}{2}) \right]^2}, \\ f_2(\varphi) = {} & \frac{\beta \rho V^2}{\mu_h a_2} \frac{3\cos^2(\frac{\varphi}{2})\sin(\frac{\varphi}{2}) - \sin^3(\frac{\varphi}{2})}{\sin^2(\frac{\varphi}{2}) + s^2 \cos^2(\frac{\varphi}{2})} \\ & - \frac{2\beta}{a_2} \frac{\left[2\cos(\varphi)(\sin^2(\frac{\varphi}{2}) + s^2 \cos^2(\frac{\varphi}{2})) + (1 - s^2)\sin^2(\varphi) \right] \sin(\frac{\varphi}{2})}{\left[\sin^2(\frac{\varphi}{2}) + s^2 \cos^2(\frac{\varphi}{2}) \right]^2} \\ & + \frac{2\beta}{a_2} s \frac{\left[2\sin(\varphi)(\sin^2(\frac{\varphi}{2}) + s^2 \cos^2(\frac{\varphi}{2})) - (1 - s^2)\sin(\varphi)\cos(\varphi) \right] s \cos(\frac{\varphi}{2})}{\left[\sin^2(\frac{\varphi}{2}) + s^2 \cos^2(\frac{\varphi}{2}) \right]^2} \end{aligned} \quad (2.37)$$

From Eq. (2.36) and Eq. (2.37), it is seen that $p = 3/2$. It follows from Eq. (2.22) that the third

order boundary condition is

$$s\frac{\partial w^{(3)}}{\partial \eta'} = 4\frac{\beta}{a_2}R^{\frac{1}{2}}\frac{is\cos(\frac{\varphi}{2})+\sin(\frac{\varphi}{2})}{\sin^2(\frac{\varphi}{2})+s^2\cos^2(\frac{\varphi}{2})}, \quad \varphi=\pm\pi \tag{2.38}$$

Substituting Eq. (2.33) into (2.36), and (2.38), one gets equations and boundary conditions for the three unknown functions $T_1(\varphi)$, $T_2(\varphi)$ and $T_3(\varphi)$. In particular, for $T_1(\varphi)$, we have

$$\frac{9}{4}T_1(\varphi)+T_1''(\varphi)=f_1(\varphi) \tag{2.39}$$

and boundary conditions

$$\begin{aligned} T_1'(\varphi) &= \frac{4\beta}{sa_2} && \varphi=-\pi \\ T_1'(\varphi) &= -\frac{4\beta}{sa_2} && \varphi=\pi \end{aligned} \tag{2.40}$$

In addition, for $T_2(\varphi)$ and $T_3(\varphi)$, we have two coupled equations

$$\begin{aligned} &\frac{9}{4}T_3(\varphi)+T_3''(\varphi)=0 \\ &\frac{9}{4}T_2(\varphi)+T_2''(\varphi)=f_2(\varphi)-3T_3(\varphi) \end{aligned} \tag{2.41}$$

with boundary conditions

$$\begin{aligned} &T_3'(\varphi)=0, \quad \varphi=\pm\pi \\ &T_2'(\varphi)=0, \quad \varphi=\pm\pi \end{aligned} \tag{2.42}$$

First, for $T_1(\varphi)$, we change the boundary value problem (2.39), (2.40) into an initial value problem. Based on the shooting method (Hildebrand, 1987), let us rewrite Eq. (2.39) and (2.40) as

$$\begin{aligned} &T_1(\varphi)=U_1(\varphi)+c_1V_1(\varphi) \\ &\frac{9}{4}U_1(\varphi)+U_1''(\varphi)=f_1(\varphi) \\ &\frac{9}{4}V_1(\varphi)+V_1''(\varphi)=0 \end{aligned}$$

$$U_1(\varphi)=0, U_1'(\varphi)=\frac{4\beta}{sa_2} \qquad \varphi=-\pi$$
$$V_1(\varphi)=1, V_1'(\varphi)=0 \qquad \varphi=-\pi \tag{2.43}$$

Clearly, Eq. (2.43) is equivalent to (2.39) and (2.40) provided the real constant c_1 meets $c_1 V_1'(\pi) = [-4\beta/sa_2 - U_1'(\pi)]$. From (2.43) we have $V_1(\varphi) = \sin(3\varphi/2)$ and $V_1'(\pi) = 0$. Therefore, to satisfy the above condition (2.43), we have $U_1'(\pi) = -4\beta/sa_2$. Since $f_1(\varphi)$ is a symmetric function, $T_1'(\pi) = -T_1'(-\pi)$ and $V_1'(\pi) = 0$, $U_1'(\pi) = -4\beta/sa_2$ is consistent with its boundary condition at $\varphi=-\pi$. Therefore, one gets

$$T_1(\varphi)=U_1(\varphi)+c_1\sin(\frac{3}{2}\varphi) \tag{2.44}$$

where, c_1 is an arbitrary real constant and $U_1(\varphi)$ can be solved numerically based on the initial value problem Eq. (2.43), as shown in Fig. 2.2.

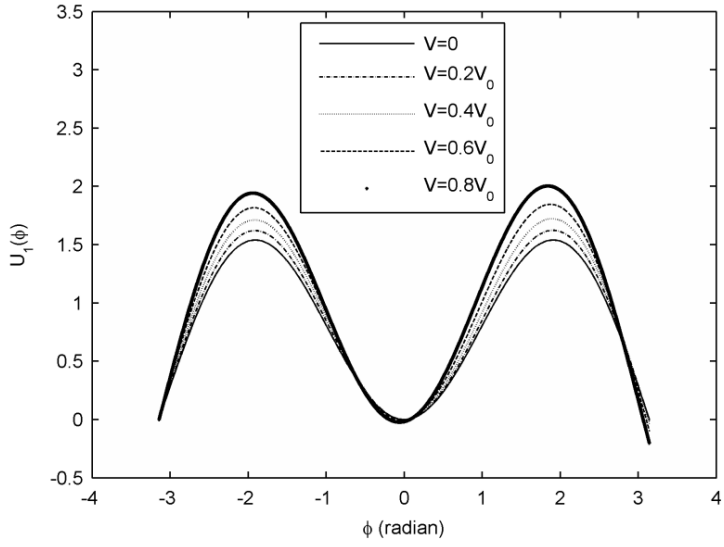

Fig. 2.2 Numerical results for $U_1(\varphi)$ (unit:$2\beta/a_2$). Where V_0 is normalized speed and $V_0 = (\mu_h/\rho)^{1/2}$.

For mode-I crack $T_1(\varphi)$ should be symmetric while $U_1(\varphi)$ is not a symmetric function. Therefore, c_1 must be determined to cancel the anti-symmetric part of $U_1(\varphi)$ so that $T_1(\varphi)$ remains a symmetric function. For example, $c_1 = 0$ when $s = 1$. With such chosen c_1, $T_1(\varphi)$ is a symmetric function without any arbitrary constant, as shown in Fig. 2.3. It is noted that when $s = 1$, $V = 0$ (static case), $T_1(\varphi)$ has a simple form

$$T_1(\varphi)=\frac{2\beta}{a_2}\left[\cos(\frac{1}{2}\varphi)-\cos(\frac{3}{2}\varphi)\right] \tag{2.45}$$

For this static case, the differences between the analytical solution and our numerical solution are shown in table 2.1. This validates accuracy of the present numerical method.

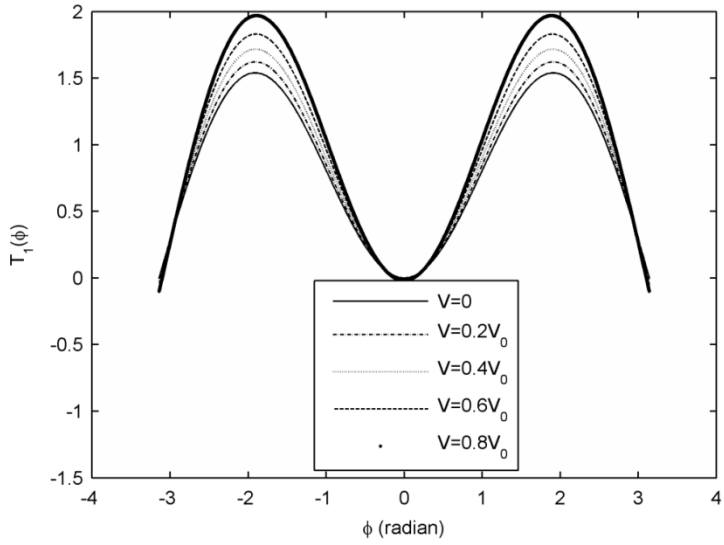

Fig. 2.3 Numerical results for $T_1(\varphi)$ (unit: $2\beta/a_2$).

Table 2.1 Error analysis (when $s = 1$, unit: $2\beta/a_2$)

$T_1(\varphi)$	$\varphi = 0$	$\varphi = \pi/6$	$\varphi = \pi/3$	$\varphi = \pi/2$	$\varphi = 2\pi/3$	$\varphi = \pi$
analytical	0	0.2588	0.8660	1.4142	-0.8660	0
Present numerical	0	0.2592	0.8652	1.4147	-0.8652	0
error	0	-0.0004	0.0008	-0.0005	-0.0008	0

To solve $T_3(\varphi)$ and $T_2(\varphi)$, let us first get $T_3(\varphi)$ from the first equation in (2.41) and the first set of boundary condition in (2.42), as follows

$$T_3(\varphi) = d\sin(\frac{3}{2}\varphi) \tag{2.46}$$

in which d is a real constant dependent of s. Taking Eq. (2.46) into the second equation of (2.41), multiplying $\sin(3\varphi/2)$ on both sides and integrating from $-\pi$ to π, in view of the boundary conditions for $T_2(\varphi)$, one gets

$$d = \frac{\int_{-\pi}^{\pi} \sin(\frac{3}{2}\varphi) f_2(\varphi) d\varphi}{3\pi} \tag{2.47}$$

From (2.47) and (2.37), we know d varies with s, and $d(s) = 0$ when $s = 1$.

Next, we can adopt the same numerical method to find $T_2(\varphi)$ as

$$T_2(\varphi) = U_2(\varphi) + c_2 \sin(\frac{3}{2}\varphi) \tag{2.48}$$

where $U_2(\varphi)$ is a particular solution of the second equation of (2.41) with the boundary conditions (2.42) whose existence is ensured under condition (2.47), while the second term on RHS of (2.48) is a homogeneous solution with an arbitrary constant c_2. Numerical results for the particular solution $U_2(\varphi)$ are shown in Fig. 2.4.

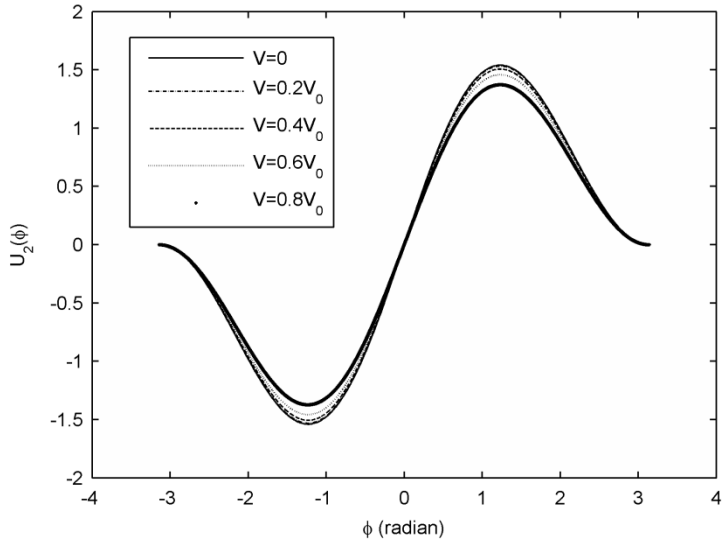

Fig. 2.4 Numerical results for $U_2(\varphi)$ (unit:$2\beta/a_2$).

Clearly, $T_3(\varphi)$ and $T_2(\varphi)$ are both odd functions. Therefore, the third order solution is

$$w^{(3)} = R^{\frac{3}{2}} T_1(\varphi) + iR^{\frac{3}{2}} \left[d(s) \sin(\frac{3}{2}\varphi) \right] \ln R + iR^{\frac{3}{2}} \left[U_2(\varphi) + c_2 \sin(\frac{3}{2}\varphi) \right] \tag{2.49}$$

where c_2 is an arbitrary constant associated with the third-order tip field.

In summary, we derived the crack-tip fields up to the third-order. The obtained tip fields are controlled by two controlling parameters b_1 and a_2 related to the constant mode-I remote loading, while another arbitrary parameter, c_2, appears in the third-order field. Furthermore

$$\begin{aligned} y_{1,1} &= b_1 + R^{1/2} P_1(\varphi) \qquad y_{1,2} = R^{1/2} s P_2(\varphi) \\ y_{2,1} &= -\frac{1}{2} a_2 R^{-1/2} \sin(\frac{\varphi}{2}) + R^{1/2} P_3(\varphi) + R^{1/2} Q_1(\varphi) \ln R \\ y_{2,2} &= \frac{1}{2} a_2 R^{-1/2} s \cos(\frac{\varphi}{2}) + R^{1/2} s P_4(\varphi) + R^{1/2} s Q_2(\varphi) \ln R \end{aligned} \tag{2.50}$$

where

$$
\begin{aligned}
P_1(\varphi) &= \frac{3}{2}\cos(\varphi)T_1(\varphi) - \sin(\varphi)T_1'(\varphi) \\
P_2(\varphi) &= \frac{3}{2}\sin(\varphi)T_1(\varphi) + \cos(\varphi)T_1'(\varphi) \\
P_3(\varphi) &= d\cos(\varphi)\sin(\frac{3}{2}\varphi) + \frac{3}{2}\cos(\varphi)\left[U_2(\varphi) + c_2\sin(\frac{3}{2}\varphi)\right] \\
&\quad - \sin(\varphi)\left[U_2'(\varphi) + \frac{3}{2}c_2\cos(\frac{3}{2}\varphi)\right] \\
P_4(\varphi) &= d\sin(\varphi)\sin(\frac{3}{2}\varphi) + \frac{3}{2}\sin(\varphi)\left[U_2(\varphi) + c_2\sin(\frac{3}{2}\varphi)\right] \\
&\quad + \cos(\varphi)\left[U_2'(\varphi) + \frac{3}{2}c_2\cos(\frac{3}{2}\varphi)\right] \\
Q_1(\varphi) &= \frac{3}{2}\left[d\cos(\varphi)\sin(\frac{3}{2}\varphi) - d\sin(\varphi)\cos(\frac{3}{2}\varphi)\right] \\
Q_2(\varphi) &= \frac{3}{2}\left[d\sin(\varphi)\sin(\frac{3}{2}\varphi) + d\cos(\varphi)\cos(\frac{3}{2}\varphi)\right]
\end{aligned}
\tag{2.51}
$$

To justify the condition $J > 0$, it follows from Eq. (2.4) that

$$
\begin{aligned}
J &= \frac{1}{2}a_2 b_1 R^{-\frac{1}{2}} s\cos(\frac{\varphi}{2}) + \frac{1}{2}a_2 s\cos(\frac{\varphi}{2})\left[\frac{3}{2}\cos(\varphi)T_1(\varphi) - \sin(\varphi)T_1'(\varphi)\right] \\
&\quad + \frac{1}{2}a_2\sin(\frac{\varphi}{2})\left[\frac{3}{2}s\sin(\varphi)T_1(\varphi) + s\cos(\varphi)T_1'(\varphi)\right] + O(r^{\frac{1}{2}})
\end{aligned}
\tag{2.52}
$$

From Eq. (2.41), one gets

$$
J = 2\beta + O(r^{1/2}), \quad \varphi = \pm\pi \tag{2.53}
$$

Clearly, the third order solution ensures $J > 0$ everywhere including the two crack faces. From Eq. (2.50), we can see that different from static case (when $s = 1$, $V = 0$), the present third order solution of moving crack possesses an additional term $O(R^{3/2}\ln R)$.

2.3 Stress field near the moving crack tip

Based on the asymptotic solution obtained in previous sections, the Piola stress can be obtained from Eq. (2.7) as

$$\begin{aligned}
P_{11} &= 2\mu_h b_1 + 2\mu_h R^{\frac{1}{2}}\left[P_1(\varphi) - P_5(\varphi)\right] \\
P_{12} &= 2\mu_h R^{\frac{1}{2}}\left[P_2(\varphi) - P_6(\varphi)\right] \\
P_{21} &= -\mu_h a_2 R^{-\frac{1}{2}}\sin(\frac{\varphi}{2}) + 2\mu_h R^{\frac{1}{2}}\left[P_3(\varphi) + P_6(\varphi)\right] + 2\mu_h R^{\frac{1}{2}} Q_1(\varphi)\ln R \\
P_{22} &= \mu_h s a_2 R^{-\frac{1}{2}}\cos(\frac{\varphi}{2}) + 2\mu_h R^{\frac{1}{2}}\left[P_4(\varphi) - P_5(\varphi)\right] + 2\mu_h R^{\frac{1}{2}} Q_2(\varphi)\ln R
\end{aligned} \tag{2.54}$$

where

$$\begin{aligned}
P_5(\varphi) &= \frac{4\beta s\cos(\frac{\varphi}{2})}{a_2\left[\sin^2(\frac{\varphi}{2}) + s^2\cos(\frac{\varphi}{2})\right]} \\
P_6(\varphi) &= \frac{4\beta\sin(\frac{\varphi}{2})}{a_2\left[\sin^2(\frac{\varphi}{2}) + s^2\cos(\frac{\varphi}{2})\right]}
\end{aligned} \tag{2.55}$$

Noticing the relation (Knowles and Sternberg, 1983)

$$\sigma_{\alpha\beta} = 2\mu_h\left\{\frac{F'(I)}{IJ}F_{\alpha\rho}F_{\beta\rho} + \left[\frac{F'(I)}{I} - 1\right]\delta_{\alpha\beta}\right\} \tag{2.56}$$

the symmetric Cauchy stress components are given as

$$\begin{aligned}
\sigma_{11} = {} & \frac{2\mu_h}{J}b_1^{\,2} + \frac{4\mu_h}{J}R^{\frac{1}{2}}b_1 P_1(\varphi) - R\frac{16\beta\mu_h}{a_2^{\,2}\left[\sin^2(\frac{\varphi}{2}) + s^2\cos(\frac{\varphi}{2})\right]} \\
& + \frac{2\mu_h}{J}R\left\{P_1^2(\varphi) + s^2 P_2^2(\varphi) - \frac{8\beta b_1^{\,2}}{a_2^{\,2}\left[\sin^2(\frac{\varphi}{2}) + s^2\cos(\frac{\varphi}{2})\right]}\right\}
\end{aligned}$$

$$\sigma_{12} = -\frac{\mu_h}{J} R^{-\frac{1}{2}} a_2 b_1 \sin(\frac{\varphi}{2}) + \frac{\mu_h}{J}\left[a_2 s^2 P_2(\varphi)\cos(\frac{\varphi}{2}) - a_2 P_1(\varphi)\sin(\frac{\varphi}{2}) \right]$$

$$+\frac{2\mu_h}{J} R^{\frac{1}{2}} \left\{ b_1 P_3(\varphi) + \frac{4\beta a_2 b_1 \sin(\frac{\varphi}{2})}{a_2{}^2\left[\sin^2(\frac{\varphi}{2}) + s^2\cos(\frac{\varphi}{2}) \right]} \right\}$$

$$+\frac{2\mu_h}{J} R^{\frac{1}{2}} \ln R b_1 Q_1(\varphi) + \frac{2\mu_h}{J} R\left[P_1(\varphi)Q_1(\varphi) + s^2 P_2(\varphi)Q_2(\varphi) \right]\ln R$$

$$+\frac{2\mu_h}{J} R\left\{ P_1(\varphi)P_3(\varphi) + s^2 P_2(\varphi)P_4(\varphi) - \frac{4\beta a_2\left[s^2 P_2(\varphi)\cos(\frac{\varphi}{2}) - P_1(\varphi)\sin(\frac{\varphi}{2}) \right]}{a_2{}^2\left[\sin^2(\frac{\varphi}{2}) + s^2\cos(\frac{\varphi}{2}) \right]} \right\}$$

$$\sigma_{22} = \frac{\mu_h a_2{}^2}{2J} R^{-1}\left[\sin^2(\frac{\varphi}{2}) + s^2\cos^2(\frac{\varphi}{2}) \right]$$

$$+\frac{2\mu_h}{J}\left[s^2 a_2 P_4(\varphi)\cos(\frac{\varphi}{2}) - a_2 P_3(\varphi)\sin(\frac{\varphi}{2}) - \frac{2\beta s^2\cos(\frac{\varphi}{2}) + 2\beta\sin^2(\frac{\varphi}{2})}{\sin^2(\frac{\varphi}{2}) + s^2\cos(\frac{\varphi}{2})} \right]$$

$$+\frac{2\mu_h a_2}{J}\left[s^2 Q_2(\varphi)\cos(\frac{\varphi}{2}) - Q_1(\varphi)\sin(\frac{\varphi}{2}) \right]\ln R - R\frac{16\beta\mu_h}{a_2{}^2\left[\sin^2(\frac{\varphi}{2}) + s^2\cos(\frac{\varphi}{2}) \right]}$$

$$+\frac{2\mu_h}{J} R\left\{ s^2 P_4{}^2(\varphi) + P_3{}^2(\varphi) - \frac{2\beta\left[s^2 P_4(\varphi)\cos(\frac{\varphi}{2}) - P_3(\varphi)\sin(\frac{\varphi}{2}) \right]}{a_2\left[\sin^2(\frac{\varphi}{2}) + s^2\cos(\frac{\varphi}{2}) \right]} \right\}$$

$$+\frac{4\mu_h}{J} R\left\{ s^2 P_4(\varphi)Q_2(\varphi) + P_3(\varphi)Q_1(\varphi) - \frac{4\beta\left[s^2 Q_2(\varphi)\cos(\frac{\varphi}{2}) - Q_1(\varphi)\sin(\frac{\varphi}{2}) \right]}{a_2\left[\sin^2(\frac{\varphi}{2}) + s^2\cos(\frac{\varphi}{2}) \right]} \right\}\ln R \qquad (2.57)$$

$$+\frac{2\mu_h}{J} R\left[s^2 Q_2{}^2(\varphi) + Q_1{}^2(\varphi) \right]\ln^2 R$$

For convenience, stress field can also be written in the (x_1,x_2) plane. Using the polar coordinates (r, θ) in the (x_1, x_2) plane, we have

$$R = r\sqrt{s^2\sin^2(\theta) + \cos^2(\theta)}, \quad \varphi = \arctan[s\tan(\theta)] \qquad (2.58)$$

Substituting r, θ into Eq. (2.55) and (2.57), one gets Piola stress in the (x_1, x_2) plane (up to the most singular terms)

$$
\begin{aligned}
P_{11} &= 2\mu_h b_1 \\
P_{12} &= 2\mu_h r^{\frac{1}{2}}(s^2\sin^2\theta+\cos^2\theta)^{\frac{1}{4}}\left[P_2(\theta)-P_6(\theta)\right] \\
P_{21} &= \begin{cases} -\dfrac{\sqrt{2}}{2}\mu_h a_2 r^{-\frac{1}{2}}(s^2\sin^2\theta+\cos^2\theta)^{-\frac{1}{2}}(\sqrt{s^2\sin^2\theta+\cos^2\theta}-\cos\theta)^{\frac{1}{2}} & (0<\theta\le\pi) \\ \dfrac{\sqrt{2}}{2}\mu_h a_2 r^{-\frac{1}{2}}(s^2\sin^2\theta+\cos^2\theta)^{-\frac{1}{2}}(\sqrt{s^2\sin^2\theta+\cos^2\theta}-\cos\theta)^{\frac{1}{2}} & (-\pi\le\theta\le 0) \end{cases} \\
P_{22} &= \frac{\sqrt{2}}{2}\mu_h s a_2 r^{-\frac{1}{2}}(s^2\sin^2\theta+\cos^2\theta)^{-\frac{1}{2}}(\sqrt{s^2\sin^2\theta+\cos^2\theta}+\cos\theta)^{\frac{1}{2}}
\end{aligned}
\tag{2.59}
$$

And the Cauchy stress (up to the most singular terms) are given by

$$
\begin{aligned}
\sigma_{11} &= \frac{4\sqrt{2}\mu_h b_1}{a_2} r^{\frac{1}{2}} s^{-1}(s^2\sin^2\theta+\cos^2\theta)^{\frac{1}{2}}(\sqrt{s^2\sin^2\theta+\cos^2\theta}+\cos\theta)^{-\frac{1}{2}} \\
\sigma_{12} &= \sigma_{21} = \begin{cases} -2\mu_h s^{-2}\sin^{-1}(\theta)(\sqrt{s^2\sin^2\theta+\cos^2\theta}-\cos\theta) & \theta\neq 0 \\ 0 & \theta = 0 \end{cases} \\
\sigma_{22} &= \frac{\sqrt{2}\mu_h a_2}{2b_1} r^{-\frac{1}{2}} s^{-1}\left\{[1-\cos\theta(s^2\sin^2\theta+\cos^2\theta)^{-\frac{1}{2}}]+s^2[1+\cos\theta(s^2\sin^2\theta+\cos^2\theta)^{-\frac{1}{2}}]\right\} \\
&\quad\times(\sqrt{s^2\sin^2\theta+\cos^2\theta}+\cos\theta)^{-\frac{1}{2}}
\end{aligned}
\tag{2.60}
$$

It is seen that the leading-order singular stress field is controlled by the two parameters b_1 and a_2, which are determined by the constant mode-I remove loading and the crack speed, and the other parameter, c_2, does not appear in the above leading-order stress field.

In addition, for a steadily propagating crack in a nonlinear hyperelastic material, the dynamic energy release rate is given by (Freund, 1990)

$$
G = \lim_{\Gamma\to 0}\int_{\Gamma}\left[(W+\frac{1}{2}\rho V^2\frac{\partial y_i}{\partial x_1}\frac{\partial y_i}{\partial x_1})n_1 - P_{ij}n_j\frac{\partial y_i}{\partial x_1}\right]d\Gamma \tag{2.61}
$$

where the contour Γ is around the moving crack tip. Here, the value of G is calculated by choosing a rectangular contour Γ around the moving crack tip (Freund, 1990). After substituting Eq. (2.59) into (2.61), one gets

$$
G = \frac{\pi}{2}\mu_h {a_2}^2 s \tag{2.62}
$$

2.4 Comparison to experimental data

Experiments on crack tip fields in hyperelastic materials have been rarely reported in the literature. Recently, Bouchbinder et al. (Bouchbinder et al., 2008, 2010) conducted a series of experiments to study the tip deformation fields of a moving crack using polyacrylamide gels. Here, we apply our crack tip solution obtained in previous sections to their experiments, by determining the two controlling parameters b_1 and a_2 of our solutions to fit their measured data. In doing so, we are able to examine the implications of the present solution to propagating cracks in hyperelastic materials, with a particular interest in speed-dependent nonlinear phenomena near a moving crack tip in a hyperelastic material.

i) Determination of b_1

In reference (Livne et al., 2010), the normal strain along the crack propagation direction $u_{1,1}$ at $\theta = 0$ was measured. From their measured data, $u_{1,1}$ is found to approach a finite constant when the crack tip is approached along $\theta = 0$, which is consistent with the present solution from (31): $b_1 - 1 = u_{1,1}$ when $\theta = 0$. From experiment (Livne et al., 2010), we find that the estimated b_1 (from the measured strain at r = 0.2mm, see Fig.3.b in (Livne et al., 2010)) nearly linearly increases with the crack speed, for example, b_1 increases from 1.6 at $V = 0.3C_s$ to 2.9 at $V = 0.8C_s$ (where, C_s is the transverse elastic wave speed). In particular, in agreement with (Livne et al., 2010), $u_{1,1}$ at $\varphi = 0$ near crack tip is a positive constant, in contradiction with linear fracture mechanics that predicts $u_{1,1} \sim r^{-1/2}$ near the crack tip. This indicates that nonlinear large deformation is indeed essential for a realistic description of crack tip deformation field in a hyperelastic material.

ii) Determination of a_2

The crack tip surfaces predicted by the present model, obtained from Eq. (2.25) and (2.31), is given by

$$y_1 = b_1 y_2^{\,2} / a_2^{\,2} \tag{2.63}$$

In order to compare the above prediction with the measured crack profile, we first obtain the value of $b_1/a_2^{\,2}$ from experimental data (Bouchbinder et al., 2008) over the range r = 0.03mm to r = 0.2mm, and thus determine the value of a_2 based on the determined value of b_1. We found that the crack profile given by Eq. (2.63) with $a_2 = 0.021\text{m}^{1/2}$ when $V = 0.2C_s$ and $a_2 = 0.030\text{m}^{1/2}$ when $V = 0.53C_s$ best fits the experiment data (Fig. 2 in (Bouchbinder et al., 2008)). After determining the value of a_2, the theoretical prediction of (2.63) is compared with experimental measurements given in Fig. 2 in (Bouchbinder et al., 2008) at a larger region (from r =0.2mm to r = 0.42mm). From Fig. 2.5 in this chapter, it is seen that the theoretical perdition of the present harmonic material model is well consistent with experiment data of polyacrylamide gels (Fig. 2 in (Bouchbinder et al., 2008)) over a quite larger range, indicating the robustness of the present model.

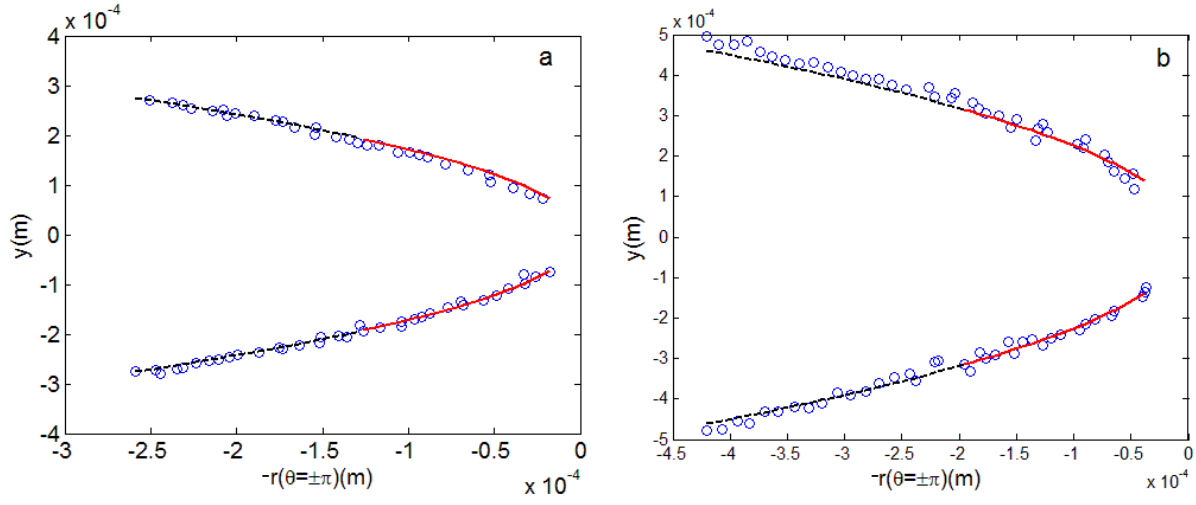

Fig. 2.5 Crack tip profiles at $V = 0.2C_s$ (Fig. a) and $V = 0.53C_s$ (Fig. b). Blue circles stand for the measured crack tip profile. Red solid lines are the parabolic fitted crack tip profile ($b_1/a_2^{\,2}$ =3398m^{-1} when $V = 0.2C_s$ and $b_1/a_2^{\,2}$ =2066m^{-1} when $V = 0.53C_s$) and black dash lines are the predicted crack surfaces by Eq. (2.63).

iii) Energy release rate G

Once a_2, as well as its dependence on crack speed V, is determined, the energy release rate G can be calculated from Eq. (2.62) as a function of crack speed V. We first investigate the

energy release rate based on the present harmonic material model (G_h) in static case. From Eq. (2.62), we get $G_h = \pi\mu_h a_2^2/2$, when $V = 0$. While Neo-Hookean theory predicts $G_n = \pi\mu a_2^2/4$ (Livne et al., 2010), where μ is the elastic shear modulus in linear elastic theory. To study the speed effect on energy release rate, we assume that these two models are coincident in static case, therefore $\mu_h = \mu/2$. Together with the estimated values of b_1 and b_1/a_2^2 based on experimental data of reference (Livne et al., 2010), we calculated the energy release rate based on the present harmonic material model (G_h), as shown in Fig. 2.6. The energy release rate given by a weakly nonlinear theory (Bouchbinder et al., 2008) (G_w) or by a neo-Hookean material model (Livne et al., 2010) (G_n) were also presented in Fig. 2.6 for a comparison. It is seen from Fig. 2.6 that harmonic model is in reasonable agreement with other two models. Moreover, all the three nonlinear models predict an nearly linear increased energy release rate with the crack speed, in good agreement with experimental data given for other gels in references (Baumberger et al., 2006; Tanaka et al., 2000).

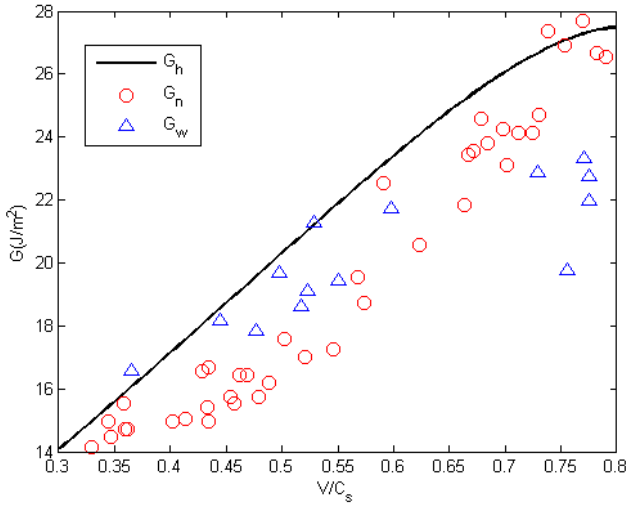

Fig. 2.6 Energy release rate from different theories at different crack speed V.

2.5 Further discussions

In what follows, we further examine the implications of the present solutions to tip nonlinear phenomena of a moving crack in a hyperelastic material.

i) The dominate stress component in front of crack tip

First, linear elastic dynamic fracture mechanics for mode-I crack predicts $\sigma_{22} \leq \sigma_{11}$ (Freund, 1990) in front of the crack tip ($\theta = 0$). On the other hand, the present harmonic material model Eq. (2.60) predicts that σ_{22} is more singular than all other stress components, which implies that $\sigma_{22}(r, 0) > \sigma_{11}(r, 0)$ at the crack tip.

ii) Crack branching at high crack speed

Yoffe (Yoffe, 1951) has explained crack-path branching with linear dynamic fracture mechanics based on the maximum hoop stress criterion. Her analysis showed that when crack speed reaches a critical value, the singular hoop stress at the moving crack tip is no longer maximized at the crack propagation direction $\theta = 0$, which implies crack branching. In the present harmonic material model, the Cauchy hoop stress can be obtained from Eq. (2.60) as

$$\sigma_{\theta\theta} = \sigma_{11} \sin^2 \theta + \sigma_{22} \cos^2 \theta - 2\sigma_{12} \sin\theta \cos\theta \tag{2.64}$$

It is seen that the leading-order singular hoop stress always attains its maximum at $\theta = 0$ for all crack speed. However, many previous works, see e.g. Cotterell (Cotterell, 1965), Ramulu et al. (Ramulu et al., 1982) have suggested that crack-path branching depends on non-singular stresses. Instead of considering the most singular hoop stress immediately in the front of the crack tip, it is suggested that one should consider the hoop stress at a small but finite distance (r_c) away from the crack tip. Based on this idea, for example, if we expect that crack branching happens at $V_c = 0.8C_s$, which is the critical velocity for oscillatory instability in polyacrylamide gels (Bouchbinder et al., 2008, 2010), based on the parameters we got from last section, we obtain the critical distance $r_c = 0.01$mm, which is on the same order of critical value 0.05mm suggested for PMMA (Williams and Ewing, 1972). The hoop stresses at $r_c = 0.01$mm for several crack

speed are shown in Fig. 2.7. From Fig. 2.7 we can see, at crack speed $V = 0.8C_s$, the hoop stress is maximized at $\theta = 30^o$. Therefore, the moving crack is expected to be deflected and propagate along at an angle 30^o to the original direction of crack propagation. This predicted angle is close to the experimentally observed 25^o for PMMA (Murphy et al., 2006) which has been shown to have similar dynamic crack oscillation behavior as polyacrylamide gels (Bouchbinder et al., 2010).

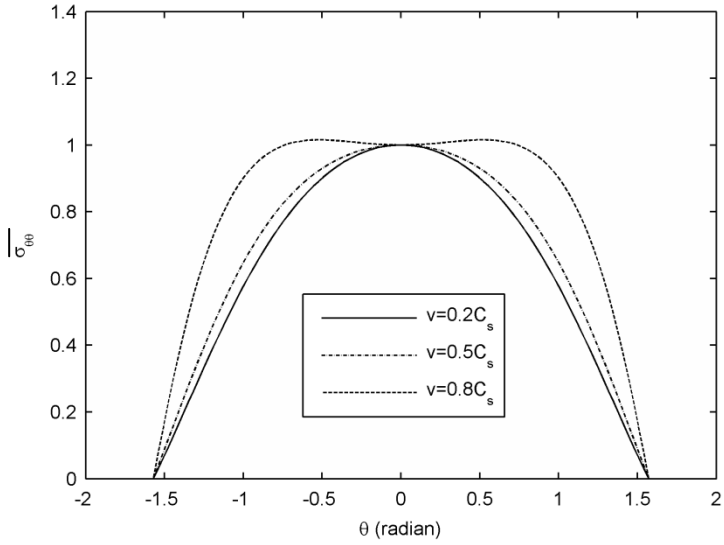

Fig. 2.7 Variation of the normalized hoop stress with angle θ at r_c = 0.01mm for several values of crack speed, where, $\overline{\sigma_{\theta\theta}} = \sigma_{\theta\theta} / \sigma_{\theta\theta}(\theta = 0)$, is normalized hoop stress. When $V = 0.8C_s$, hoop stress is maximized at $\theta = 30^o$, which indicates that crack more likely propagates along a direction inclined at about 30^o to the crack surfaces.

iii) Interface crack in harmonic bi-materials

A well-known problem with linear elastic fracture mechanics is the oscillatory singularity and associated interpenetration of bi-materials near an interface crack tip. Knowles and Sternberg (Knowles and Sternberg, 1975), Ru (Ru, 1997) have shown that finite deformation models can eliminate oscillations near a static interface crack tip. Here, we will prove that oscillatory tip field does not occur near a moving interface crack tip in harmonic bi-materials. Let us consider an interface crack lying between two different harmonic materials, the upper is material 1, and lower is material 2. Therefore, the lowest-order solution must satisfy the

equation of motion, traction-free crack-face and continuous interface conditions as follows

$$
\begin{aligned}
&(\frac{\partial^2}{\partial R_1^{\,2}}+\frac{\partial}{R_1\partial R_1}+\frac{\partial^2}{R_1^{\,2}\partial \varphi_1^{\,2}})\left[w\right]_1=0\\
&(\frac{\partial^2}{\partial R_2^{\,2}}+\frac{\partial}{R_2\partial R_2}+\frac{\partial^2}{R_2^{\,2}\partial \varphi_2^{\,2}})\left[w\right]_2=0\\
&\left[\sigma_{12}+i\sigma_{22}\right]_1=0,\quad \varphi_1=\pi\\
&\left[\sigma_{12}+i\sigma_{22}\right]_2=0,\quad \varphi_2=-\pi\\
&\left[w\right]_1=\left[w\right]_2,\qquad\qquad\qquad \varphi_1=0\\
&\left[\sigma_{12}+i\sigma_{22}\right]_1=\left[\sigma_{12}+i\sigma_{22}\right]_2\qquad \varphi_2=0
\end{aligned}
\tag{2.65}
$$

where, $[w]_i$ and $[\sigma_{12}+i\sigma_{22}]_i$ stands for the deformation and stress field for each material, and

$$
\begin{aligned}
&R_1=\sqrt{x_1^{\,2}+s_1^{\,2}x_2^{\,2}},\ R_2=\sqrt{x_1^{\,2}+s_2^{\,2}x_2^{\,2}},\ \varphi_1=\arctan(\frac{s_1x_2}{x_1}),\ \varphi_2=\arctan(\frac{s_2x_2}{x_1})\\
&s_1=\sqrt{\frac{2\mu_1-\rho_1V^2}{2\mu_1}},s_2=\sqrt{\frac{2\mu_2-\rho_2V^2}{2\mu_2}}
\end{aligned}
\tag{2.66}
$$

The only first order asymptotic solution which satisfies Eq. (2.65) is given by

$$
\begin{aligned}
&\left[w\right]_1=R_1^{\frac{1}{2}}C\sin(\frac{1}{2}\varphi_1)\\
&\left[w\right]_2=R_2^{\frac{1}{2}}\frac{\mu_1}{\mu_2}C\sin(\frac{1}{2}\varphi_2)
\end{aligned}
\tag{2.67}
$$

where, C is an arbitrary complex constant. Thus, oscillation does not occur and interpenetration can be prevented as long as $\mathrm{Re}(C) > 0$, $\mathrm{Im}(C) > 0$, which is ensured by the condition that the remote mode-I stress is tensile.

2.6 Conclusions

A finite strain harmonic material model is employed to study mode-I steadily moving crack in hyperelastic materials. The asymptotic crack tip fields are derived up to the third order, which depend on two controlling parameters to be determined by the constant remote loading and the crack speed. The solution is applied to a specific hyperelastic material for which some recent

experiment data are available in the literature. It is found that the present harmonic material model can well describe the observed crack-face profile near a moving crack tip, and the energy release rate and its dependence on the crack speed predicted by the present model are in reasonable agreement with those given by several existing nonlinear elastic models. In particular, crack branching angle predicted by the present model is also in reasonable agreement with some known experimental data. These results suggest that, instead of its mathematical simplicity, the harmonic material model has the potential to catch the main nonlinear phenomena near a moving crack tip in a nonlinear hyperelastic material.

Chapter 3: A modified speed-dependent cohesive zone model for a steady-state moving crack of constant length

3.1 Introduction

The cohesive zone models, first proposed by Barenblatt (Barenblatt, 1959) and Dugdale (Dugdale, 1960) for a static crack, have been applied to dynamic crack problems of nonlinear or ductile materials, see e.g. (Atkinson, 1968; Goodier and Field, 1963; Kanninen, 1968). In these works, a major assumption is that the normal traction force on the cohesive zone is constant and equal to the yielding stress of the material, and therefore the early models are unable to incorporate strain hardening and the influence of normal stress (σ_{xx}) parallel to the crack axis. Thus, modified cohesive zone models are developed and employed in static crack analytic analysis (Bhargava and Bansal, 2002; Daniewicz, 1994; Harrop, 1978; Isherwood and Williams, 1970; Theocaris and Gdoutos, 1974; Yao and Huang, 2011), in which the effect of normal stress σ_{xx} is showed to be of secondary importance for static cracks. Furthermore, non-uniform traction distribution is widely employed in numerical simulation of crack propagation (Scheider, 2009; Tvergaard and Hutchinson, 1994; Xu and Needleman, 1994; Zhou et al., 2005). At high crack speed, however, inertia effect significantly influences crack tip stress state (Freund, 1990). As a result, other stress components, especially the normal stress σ_{xx} along the crack axis, could play an important role in the cohesive zone. Actually, some experiments (Alpa et al., 1979; Lu and Chow, 1990) have shown that the stress component σ_{xx} significantly influences fracture process, a phenomenon which has not been well studied by the existing cohesive zone models (such as (Atkinson, 1968; Bhargava and Bansal, 2002; Daniewicz, 1994; Goodier and Field, 1963; Harrop, 1978; Isherwood and Williams, 1970; Kanninen, 1968; Theocaris and Gdoutos, 1974; Yao and Huang, 2011) for ductile materials. For example, the effect of σ_{xx} on the yielding criterion imposed on the cohesive zone has recently drawn considerable attentions (Lu and

Chow, 1990; Neimitz, 2004; Scheider, 2009; Siegmund and Brocks, 2000; Tvergaard and Hutchinson, 1994; Wnuk and Legat, 2002) for static cracks. However, to the best of my knowledge, little attention has been paid to dynamic cracks. In particular, analytic solution for a moving crack with variable cohesive zone traction is not available in literature, and the crack speed effects on yielding criterion, cohesive zone length and fracture energy for mode-I moving cracks remains unclear.

In this chapter, the problem of a steady-state moving crack under mode-I remote loading is studied with a modified cohesive zone model described in section 3.2. In this modified model, normal traction force on the cohesive zone is assumed as an arbitrary symmetric polynomial of the coordinate x along the crack axis, which is to be determined as a part of the solution by satisfying specific stress-based criterion on the cohesive zone (e.g. von Mises yielding criterion with or without hardening). In section 3.3, with the von Mises criterion without hardening defined by a constant yielding stress Y, unlike the classical Dugdale model of moving cracks (Goodier and Field, 1963; Kanninen, 1968) which predicts that the cohesive zone length is independent of crack speed, the present model predicts that the cohesive zone length increases monotonically with crack speed under moderate remote mode-I loading T ($T \leq 0.5Y$). A more general non-uniform traction distribution defined by a sixth-order symmetric polynomial is studied in section 3.3.2, where the non-uniform traction is determined by the material ductility property (Siegmund and Brocks, 2000; Wnuk and Mura, 1983), initial yielding stress, hardening, crack speed and remote loading. Numerical results show that the cohesive zone length and displacements of the zone face depend on the form of traction distribution, and the polynomial traction model predicts a better crack profiles than the uniform traction model as compared to experimental data. Reasonable agreement between the present results and some known experimental data, demonstrated in section 3.4, suggests that the speed dependent cohesive zone traction force (as described by the present model) is essential to capture the speed effect on dynamic fracture. Finally, main conclusions are summarised in section 3.5.

3.2 A modified cohesive zone model for a steady-state moving crack

In this section, a modified cohesive zone model is proposed for a Yoffe-type steady-state moving crack of constant length $2c$ in an infinite elastic plane, subjected to the mode-I remote tensile loading T. It is assumed that the cohesive zone have a length c' at each of two crack tips (see Fig. 3.1). In a fixed coordinate system (x', y'), the crack is moving along the x' axis at a constant speed V. Under the steady-state conditions, stress and displacement fields will not explicitly depend on time t in the moving frame (x, y) defined by $x = x' - Vt, y = y'$ (see Fig. 3.1). Thus the two displacement components (u_x, u_y) in the moving frame (x, y) can be given in terms of two wave functions $\varsigma(x, y)$ and $\psi(x, y)$ (Craggs, 1960)

$$u_x = \frac{\partial \varsigma}{\partial x} + \frac{\partial \psi}{\partial y}, \qquad u_y = \frac{\partial \varsigma}{\partial y} - \frac{\partial \psi}{\partial x} \tag{3.1}$$

The two wave functions $\varsigma(x, y)$ and $\psi(x, y)$ meet harmonic equations

$$\left(\frac{\partial^2}{\partial x^2} + \frac{\partial^2}{\partial y_d^{\,2}} \right) \varsigma = 0, \qquad \left(\frac{\partial^2}{\partial x^2} + \frac{\partial^2}{\partial y_s^{\,2}} \right) \psi = 0 \tag{3.2}$$

where

$$y_d = \beta_1 y, \;\; y_s = \beta_2 y, \;\; \beta_1 = \sqrt{1 - V^2 / C_d^{\,2}}, \;\; \beta_2 = \sqrt{1 - V^2 / C_s^{\,2}} \tag{3.3}$$

with $C_d > C_s > V$ (the crack speed is slower than the transverse elastic wave speed), and C_d and C_s are longitudinal and transverse elastic wave speeds defined by

$$C_d^{\,2} = \frac{\kappa + 1}{\kappa - 1} \frac{\mu}{\rho}, \;\; C_s^{\,2} = \frac{\mu}{\rho} \tag{3.4}$$

in which ρ is the mass density, μ is the elastic shear modulus, and κ is defined by Poisson's ratio ν as

$$\kappa = \begin{cases} 3 - 4\nu & \text{plane strain} \\ \dfrac{3 - \nu}{1 + \nu} & \text{plane stress} \end{cases} \tag{3.5}$$

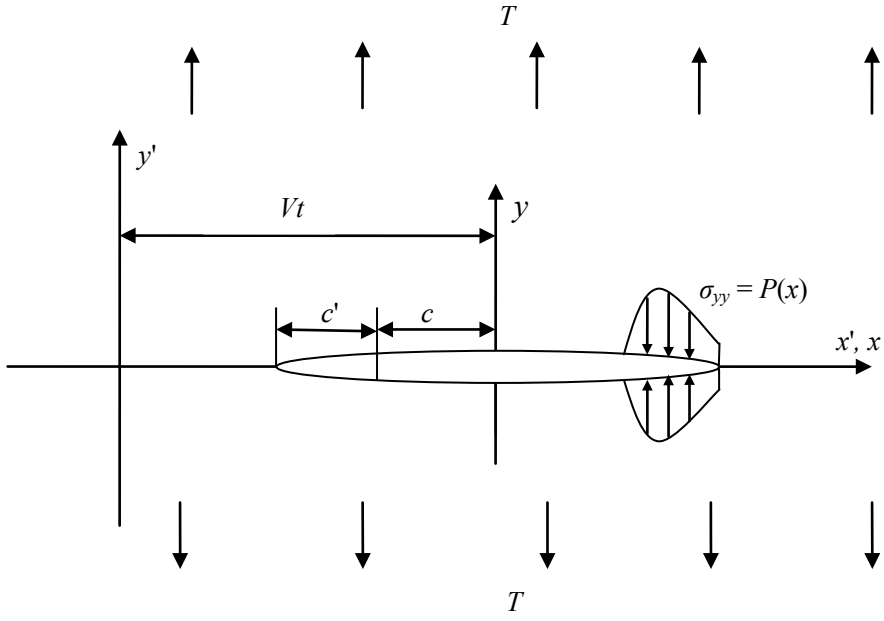

Fig. 3.1 A crack of constant length 2*c* in the moving coordinate system (*x*, *y*) with remote loading *T* and traction force *P*(*x*) on the cohesive zone.

In the present mode-I crack problem, the stress field is symmetrical about the real axis and the shear stress σ_{xy} vanishes on crack faces and the cohesive zone. Therefore, the boundary conditions for the present problem are

$$\left.\begin{array}{ll} \sigma_{yy} = 0 & |x| < c \\ \sigma_{yy} = P(x) & c \le |x| \le c + c' \\ \sigma_{xy} = 0 & |x| \le c + c' \end{array}\right\} \quad \text{at } y = 0$$
$$\sigma_{xx} = 0,\ \sigma_{xy} = 0,\ \sigma_{yy} = T \quad \text{at infinity} \tag{3.6}$$

where the undetermined normal traction force *P*(*x*) on the cohesive zone can be an arbitrary symmetric function of *x* and will be determined as part of the solution so that specific stress-based yielding criterion is met along the cohesive zone. As mentioned before, in the classical Dugdale model (Atkinson, 1968; Dugdale, 1960; Goodier and Field, 1963; Kanninen, 1968), the normal traction force *P*(*x*) on the cohesive zone is constant and equal to the yielding stress *Y*. To the best of our knowledge, except few works which studied simpler linear (Bhargava and Bansal, 2002), or parabolic (Harrop, 1978), or exponential cohesive force (Daniewicz, 1994; Wnuk and Legat, 2002) under small scale yielding condition for static cracks, no attempt has

been made to study more general non-uniform cohesive force $P(x)$ especially for moving cracks. Therefore, in what follows, an analytic solution will be derived for a moving crack with a non-uniform cohesive force $P(x)$ defined by an arbitrary polynomial of the coordinate x.

For this purpose, first, let us introduce complex variables (Craggs, 1960)

$$z_1 = x + iy_d\,, \qquad z_2 = x + iy_s \tag{3.7}$$

Thus the two wave functions can be given as

$$\varsigma(z_1) = \frac{1}{2\mu}\left[F_1(z_1) + \overline{F_1(z_1)}\right], \quad \psi(z_2) = \frac{1}{2\mu} i\left[F_2(z_2) - \overline{F_2(z_2)}\right] \tag{3.8}$$

where $F_1(z_1)$ is an analytical function of the complex variable z_1, and $F_2(z_2)$ is an analytic function of the complex variable z_2, respectively, in the entire complex plane except the crack faces and the cohesive zone, and $\overline{F_1(z_1)}$ and $\overline{F_2(z_2)}$ are their conjugates. Denoting

$$\Phi(z_1) = \frac{\mathrm{d}F_1(z_1)}{\mathrm{d}z_1}, \quad \Psi(z_2) = \frac{\mathrm{d}F_2(z_2)}{\mathrm{d}z_2} \tag{3.9}$$

it can be verified (Rice, 1968) that stresses in the entire plane can be given by

$$\begin{aligned}
\sigma_{xx} &= \mathrm{Re}\left\{(2\beta_1^2 - \beta_2^2 + 1)\Phi'(z_1) - 2\beta_2\Psi'(z_2)\right\} \\
\sigma_{yy} &= \mathrm{Re}\left\{-(\beta_2^2 + 1)\Phi'(z_1) + 2\beta_2\Psi'(z_2)\right\} \\
\sigma_{xy} &= \mathrm{Im}\left\{-2\beta_1\Phi'(z_1) + (\beta_2^2 + 1)\Psi'(z_2)\right\}
\end{aligned} \tag{3.10}$$

where, prime stands for derivate. From the third equation in (3.10) and the condition (3.6) that the shear stress vanishes along both crack and cohesive zone (where $z_1 = z_2 = z$), one gets on the crack and cohesive zone faces

$$\begin{aligned}
\left[-2\beta_1\Phi'(z) + \left(1 + \beta_2^2\right)\Psi'(z)\right]^+ &= \left[-2\beta_1\overline{\Phi'}(z) + \left(1 + \beta_2^2\right)\overline{\Psi'}(z)\right]^- \\
\left[-2\beta_1\Phi'(z) + \left(1 + \beta_2^2\right)\Psi'(z)\right]^- &= \left[-2\beta_1\overline{\Phi'}(z) + \left(1 + \beta_2^2\right)\overline{\Psi'}(z)\right]^+
\end{aligned} \tag{3.11}$$

where the superscripts '+' and '−' denote the limit values from the upper and lower half -planes, respectively. Thus, it follows from Eq. (3.11) that the expression inside the brackets on the left-hand side of the following equation is continuous across the crack and the cohesive zone, namely

$$\left[-2\beta_1\Phi'(z)-2\beta_1\overline{\Phi'}(z)+(1+\beta_2{}^2)\Psi'(z)+(1+\beta_2{}^2)\overline{\Psi'}(z)\right]_-^+=0 \tag{3.12}$$

Therefore, it follows from the principle of analytic continuation that the expression is analytical on the entire complex plane and thus must be a constant (Lang, 1999)

$$-2\beta_1\Phi'(z)-2\beta_1\overline{\Phi'}(z)+(1+\beta_2{}^2)\Psi'(z)+(1+\beta_2{}^2)\overline{\Psi'}(z)=-4\beta_1\Phi'(\infty)+2(1+\beta_2{}^2)\Psi'(\infty) \tag{3.13}$$

in the entire complex plane. Here, the asymptotic stress conditions at infinity indicate that the limits of the two functions Φ' and Ψ' at infinity are bounded and real, and furthermore

$$\Phi'(\infty)=\frac{T}{2(\beta_1{}^2-\beta_2{}^2)},\ \Psi'(\infty)=\frac{2\beta_1{}^2-\beta_2{}^2+1}{4\beta_2(\beta_1{}^2-\beta_2{}^2)}T \tag{3.14}$$

Substituting Eq. (3.13) into (3.11), one gets

$$\left[-2\beta_1\Phi'(z)+\left(1+\beta_2^2\right)\Psi'(z)\right]^+ +\left[-2\beta_1\Phi'(z)+\left(1+\beta_2^2\right)\Psi'(z)\right]^- =-4\beta_1\Phi'(\infty)+2(1+\beta_2{}^2)\Psi'(\infty) \tag{3.15}$$

Combined with Eq. (3.14) and the third equation in (3.10), the bounded solution of the above inhomogeneous equation (which is bounded at the tips of crack and cohesive zone) is given by

$$-2\beta_1\Phi'(z)+\left(1+\beta_2^2\right)\Psi'(z)=\frac{-4\beta_1\beta_2+\left(1+\beta_2^2\right)\left(2\beta_1{}^2-\beta_2^2+1\right)}{4\beta_2\left(\beta_1{}^2-\beta_2^2\right)}T \tag{3.16}$$

In particular, substituting Eq. (3.16) into (3.10), one gets a general relation between σ_{xx} and σ_{yy} on the entire real axis

$$\sigma_{xx}=R_a(V)\left(\sigma_{yy}-T\right),\quad R_a(V)=\frac{2(\beta_1{}^2-\beta_2{}^2)(1+\beta_2{}^2)}{4\beta_1\beta_2-(1+\beta_2{}^2)^2}-1 \tag{3.17}$$

where $R_a(V)$ is a speed-dependent function, its value increases continuously from unity, at $V=0$, to infinity at the Rayleigh wave speed C_R, similar to dynamic elastic models (Freund, 1990). It is seen from (3.17) that, at high crack speed for which $R_a(V)$ is much larger than unity, the normal stress σ_{xx} could be much larger than σ_{yy} and thus play an important role in the cohesive zone. It is stressed that Eq. (3.17) holds for arbitrary traction force $P(x)$. In classical Dugdale model, $P(x)$ is taken as a constant equal to the yielding stress Y. Here, we consider the general case when $P(x)$ is defined by an arbitrary polynomial with real coefficients,

$$P(x) = A_n x^n + A_{n-1} x^{n-1} + \cdots + A_1 x + A_0 \tag{3.18}$$

where n is an arbitrary positive integer, the real coefficients A_0, A_1,...A_n are to be determined by satisfying specific stress-based criterion on the cohesive zone (see section 3.3.1 and 3.3.2) and symmetric conditions of a mode-I crack.

Now, from the second equation in Eq. (3.10) and the normal stress condition on the upper and lower faces of the crack and the cohesive zone, the limit values of Eq. (3.10-2) on the crack and cohesive zone faces from the upper and lower half planes give

$$\begin{aligned} &-\left(1+\beta_2{}^2\right)\left[\Phi'(z)^+ + \overline{\Phi'}(z)^-\right] + 2\beta_2\left[\Psi'(z)^+ + \overline{\Psi'}(z)^-\right] = 2P(x)H(|x|-c) \\ &-\left(1+\beta_2{}^2\right)\left[\Phi'(z)^- + \overline{\Phi'}(z)^+\right] + 2\beta_2\left[\Psi'(z)^- + \overline{\Psi'}(z)^+\right] = 2P(x)H(|x|-c) \end{aligned} \tag{3.19}$$

where $H(|x|-c)$ is Heaviside step function. Thus, the subtraction of the two equations in Eq. (3.19) gives

$$\left[-(1+\beta_2{}^2)\Phi'(z) + (1+\beta_2{}^2)\overline{\Phi'}(z) + 2\beta_2\Psi'(z) - 2\beta_2\overline{\Psi'}(z)\right]_-^+ = 0 \tag{3.20}$$

Therefore, it follows from principle of analytical continuation and conditions (3.14) at infinity that

$$-(1+\beta_2{}^2)\Phi'(z) + (1+\beta_2{}^2)\overline{\Phi'}(z) + 2\beta_2\Psi'(z) - 2\beta_2\overline{\Psi'}(z) = 0 \tag{3.21}$$

in the entire complex plane. Taking Eq. (3.21) into Eq. (3.19), one shows that along crack faces and cohesive zone

$$\left[-\left(1+\beta_2^2\right)\Phi'(z) + 2\beta_2\Psi'(z)\right]^+ + \left[-\left(1+\beta_2^2\right)\Phi'(z) + 2\beta_2\Psi'(z)\right]^- = 2P(x)H(|x|-c) \tag{3.22}$$

Condition (3.22) is a non-homogeneous Riemann-Hilbert problem (Rice, 1968), and its general solution (which has the inverse square-root singularity at the tips of cohesive zone) is given by (see appendix A for details)

$$-\left(1+\beta_2^2\right)\Phi'(z) + 2\beta_2\Psi'(z) = \frac{1}{i\pi}\left[P(z)\left(i\pi + \ln\frac{z\sqrt{\left(c+c'\right)^2 - c^2} - ic\sqrt{z^2-\left(c+c'\right)^2}}{z\sqrt{\left(c+c'\right)^2 - c^2} + ic\sqrt{z^2-\left(c+c'\right)^2}}\right) - \frac{iQ(z)}{\sqrt{z^2-\left(c+c'\right)^2}}\right] + \frac{Tz}{\sqrt{z^2-\left(c+c'\right)^2}}$$

(3.23)

where $Q(z)$ is an arbitrary polynomial of finite degree to be determined by the remote conditions at infinity, and a T-related term has been separated from $Q(z)$ just for convenience. From Eq. (3.14) and (3.23), it is verified that $Q(z)$ must be a polynomial of z with real coefficients. In particular, for the present mode-I crack problem, the traction force $P(x)$ is symmetric about y-axis and thus an even polynomial in x, therefore

$$\begin{aligned} P(z) &= A_n z^n + A_{n-2} z^{n-2} + \cdots + A_2 z^2 + A_0 \\ Q(z) &= B_n z^{n+1} + B_{n-2} z^{n-1} + \cdots + B_2 z^3 + B_0 z \end{aligned} \tag{3.24}$$

where n is an even integer, and B_0, B_2, B_4... B_n are some real constants to be determined by remote loading condition. It is seen from Eq. (3.1), (3.8), (3.9), and (3.23) that single valued displacements (u_x, u_y) are assured by the fact that $Q(z)$ given by (3.24) is an odd function of z and does not contain a non-zero constant term. From Eq. (3.16) and (3.23), one gets

$$\begin{aligned} \Phi'(z) &= \frac{1+\beta_2^{\,2}}{i\pi\left[4\beta_1\beta_2-(1+\beta_2^{\,2})^2\right]}\left[P(z)\left(i\pi+\ln\frac{z\sqrt{(c+c')^2-c^2}-ia\sqrt{z^2-(c+c')^2}}{z\sqrt{(c+c')^2-c^2}+ia\sqrt{z^2-(c+c')^2}}\right)-\frac{iQ(z)}{\sqrt{z^2-(c+c')^2}}\right] \\ &\quad+\frac{1+\beta_2^{\,2}}{4\beta_1\beta_2-(1+\beta_2^{\,2})^2}\frac{Tz}{\sqrt{z^2-(c+c')^2}}+H_1 \\ \Psi'(z) &= \frac{2\beta_1}{i\pi\left[4\beta_1\beta_2-(1+\beta_2^{\,2})^2\right]}\left[P(z)\left(i\pi+\ln\frac{z\sqrt{(c+c')^2-a^2}-ia\sqrt{z^2-(c+c')^2}}{z\sqrt{(c+c')^2-a^2}+ia\sqrt{z^2-(c+c')^2}}\right)-\frac{iQ(z)}{\sqrt{z^2-(c+c')^2}}\right] \\ &\quad+\frac{2\beta_1}{4\beta_1\beta_2-(1+\beta_2^{\,2})^2}\frac{Tz}{\sqrt{z^2-(c+c')^2}}+H_2 \end{aligned} \tag{3.25}$$

where H_1 and H_2 are two real constants related with crack speed V and remote loading T with

$$H_1=-\frac{(1+\beta_2^{\,2})(2\beta_1^{\,2}-\beta_2^{\,2}+1)-4\beta_1\beta_2}{2\left[4\beta_1\beta_2-(1+\beta_2^{\,2})^2\right](\beta_1^{\,2}-\beta_2^{\,2})}T,\ H_2=-\frac{(1+\beta_2^{\,2})\left[(1+\beta_2^{\,2})(2\beta_1^{\,2}-\beta_2^{\,2}+1)-4\beta_1\beta_2\right]}{4\beta_2\left[4\beta_1\beta_2-(1+\beta_2^{\,2})^2\right](\beta_1^{\,2}-\beta_2^{\,2})}T \tag{3.26}$$

For $|z|\to\infty$, Eq. (3.23) has the following asymptotic form

$$-\left(1+\beta_2^2\right)\Phi'(z)+2\beta_2\Psi'(z)=P(z)-\frac{P(z)}{\pi}\left\{2\arctan\frac{c}{\sqrt{(c+c')^2-c^2}}+\sum_{i=1}^{n/2}\frac{g_1^{(i)}(0)}{i!}\left[\frac{(c+c')^2}{z^2}\right]^i\right\}$$
$$-\frac{Q(z)}{\pi z}\left\{1+\sum_{i=1}^{n/2}\frac{g_2^{(i)}(0)}{i!}\left[\frac{(c+c')^2}{z^2}\right]^i\right\}+T \tag{3.27}$$

where, $g_1^{(i)}(0)$ is the value of the ith derivative of $g_1(z)$ at the point 0, $g_2^{(i)}(0)$ is the value of ith derivative of $g_2(z)$ at the point 0, with

$$g_1(z)=2\arctan\frac{c\sqrt{1-z}}{\sqrt{(c+c')^2-c^2}},\quad g_2(z)=\frac{1}{\sqrt{1-z}} \tag{3.28}$$

Thus, the coefficients B_0-B_n can be determined by Eq. (3.27) and the remote loading conditions that $\sigma_{yy} = T$ at infinity. For example, for a sixth order polynomial traction $P(x)$ with $n = 6$ and four real coefficients A_0, A_2, A_4 and A_6, the condition $\sigma_{yy} = T$ at infinity gives

$$2P(z)\left\{\arccos\frac{c}{c+c'}+\frac{c\sqrt{(c+c')^2-c^2}}{(c+c')^2}\left[\frac{(c+c')^2}{z^2}\right]+\left[\frac{c\sqrt{(c+c')^2-c^2}}{4(c+c')^2}+\frac{c^3\sqrt{(c+c')^2-c^2}}{2(c+c')^4}\right]\left[\frac{(c+c')^2}{z^2}\right]^2\right.$$
$$\left.+\left[\frac{c\sqrt{(c+c')^2-c^2}}{8(c+c')^2}+\frac{c^3\sqrt{(c+c')^2-c^2}}{6(c+c')^4}+\frac{c^5\sqrt{(c+c')^2-c^2}}{3(c+c')^6}\right]\left[\frac{(c+c')^2}{z^2}\right]^3\right\}$$
$$-\frac{Q(z)}{z}\left\{1+\frac{1}{2}\left[\frac{(c+c')^2}{z^2}\right]+\frac{3}{8}\left[\frac{(c+c')^2}{z^2}\right]^2+\frac{5}{16}\left[\frac{(c+c')^2}{z^2}\right]^3\right\}=0 \tag{3.29}$$

It follows from Eq. (3.24) and (3.29) that the four coefficients B_0, B_2, B_4, B_6 are given in terms of the coefficients A_0, A_1, A_4 and A_6 which are shown in appendix B. The cohesive zone length can be determined by the condition of cancelling the inverse square root singularity at the two ends of the cohesive zone $|z| = c+c'$ in Eq. (3.23), which gives $Q(c+c') = \pi T(c+c')$. Thus from Eq. (B.1) one gets

$$2\arccos\frac{c}{c+c'}A_0+\left[c\sqrt{(c+c')^2-c^2}+(c+c')^2\arccos\left(\frac{c}{c+c'}\right)\right]A_2+\left[\frac{c^3\sqrt{(c+c')^2-c^2}}{2}\right.$$
$$\left.+\frac{3c(c+c')^2\sqrt{(c+c')^2-c^2}}{4}+\frac{3(c+c')^4}{4}\arccos\left(\frac{c}{c+c'}\right)\right]A_4+\left[\frac{c^5\sqrt{(c+c')^2-c^2}}{3}\right. \tag{3.30}$$
$$\left.+\frac{5c^3(c+c')^2\sqrt{(c+c')^2-c^2}}{12}+\frac{5c(c+c')^4\sqrt{(c+c')^2-c^2}}{8}+\frac{5(c+c')^6}{8}\arccos\left(\frac{c}{c+c'}\right)\right]A_6=T\pi$$

In particular, if $P(x)\equiv A_0$ and A_0 is independent of crack speed, it can be easily verified that Eq. (3.30) reduces to the results of classical Dugdale model

$$\arccos\left(\frac{c}{c+c'}\right)=\frac{\pi T}{2A_0}$$

In addition, if $P(x)=A_0+A_2x^2$, and A_0, A_2 are independent of crack speed, Eq. (3.30) gives

$$2\arccos\frac{c}{c+c'}A_0+\left[c\sqrt{(c+c')^2-c^2}+(c+c')^2\arccos\left(\frac{c}{c+c'}\right)\right]A_2=T\pi$$

which is identical to the result of (Harrop, 1978) (see Eq. (7) in (Harrop, 1978)).

Furthermore, the displacement u_y at $y = 0$ can be determined by (Rice, 1968)

$$u_y=-\mathrm{Im}\left\{\beta_1\int\Phi'(x)\mathrm{d}x-\int\Psi'(x)\mathrm{d}x\right\}/\mu \tag{3.31}$$

Taking Eq. (3.25) into (3.31), one shows that on the cohesive zone,

$$u_y(x)^+=\int\frac{A(V)}{\pi\mu}\left[-P(x)\ln\frac{x\sqrt{(c+c')^2-c^2}+c\sqrt{(c+c')^2-x^2}}{x\sqrt{(c+c')^2-c^2}-c\sqrt{(c+c')^2-x^2}}+\frac{Q(x)}{\sqrt{(c+c')^2-x^2}}\right.$$
$$\left.-\frac{\pi Tx}{\sqrt{(c+c')^2-x^2}}\right]\mathrm{d}x \tag{3.32}$$

where,

$$A(V)=\frac{\beta_1(1-\beta_2{}^2)}{4\beta_1\beta_2-(1+\beta_2{}^2)^2} \tag{3.33}$$

And the fracture energy in the cohesive zone can be determined by

$$
\begin{aligned}
G &= -\int_{c}^{c+c'} 2P(x)\frac{\mathrm{d}u_y(x)}{\mathrm{d}x}\mathrm{d}x \\
&= -2\int_{c}^{c+c'} \frac{A(V)P(x)}{\pi\mu}\left[-P(x)\ln\frac{x\sqrt{(c+c')^2-c^2}+c\sqrt{(c+c')^2-x^2}}{x\sqrt{(c+c')^2-c^2}-c\sqrt{(c+c')^2-x^2}}\right. \\
&\quad \left.+\frac{Q(x)}{\sqrt{(c+c')^2-x^2}}-\frac{\pi Tx}{\sqrt{(c+c')^2-x^2}}\right]\mathrm{d}x
\end{aligned}
\tag{3.34}
$$

Thus the open displacement and fracture energy in the cohesive zone can be obtained by Eq. (3.32) and (3.34) explicitly for a uniform cohesive force $P(x)\equiv A_0$, and numerically for non-uniform polynomial cohesive force $P(x)$ of the form (3.24).

3.3 Results and Discussion

3.3.1 A simple model with von Mises criterion without hardening (plane stress)

First, we consider a simple case that the material is under plane stress and satisfies the von Mises criterion with a constant yielding stress Y (without hardening) in the cohesive zone. Therefore, in view of Eq. (3.17) and the fact that shear stress vanishes on the cohesive zone, the normal traction $P(x)$ must be a constant on the entire cohesive zone, denoted by S, and determined by the von Mises yielding criterion, which gives

$$
S=\frac{2R_a{}^2T-R_aT+\sqrt{(R_aT-2R_a{}^2T)^2-4(R_a{}^2-R_a+1)(R_a{}^2T^2-Y^2)}}{2(R_a{}^2-R_a+1)} \tag{3.35}
$$

Thus, in this simple case, unlike the classical Dugdale model which gives $S = Y$, the constant traction force S given by the present model is a function of crack speed, remote loading and material yielding stress Y (see Fig. 3.2). In this case, $P(x) = A_0 = S$. The cohesive zone length c' can be obtained from Eq. (3.30)

$$c' = c\left[\sec(\frac{\pi T}{2S}) - 1\right] \tag{3.36}$$

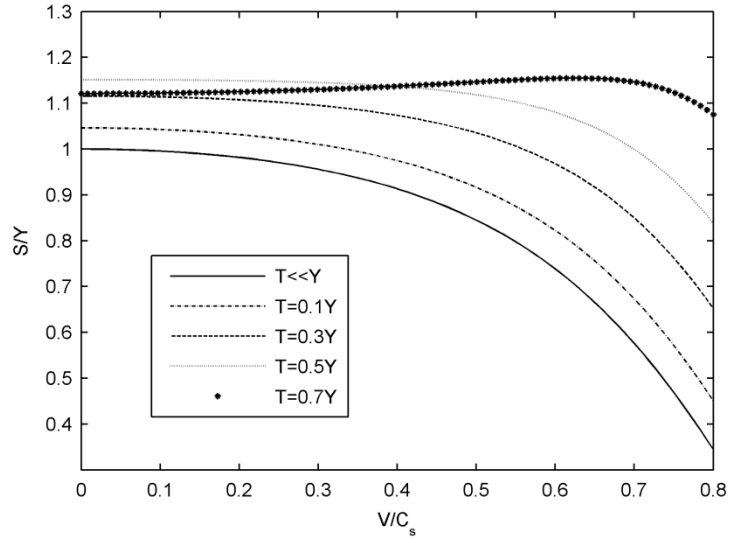

Fig. 3.2 Variations of the uniform traction force S with crack speed V given by the simple model without hardening ($\kappa = 2.1$, C_s is the transverse elastic wave speed, Y is the material yielding stress.).

Clearly, from Eq. (3.17) and (3.35), one can see that when $V \to C_R$, $R_a \to \infty$ and $S \to T$. Thus it follows from Eq. (3.36) that $c' \to \infty$ when $V \to C_R$. Therefore, to ensure a finite cohesive zone length, the crack speed must be lower than C_R.

Dependence of the constant traction force S on crack speed is shown in Fig. 3.2. It is seen from Fig. 3.2 that when $T \leq 0.5Y$, the normal traction force S in cohesive zone decreases with crack speed while it increases with remote tensile loading. In particular, due to the increase of $R_a(V)$ with increasing speed, the traction force decreases quickly with crack speed after $V = 0.2C_s$, which indicates that the dependence of traction force S on crack speed is significant and cannot be neglected at high crack speed ($V > 0.2C_s$). In addition, different from the classical Dugdale model of steady-state moving crack in (Goodier and Field, 1963; Kanninen, 1968) which gives a constant cohesive zone length, it is seen from Eq. (3.35) and (3.36) that the cohesive zone length c' predicted by the present model increases monotonously with crack speed under low and moderate remote loading ($T \leq 0.5Y$). Dependence of the cohesive zone length on remote loading is shown in Fig. 3.3. It is seen from Fig. 3.3 that the cohesive zone length increases with remote loading, and the effect of crack speed on cohesive zone length varies with

remote loading and becomes insignificant when $T = 0.7Y$. This can be confirmed from Fig. 3.2 which shows that the dependence of traction force S on crack speeds is not significant when $T = 0.7Y$.

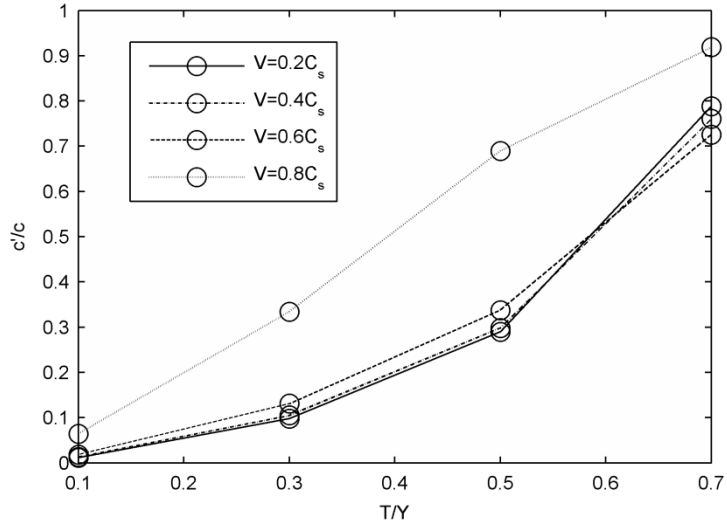

Fig. 3.3 Relation between cohesive zone length c' and remote loading T at different crack speeds given by the simple model without hardening ($\kappa = 2.1$).

On the other hand, the crack tip opening displacement (CTOD) δ at the crack tip $|z| = c$ can be obtained by Eq. (3.32)

$$\delta = \frac{4S}{\pi\mu} A(V) c \ln\left(\frac{c + c'}{c}\right) \tag{3.37}$$

The associated fracture energy in cohesive zone can be determined by Eq. (3.34)

$$G = \frac{4S^2}{\pi\mu} A(V) c \ln\left(\frac{c + c'}{c}\right) \tag{3.38}$$

The speed effect on CTOD δ and fracture energy G are shown in Fig. 3.4 and 3.5. In Fig. 3.4, δ_0 is the CTOD obtained from classical Dugdale model under the same remote loading T but at $V = 0$. It is seen from Fig. 3.4 that, CTOD predicted by the present model increases more rapidly with crack speed than classical Dugdale model. Furthermore, different from the classical Dugdale model which gives a T-independent δ-V relation, the δ-V relation given by the present model is influenced by remote loading T. In addition, the relation between fracture energy G and crack speed V is shown in Fig. 3.5, where G_0 is the fracture energy obtained from classical

Dugdale model under the same remote loading T but at $V = 0$.

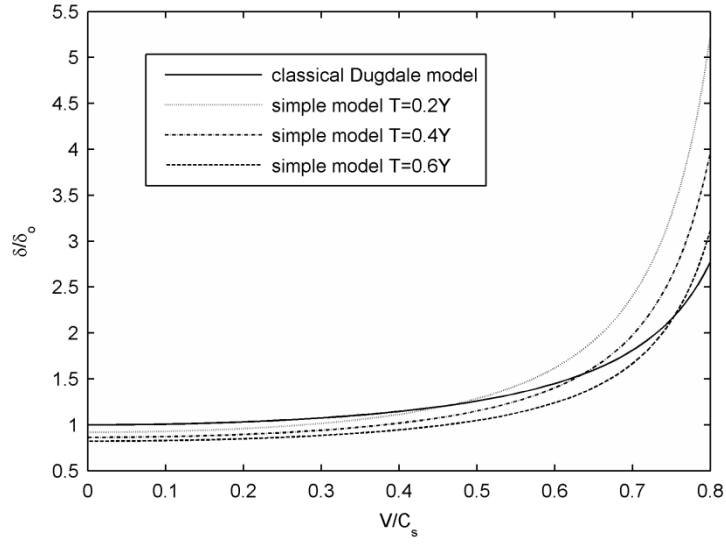

Fig. 3.4 Relation between δ (CTOD) and crack speed V given by the simple model ($\kappa = 2.1$), where δ_0 is the CTOD given by classical Dugdale model under the same remote loading T but at $V = 0$.

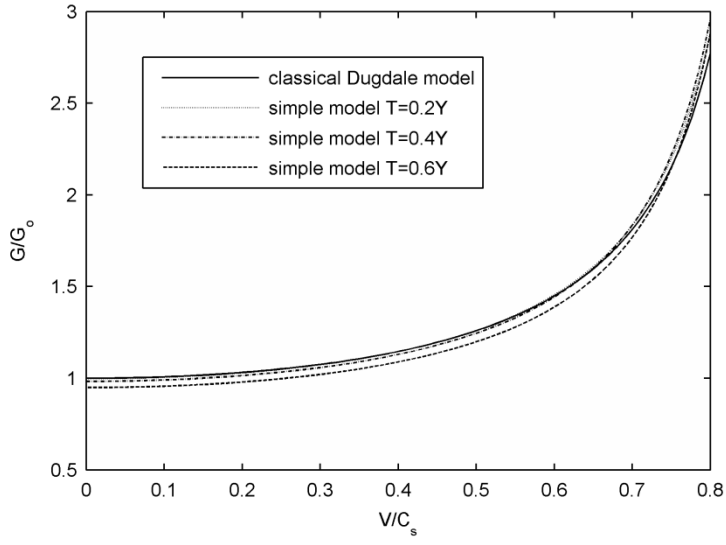

Fig. 3.5 Relation between fracture energy G and crack speed V given by the simple model ($\kappa = 2.1$), where G_0 is the fracture energy given by classical Dugdale model under the same remote loading T but at $V = 0$.

It is seen from Fig. 3.5 that, at high crack speed, although the present simple model gives a very different traction force in cohesive zone, the G-V relations predicted by the classical Dugdale model and the present simple model are quite similar. This is not surprising because larger traction force introduces a smaller cohesive zone length and CTOD, which lead to a similar fracture energy (the product of traction force and CTOD). In particular, when $T << S$, from Eq. (3.36) and (3.38), it can be seen that $G \approx A(V)\pi c T^2/2\mu$, which is independent of traction

force S. It can be seen from Fig. 3.2-3.5 that, under small or moderate loadings ($T \leq 0.5Y$), the present simple model gives a larger cohesive zone length and CTOD, but a similar fracture energy at high crack speed as compared with classical Dugdale model.

3.3.2 A polynomial model with hardening (plane stress)

In general, however, the traction force could be non-uniform on the cohesive zone (Volokh, 2004; Williams and Hadavinia, 2002) especially due to hardening. Traction-separation law is convenient to be employed in numerical simulation but difficult to be used in analytical analysis. To pursue explicit results, traction distribution as a function of the coordinate x is assumed in the present paper, as well as in some other papers (Bhargava and Bansal, 2002; Daniewicz, 1994; Harrop, 1978; Wnuk and Legat, 2002). Here, we consider a general case when the cohesive force $P(x)$ is a polynomial of x and specified by four parameters: the values of traction at the two ends of the cohesive zone, plus the value and location of the maximum traction on the cohesive zone. For this end, let us adopt the following assumptions:

i) Initial yielding at the end of cohesive zone: at the end of cohesive zone ($|x| = c+c'$) where the material starts to yield (Wnuk and Legat, 2002), the traction force is equal to initial yielding traction force S_0 defined by Eq. (3.35) (by setting $Y = Y_0$ on RHS of (3.35), where Y_0 is the initial yielding stress of material of hardening. Material is under plane stress condition.).

ii) The maximum value of traction: In the present paper, we set $\sigma_{max}=mS_0$, where m ($m \geq 1$) is a dimensionless parameter which measures the strain hardening (the maximum value of traction) and is independent of crack speed. Clearly, the mean traction force along cohesive zone increases with m thus the cohesive zone length decreases with m.

iii) Location of the maximum traction: the maximum traction occurs at $|x_m| = c+c'\Delta$, where x_m is the coordinate of maximum traction location, Δ is assumed to be a dimensionless material property ($0 \leq \Delta \leq 1$) independent of crack speed and determined by material ductility (Wnuk and Legat, 2002; Wnuk and Mura, 1983). It defines the location of maximum traction in cohesive

zone. In the present paper, for a sixth-order even polynomial, to ensure a positive traction force along the entire cohesive zone, it turns out that $0.1 < \Delta < 0.9$. Therefore, the material experiences strain hardening on the interval (c+c'Δ < |x| < c+c') and strain softening within c < |x| < c+c'Δ. Clearly, the mean traction force along cohesive zone decreases with Δ thus the cohesive zone length increases with Δ.

iv) Traction vanishes at the crack tip: the traction force reduces to zero at the other end of cohesive zone (|x|= c) (Volokh, 2004; Williams and Hadavinia, 2002).

Therefore, with given material property Δ and the dimensionless parameter m ($m \geq 1$), a sixth-order even polynomial $P(x)$ with 4 coefficients A_0, A_2, A_4 and A_6 can be determined uniquely to meet the following 4 conditions

$$P(c) = 0,\ P(c + c') = S_0(V, T, Y_0),\ P'(x_m) = 0,\ P(x_m) = mS_0(V, T, Y_0) \tag{3.39}$$

In doing so, the 4 real coefficients A_0, A_2, A_4 and A_6 will be determined by the crack speed V, remote loading T, the initial yielding stress Y_0, the material ductility property Δ, hardening parameter m, crack length $2c$, and the cohesive zone length c'. Substituting A_0, A_2, A_4, and A_6 into Eq. (3.30), the cohesive zone length c' can be determined. Finally, stress and displacement fields can be obtained from Eq. (3.10), (3.25), (3.29) and (3.32).

For example, for a crack under remote loading $T = 0.4Y_0$, assuming that $\Delta = 0.7$ and $m = 1.5$ (Adams et al., 2001; Bucaille et al., 2006; Livne et al., 2010; Wnuk and Mura, 1983) (for materials with moderate hardening and the hardening zone is relatively small), the traction distribution at different crack speed is shown in Fig. 3.6 ($\kappa = 1.7$). Furthermore, the effect of material parameters m and Δ on cohesive zone length is shown in Fig 3.7. From Fig. 3.7, it can be seen that, similar as the previous simple model discussed in section 3.3.1, the cohesive zone length given by the present polynomial model increases with crack speed under moderate loading $T = 0.4Y_0$. The zone length is determined by both values of m and Δ, and decreases with the hardening parameter m. In addition, it is found that when setting $m = 1.24$, $\Delta = 0.7$ (in this case, the average traction force in cohesive zone is about $0.92S_0$), the dependence of cohesive zone length on crack speed predicted by the present sixth-order polynomial model is quite

similar to the previous simple model given in section 3.3.1.

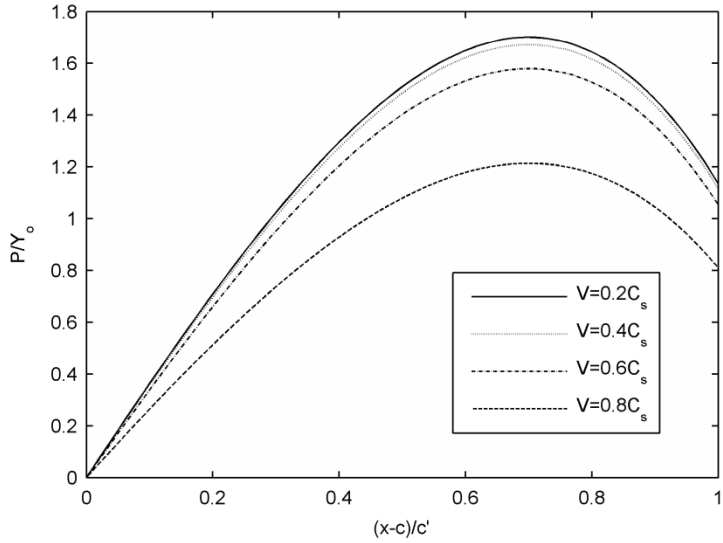

Fig. 3.6 Variations of traction force $P(x)$ with crack speed V given by the polynomial model with hardening ($T = 0.4Y_0$, $\kappa = 1.7$, $\Delta = 0.7$, $m = 1.5$. Y_0 is the material initial yielding stress.).

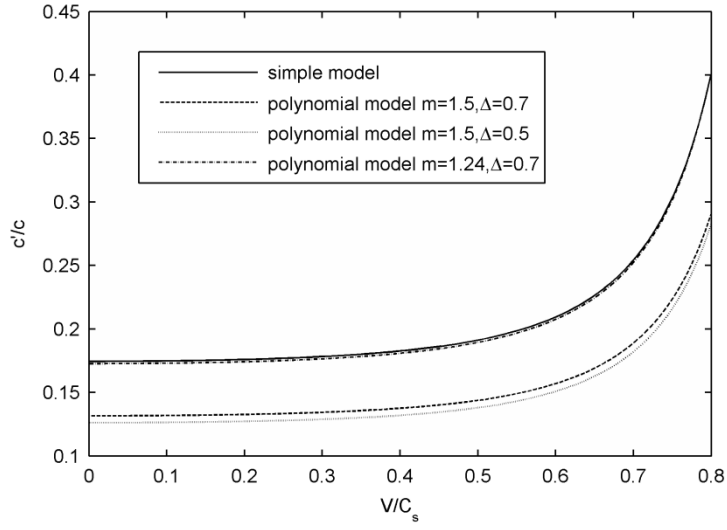

Fig. 3.7 Variations of normalized cohesive zone length c'/c with crack speed V given by the polynomial model and simple model ($T = 0.4Y_0$, $\kappa = 1.7$).

To explore the effect of non-uniform traction distribution given by the polynomial model, we calculated the CTOD based on the simple model and the polynomial model with $m = 1.24$, $\Delta = 0.7$, respectively. From Eq. (3.32), the CTOD for the polynomial model and the simple model is evaluated numerically under different loading conditions, and the results are shown in Fig. 3.8. In Fig. 3.8, δ_0 is the CTOD obtained by the simple model under the same remote loading T but at

$V = 0$. From Fig. 3.7 and 3.8, it can be seen that although the simple model and the polynomial model give almost same cohesive zone length, the CTOD predicted by the two models are quite different. Generally, the CTOD given by the polynomial model is about 30% larger than that given by the simple model. And the difference given by the two models increases with the remote loading and crack speed (for example, the differences is about 40% at $V = 0.8C_s$, $T = 0.6Y_0$), which indicates that the effect of non-uniformity of traction increases with the length of cohesive zone.

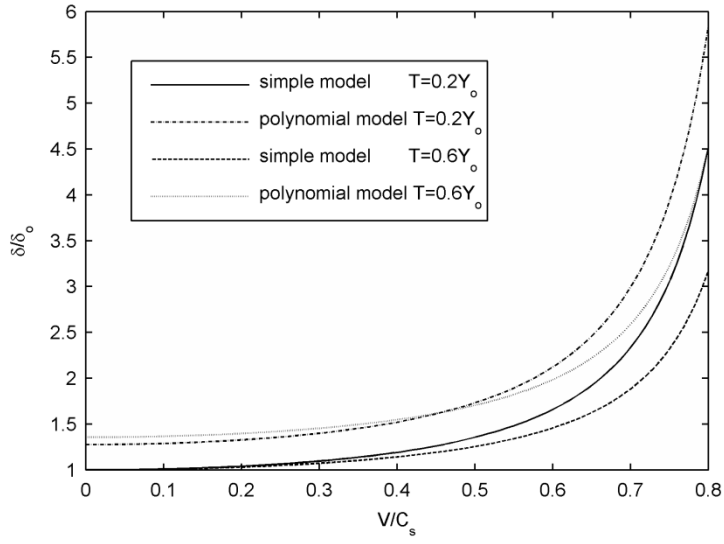

Fig. 3.8 Relation between δ (CTOD) and crack speed V given by the simple model and the polynomial model ($\kappa = 1.7$, $\Delta = 0.7$, $m = 1.24$. δ_0 is the CTOD given by the simple model under the same remote loading T but at $V = 0$.).

Therefore, the opening displacement of the cohesive zone is significantly influenced by the non-uniformity of traction distribution. For example, in reference (Döll, 1983), in static case, the crack face profiles predicted by the classical Dugdale model are shown in reasonable agreement with experimental data of some materials but deviates for a polycarbonate sheet (Fig. 8 in (Döll, 1983)). In our Fig. 3.9a, we evaluate the crack face profiles using the present simple model and the polynomial model. Since the problem is under small yielding condition, we set $T = 0.05Y_0$ and $T = 0.1Y_0$. From Fig. 3.9a, it can be seen that under small scale yielding condition, the crack face profiles given by the present polynomial model are insensitive to remote loading and largely determined by the material parameters m and Δ. For instance, in Fig. 3.9a, the crack faces predicted by the polynomial model ($m = 1.04$, $\Delta = 0.85$) under $T = 0.05Y_0$ (solid line) and $T = 0.1Y_0$ (dash-dot line) are indistinguishable with each other. Based on the experimental data

about CTOD (δ = 4.3μm) at the point near crack tip ($x-c$ = 2.4μm), using the numerical results of Eq. (3.32), one gets $(\kappa+1)Y_0/\pi\mu$ = 0.054 for both the simple model and the polynomial model with m = 1.04 and Δ = 0.85, and $(\kappa+1)Y_0/\pi\mu$ = 0.045 for the polynomial model with m = 1.1 and Δ = 0.85. By setting V = 0, the crack face profiles predicted by the simple model with $(\kappa+1)Y_0/\pi\mu$ = 0.054, the polynomial model with m = 1.04, Δ = 0.85 and $(\kappa+1)Y_0/\pi\mu$ = 0.054, the polynomial model with m = 1.1, Δ = 0.85 and $(\kappa+1)Y_0/\pi\mu$ = 0.045 are shown in Fig. 3.9a. From Fig. 3.9a, it can be seen that, the polynomial model with m = 1.04 and Δ = 0.85 best fits the experimental data. Thus, compared with the simple model, the polynomial model with adjustable parameters m and Δ is in better agreement with experimental data given in (Döll, 1983) and has the potential to capture main features of both the crack face profile and cohesive zone length. In addition, the associated traction-separation laws derived from the polynomial models with different m and Δ are shown in Fig. 3.9b.

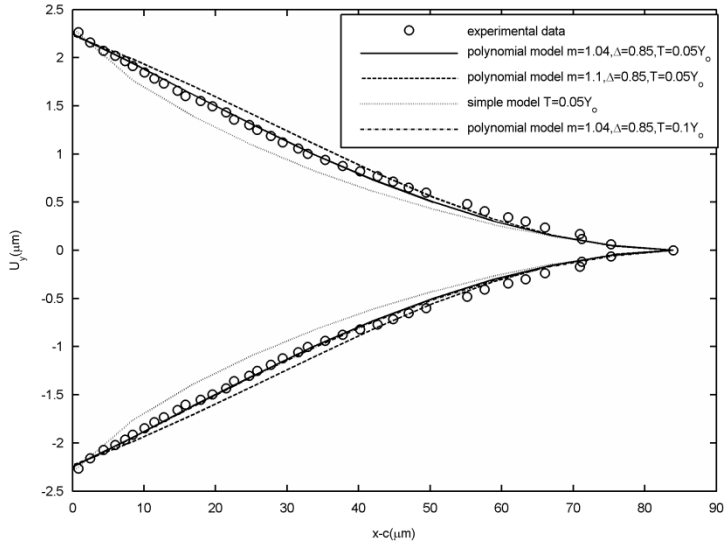

Fig. 3.9a Cohesive zone profiles given by the simple model and the polynomial model, where $x-c$ is the distance to crack tip, u_y is the y-displacement of the cohesive zone faces. The crack profiles are obtained by the simple model with $(\kappa+1)Y_0/\pi\mu$ = 0.054, or the polynomial model with m = 1.04, Δ = 0.85 and $(\kappa+1)Y_0/\pi\mu$ = 0.045, or the polynomial model with m = 1.1, Δ = 0.85 and $(\kappa+1)Y_0/\pi\mu$ = 0.045.

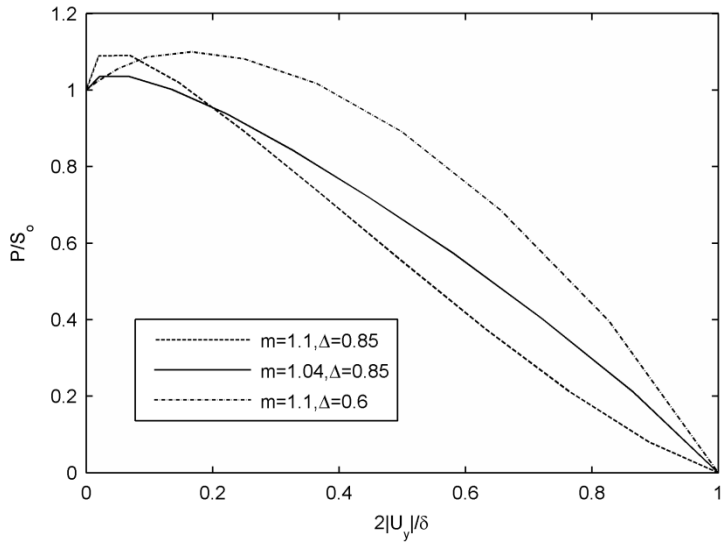

Fig. 3.9b Traction-separation laws derived from the polynomial models with different m and Δ.

On the other hand, the fracture energy are calculated based on the simple model and the polynomial model with m = 1.24, Δ = 0.7. As discussed above, these two models give almost same cohesive zone length for a wide range of crack speeds. The fracture energy given by the two models is shown in Fig. 3.10, where G_0 is the fracture energy given by the simple model under the same remote loading T but at V = 0. From Fig. 3.8-3.10, it can be seen that although the two models predict different CTOD, the fracture energy given by the two models are very similar (the difference is no more than 10% at $V = 0.8C_s$, $T = 0.6Y_0$), especially under low remote loading $T = 0.2Y_0$. Therefore, from Fig. 3.7-3.10, it can be concluded that: i) the form of traction distribution in cohesive zone significantly influences the crack tip profiles and CTOD; ii) fracture energy is much less sensitive to the non-uniformity of traction distribution. This conclusion is consistent with reference (Williams and Hadavinia, 2002) which states that the fracture energy is insensitive to the shape of traction-separation law. However, the non-uniformity of traction distribution gives a more reasonable crack faces profiles for some materials (Döll, 1983) thus has the potential to better capture fracture phenomenon of ductile materials with strain hardening in cohesive zone.

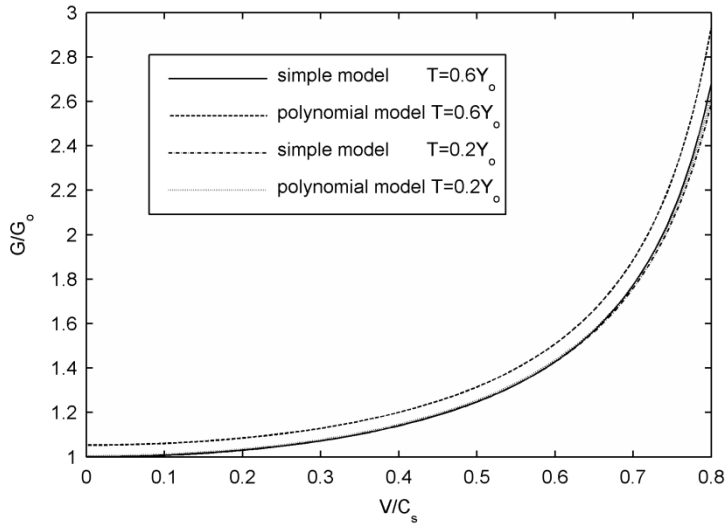

Fig. 3.10 Relation between fracture energy G and crack speed V given by the simple model and the polynomial model ($\kappa = 1.7$, $\Delta = 0.7$, $m = 1.24$. G_0 is the fracture energy given by the simple model under the same remote loading T but at $V = 0$.).

3.4 Further comparison to experimental data

Here let us further compare our results with available experiments in the simple case when traction $P(x)$ is a constant S, as discussed in section 3.3.1. In reference (Livne et al., 2010), a nonlinear zone is observed near moving crack tip in a polyacrylamide gel sheet, which cannot be explained by linear elastic fracture mechanics. For comparison, we choose the nonlinear zone length obtained from (Livne et al., 2010) as the cohesive zone length c' defined in the present model. Thus, fracture energy G at different crack speeds predicted by the present simple model is given by Eq. (3.38). Assuming that $c' << c$ and $T << Y$, we have $c\ln(1+c'/c) \approx c'$ in Eq. (3.38). On the other hand, from test data of (Livne et al., 2010), we have fracture energy $G = 14\text{J/m}^2$ and cohesive zone length $c' = 0.038\text{mm}$ at $V = 0.34C_s$ (see Fig. 2 and Fig. 4 in (Livne et al., 2010)). Using these two values of test, the present simple model (see Eq. (3.35) and (3.38)) gives the value of $Y^2/\mu = 0.4\text{MPa}$. Assuming μ is a constant independent of crack speed and $\nu = 0.5$ (Livne et al., 2010), fracture energy at different crack speed predicted by the present simple

model (with $P(x) = S$, from Eq. (3.35) and (3.38)) is shown in Fig. 3.11 with comparison to classical Dugdale model and experimental data of (Livne et al., 2010). It is seen from Fig. 3.11 that, as compared to classical Dugdale model, the present model is in much better agreement with the test results of (Livne et al., 2010) especially at high crack speeds. Actually, the difference between the present simple model and classical Dugdale model is not significant when $V < 0.4C_s$, which confirms that the speed effect predicted by the present model becomes significant especially for high crack speeds. At higher crack speed, when $V > 0.4C_s$, the differences between the present simple model and classical Dugdale model increases rapidly with crack speed. For example, at $V = 0.78C_s$, fracture energy predicted by classical Dugdale model is nearly 10 times the experimental result (Livne et al., 2010), while the result given by the present simple model is only about 40% higher than the experimental result. In addition, if strain rate effect on yielding stress Y is considered, traction force in cohesive zone will increase with crack speed, which leads to a larger fracture energy at high crack speed thus the results in Fig. 3.11 will deviates from experimental data. Also, from Fig. 3.2 it can be seen that the traction force decreases to blow 40% of its original value at high crack speed. Thus, it is reasonable to assume that the inertia effect dominates at high crack speed and is mainly responsible for physically reasonable fracture energy at high crack speed. These results show that the speed-dependence of traction force, as predicted by the present model, is essential to explain some known test results of nonlinear/ductile materials especially at high crack speeds.

Furthermore, if non-uniform traction distribution is considered, as discussed in section 3.2, it can be seen from Fig. 3.7 and 3.10 that under low remote loading, c'-V relation and G-V relation given by the present polynomial model are insensitive to the non-uniformity of traction distribution. Thus, the polynomial model will predict a similar G-V relation as the simple model without hardening.

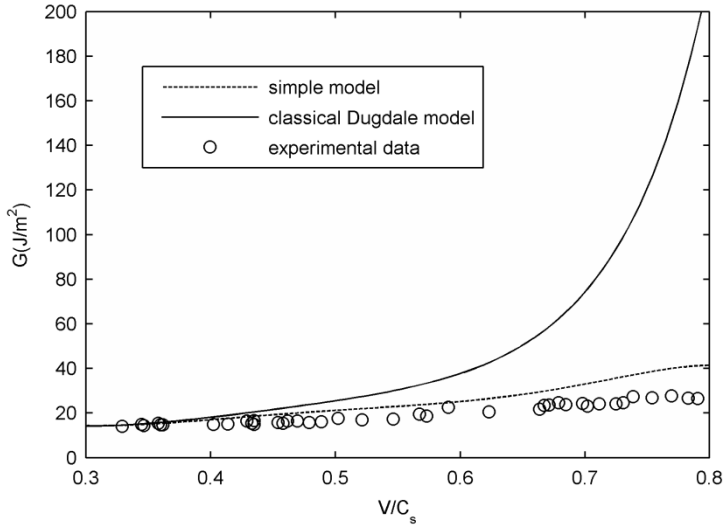

Fig. 3.11 Relation between fracture energy G and crack speed V given by the classical Dugdale model and the present simple model (without hardening). ($\kappa = 1.7$)

3.5 Conclusions

A steady-state moving crack of Yoffe-type is studied with a modified cohesive zone model. New features of this modified model are that the effects of the normal stress parallel to the crack axis and the non-uniformity of normal traction force in cohesive zone are examined, and non-uniform traction force on the cohesive zone is expressed by an arbitrary symmetric polynomial to be determined by specific yielding criterion imposed on the cohesive zone. The main conclusions can be summarized as:

i) For materials defined by von Mises criterion without hardening, it is shown that the normal traction force is a speed-dependent constant which could be even much smaller than the normal stress parallel to the crack axis at high crack speed. Unlike the classical Dugdale model of a moving crack which predicts a speed-independent cohesive zone length, the present model predicts that the cohesive zone length increases with crack speed under lower or moderate remote mode-I loading.

ii) Effect of non-uniformity of traction distribution is studied with a polynomial model in which

the traction is expressed by a sixth-order symmetric polynomial with four coefficients determined by the value and location of the maximum traction and the values of traction at two ends of the cohesive zone. Numerical results show that the non-uniformity of traction distribution significantly influences the opening displacement of cohesive zone, and the polynomial model predicts a more reasonable crack face profile than the simple model without hardening as compared with experimental data.

iii) Comparison with some known experimental data shows that the present model is in better agreement with experimental data than the classical Dugdale model especially at higher crack speeds.

These results suggest that the present model is plausible to capture some speed effects on the cohesive traction and associated fracture energy at higher crack speed.

Chapter 4: A modified speed-dependent cohesive zone model for a high-speed self-similar expanding crack

4.1 Introduction

In this chapter, the speed-dependent cohesive zone model presented in chapter 3 is applied to a self-similar expanding crack problem. It is well known that large plastic deformations are often involved near the crack tip in ductile materials. Thus, to describe the stress field in this region, the cohesive zone models, were proposed by Barenblatt (Barenblatt, 1959) and Dugdale (Dugdale, 1960) for a static crack, and have been applied to dynamic crack problems of nonlinear or ductile materials (Atkinson, 1968; Goodier and Field, 1963; Kanninen, 1968; Wu and Huang, 2013). In these works, the materials in cohesive zone along crack faces are assumed to be yield and become the part of the crack faces while crack is propagating. A major assumption in these models (Dugdale model) is that the normal traction force in the cohesive zone is constant and equal to the yielding stress of the material. With such an assumption, for example, the role of the normal stress parallel to the crack faces is completely ignored in the yielding condition in the cohesive zone. However, it is known that high crack speed influences crack tip stress state and causes high inertia zone near crack tip. As a result, other stress components, especially the normal stress σ_{xx} parallel to the crack axis, comes to play an important role in the yielding condition in the cohesive zone at high crack speed. Moreover, Sousa et al. (Sousa et al., 2013) shows that the constant T-stress parallel to crack axis influences the plastic zone size near a static crack tip and cannot be ignored under moderate loading conditions; Jayadevan et al. (Jayadevan et al., 2003) shows that the fracture toughness is enhanced significantly with negative T-stress parallel to crack axis in a numerical analysis. These studies (Jayadevan et al., 2003; Sousa et al., 2013) suggested that the normal stress parallel to the crack axis, σ_{xx}, significantly influences fracture process in ductile materials, a

phenomenon which cannot be studied by the above-mentioned existing models (Atkinson, 1968; Goodier and Field, 1963; Kanninen, 1968; Wu and Huang, 2013). Therefore, the effects of σ_{xx} on the cohesive zone have recently drawn considerable attentions for static cracks (Siegmund and Brocks, 2000). However, to the best of my knowledge, little attention has been paid to dynamic cracks in ductile materials based on analytic cohesive zone models. In addition, non-uniform traction force in the cohesive zone has not been considered in previous analytic models. However, strain hardening (or softening) of materials are often involved in cohesive zone thus the traction usually are not constant along the zone (Siegmund and Brocks, 2000). Therefore, non-uniform traction distribution is studied in this chapter, and the effect of σ_{xx}, combined with remote loading T, on traction force, cohesive zone length, crack tip opening displacement (CTOD) and energy release rate near an expanding crack tip is discussed.

Thus, in this chapter, self-similar high-speed crack propagation is studied with a modified cohesive zone model. With the present model, the normal traction distribution and the normal stress parallel to the crack in the cohesive zone are to be determined by satisfying the specific yielding criterion in the cohesive zone. It is shown in section 4.3 that for a ductile material defined by von Mises criterion without hardening, the traction force on cohesive zone is a constant and depends on crack speed V_a and mode-I remote loading T. In particular, the present model confirms that the normal stress parallel to the crack faces, which has been ignored in previous related studies (Atkinson, 1968; Goodier and Field, 1963; Kanninen, 1968; Wu and Huang, 2013), can be larger than the normal stress perpendicular to the crack faces at high crack speed and thus play an important role in the cohesive zone. In addition, as shown in section 4.3.1, at high crack speed, the cohesive zone length given by the present model is 2 times the zone length predicted by the classical Dugdale model. The CTOD and energy release rate calculated by the present model in section 4.3.2, are shown to decrease with increasing crack speed. In section 4.4, strain hardening effect is examined with a non-uniform traction distribution in the cohesive zone. Comparison between a self-similar expanding crack and a Yoffe- type steady-state moving crack based on the present model is discussed in section 4.5.

Finally, the main conclusions are summarized in section 4.6.

4.2 A modified cohesive zone model for a self-similar expanding crack

Let us consider a central crack lying on the x'-axis in an infinite elastic plane, which has an initial length 0 at $t = 0$ and expands at both tips along x' axis, with the tip velocity V_a. The crack surfaces are under uniform pressure $-T$, where T corresponds to the mode-I remote loading. In addition, two symmetric cohesive zones, ahead of the two crack tips, expanding at the velocity of V_c and are under force $S_y - T$, where S_y is the traction on the cohesive zone (see Fig. 4.1). Unlike classical Dugdale model and previous related models studies (Atkinson, 1968; Goodier and Field, 1963; Kanninen, 1968; Wu and Huang, 2013) in which the traction S_y on the cohesive zone is taken as the yielding stress Y of material, the traction S_y in the present model is to be determined by satisfying specific yielding criterion on the cohesive zone.

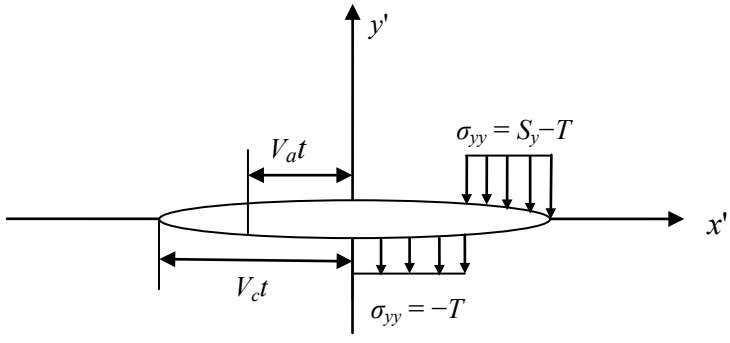

Fig. 4.1 A self-similar expanding crack with cohesive zones ahead of crack tips.

It is known that for the present plane dynamic elastic problem, similar as Eq. (3.1) in chapter 3, the two displacement components (u_x, u_y) at time t can be given in terms of two wave functions $\varsigma(x', y', t)$ and $\psi(x', y', t)$ (Craggs, 1960)

$$u_x = \frac{\partial \varsigma}{\partial x'} + \frac{\partial \psi}{\partial y'}, \qquad u_y = \frac{\partial \varsigma}{\partial y'} - \frac{\partial \psi}{\partial x'} \tag{4.1}$$

and the two wave functions meet motion equations

$$\frac{\partial^2 \varsigma}{\partial x'^2}+\frac{\partial^2 \varsigma}{\partial y'^2}-\frac{1}{C_d^{\,2}}\frac{\partial^2 \varsigma}{\partial t^2}=0,$$
$$\frac{\partial^2 \psi}{\partial x'^2}+\frac{\partial^2 \psi}{\partial y'^2}-\frac{1}{C_s^{\,2}}\frac{\partial^2 \psi}{\partial t^2}=0 \tag{4.2}$$

where, C_d and C_s are longitudinal and transverse elastic wave speeds defined by Eq. (3.4). And the boundary conditions of the present problem are

$$\begin{aligned}
&\sigma_{yy}=-T && \text{as} \quad |x'|<V_a t,\ \ y'=0\\
&\sigma_{yy}=S_y-T && \text{as} \quad V_a t<|x'|<V_c t,\ \ y'=0\\
&\sigma_{xy}=0 && \text{as} \quad y'=0\\
&u_y=0 && \text{as} \quad y'=0,\ |x'|>V_c t
\end{aligned} \tag{4.3}$$

with the asymptotic conditions that all stresses vanish at the infinity.

For self-similar plane problems, stresses and velocities depend on the two combinations t/x' and t/y' and thus are homogeneous functions of x', y' and t of degree zero. As a result, the number of independent variables for stresses and velocities is reduced from three to two. Consequently, for the present mode-I expanding crack problem, as shown in reference (Freund, 1990) that the eight related functions on the left of the following Eq. (4.4) and (4.5) depend on two combinations of x', y' and t and eventually can be given in terms of eight respective analytical functions (F_{xx}, F_{xy}, F_{yy}, F_{yt}, G_{xx}, G_{xy}, G_{yy}, G_{xt}) on the right of Eq. (4.4) and (4.5) as

$$\mu\frac{\partial^2 \varsigma}{\partial x'^2}=\mathrm{Re}\{F_{xx}(\zeta_d)\},\quad \mu\frac{\partial^2 \varsigma}{\partial x'\partial y'}=\mathrm{Im}\{F_{xy}(\zeta_d)\},\ \mu\frac{\partial^2 \varsigma}{\partial y'^2}=\mathrm{Re}\{F_{yy}(\zeta_d)\},\ \mu\frac{\partial^2 \varsigma}{\partial y'\partial t}=\mathrm{Im}\{F_{yt}(\zeta_d)\} \tag{4.4}$$

and

$$\mu\frac{\partial^2 \psi}{\partial x'^2}=\mathrm{Im}\{G_{xx}(\zeta_s)\},\ \mu\frac{\partial^2 \psi}{\partial x'\partial y'}=\mathrm{Re}\{G_{xy}(\zeta_s)\},\quad \mu\frac{\partial^2 \psi}{\partial y'^2}=\mathrm{Im}\{G_{yy}(\zeta_s)\},\ \mu\frac{\partial^2 \psi}{\partial x'\partial t}=\mathrm{Im}\{G_{xt}(\zeta_s)\} \tag{4.5}$$

where F_{xx}, ..., G_{xt} are eight functions (which are analytical in the entire complex plane except the crack, cohesive zone, and the circular wave front) of the two complex variables ζ_d and ζ_s defined

by (Freund, 1990)

$$\zeta_d = \xi + i\eta_1 = \frac{x'}{r^2}t + i\frac{y'}{r^2}\sqrt{t^2 - \frac{r^2}{C_d^{\,2}}},\quad \zeta_s = \xi + i\eta_2 = \frac{x'}{r^2}t + i\frac{y'}{r^2}\sqrt{t^2 - \frac{r^2}{C_s^{\,2}}} \tag{4.6}$$

where $r = (x'^2+y'^2)^{1/2} < C_d t$. In particular, along the crack faces and the cohesive zone we have $\zeta_d = \zeta_s = \zeta$, and the interval of $V_a t < |x'| < V_c t$ at $y' = 0$ is then mapped into $V_c^{-1} < |\xi| < V_a^{-1}$, the interval of $0 < |x'| < V_a t$ at $y' = 0$ is mapped into $|\xi| > V_a^{-1}$, and the circular wave front $r = C_d t$ in the physical plane is mapped into $0 \le |\xi| \le C_d^{-1}$. For the present 2D plane problem, only two of the above eight analytical functions are independent. Actually, as shown in reference (Freund, 1990) from Eq. (4.4-4.6) that for the present mode-I problem the following six relations hold between the eight functions (F_{xx}, ……G_{xt})

$$\begin{aligned}
&(\zeta_d^{\,2} - C_d^{\,-2})F'_{xx}(\zeta_d) = \zeta_d\sqrt{\zeta_d^{\,2} - C_d^{\,-2}}F'_{xy}(\zeta_d) = -\zeta_d^{\,2}F'_{yy}(\zeta_d) = -\zeta_d^{\,2}\sqrt{\zeta_d^{\,2} - C_d^{\,-2}}F'_{yt}(\zeta_d),\\
&(\zeta_s^{\,2} - C_s^{\,-2})G'_{xx}(\zeta_s) = -\zeta_s\sqrt{\zeta_s^{\,2} - C_s^{\,-2}}G'_{xy}(\zeta_s) = -\zeta_s^{\,2}G'_{yy}(\zeta_s) = -\zeta_s(\zeta_s^{\,2} - C_s^{\,-2})G'_{xt}(\zeta_s)
\end{aligned} \tag{4.7}$$

which effectively reduces the number of independent functions from eight to two. Furthermore, the stress field then can be described as (Freund, 1990)

$$\begin{aligned}
\sigma_{xx} &= \mathrm{Re}\left\{\frac{C_d^{\,2}}{C_s^{\,2}}F_{xx}(\zeta_d) + \left(\frac{C_d^{\,2}}{C_s^{\,2}} - 2\right)F_{yy}(\zeta_d) + 2G_{xy}(\zeta_s)\right\}\\
\sigma_{yy} &= \mathrm{Re}\left\{\left(\frac{C_d^{\,2}}{C_s^{\,2}} - 2\right)F_{xx}(\zeta_d) + \frac{C_d^{\,2}}{C_s^{\,2}}F_{yy}(\zeta_d) - 2G_{xy}(\zeta_s)\right\}\\
\sigma_{xy} &= \mathrm{Im}\left\{2F_{xy}(\zeta_d) + G_{yy}(\zeta_s) - G_{xx}(\zeta_s)\right\}
\end{aligned} \tag{4.8}$$

Final determination of all analytical functions depends on the boundary conditions. In view of the presence of the cohesive zone, the present problem has different boundary conditions on the cohesive zone than the elastic mode-I crack (Freund, 1990). In particular, different than the elastic mode-I crack (Freund, 1990), the normal traction in the present problem suffers a discontinuity across the crack tip. Thus, the arguments and derivations used in reference (Freund, 1990) for the elastic mode-I crack need to be verified or modified for the present case. First of all, it can be seen that, similar to the case in reference (Freund, 1990; Georgiadis, 1991), shear stress vanish at circular wave front $r = C_d t$. Therefore, in view of the third equation in (4.8), the condition that the shear stress vanishes along the upper and lower faces of the crack, the

cohesive zone and the wave front (along which $\zeta_d = \zeta_s = \zeta$) gives

$$\begin{aligned} 2F'_{xy}(\zeta)^+ + G'_{yy}(\zeta)^+ - G'_{xx}(\zeta)^+ &= 2\overline{F'_{xy}}(\zeta)^- + \overline{G'_{yy}}(\zeta)^- - \overline{G'_{xx}}(\zeta)^-, \\ 2F'_{xy}(\zeta)^- + G'_{yy}(\zeta)^- - G'_{xx}(\zeta)^- &= 2\overline{F'_{xy}}(\zeta)^+ + \overline{G'_{yy}}(\zeta)^+ - \overline{G'_{xx}}(\zeta)^+ \end{aligned} \tag{4.9}$$

where the superscripts '+' and '−' denote the limit values from the upper and lower half -planes, respectively. Thus, from Eq. (4.9), the following combination is continuous across the crack, cohesive zone and wave front

$$\left[2F'_{xy}(\zeta) + G'_{yy}(\zeta) - G'_{xx}(\zeta) + 2\overline{F'_{xy}}(\zeta) + \overline{G'_{yy}}(\zeta) - \overline{G'_{xx}}(\zeta)\right]^+_- = 0 \tag{4.10}$$

On the other hand, from Eq. (4.7) and (4.8) and the first boundary conditions in (4.3), one gets on crack faces

$$\frac{\partial \sigma_{yy}}{\partial \xi} = \mathrm{Re}\left\{\frac{{C_d}^2}{{C_s}^2}\frac{\zeta}{\sqrt{\zeta^2 - {C_d}^{-2}}}F'_{xy}(\zeta) - \left(\frac{{C_d}^2}{{C_s}^2} - 2\right)\frac{\sqrt{\zeta^2 - {C_d}^{-2}}}{\zeta}F'_{xy}(\zeta) + 2\frac{\zeta}{\sqrt{\zeta^2 - {C_s}^{-2}}}G'_{yy}(\zeta)\right\} = 0 \tag{4.11}$$

In addition, it follows from Eq. (4.7) that $G_{yy}' = -G_{xx}'$ as $\zeta \to \infty$. Thus, from Eq. (4.11) one gets

$$\mathrm{Re}\left\{2F'_{xy}(\infty) + G'_{yy}(\infty) - G'_{xx}(\infty)\right\} = 0 \tag{4.12}$$

Therefore, from the principle of analytical continuation, it follows from Eq. (4.10) and (4.12) that

$$2F'_{xy}(\zeta) + G'_{yy}(\zeta) - G'_{xx}(\zeta) + 2\overline{F'_{xy}}(\zeta) + \overline{G'_{yy}}(\zeta) - \overline{G'_{xx}}(\zeta) = 0 \tag{4.13}$$

in the entire complex plane including the crack faces, the cohesive zone and wave front. Substituting Eq. (4.13) into Eq. (4.9), one gets that along the crack faces, cohesive zone and wave front

$$\left[2F'_{xy}(\zeta) + G'_{yy}(\zeta) - G'_{xx}(\zeta)\right]^+ + \left[2F'_{xy}(\zeta) + G'_{yy}(\zeta) - G'_{xx}(\zeta)\right]^- = 0 \tag{4.14}$$

This is a Hilbert problem and the solution bounded at the cohesive zone tips and $|x'| = C_d t$, $y' = 0$ is (Rice, 1968)

$$2F'_{xy}(\zeta) + G'_{yy}(\zeta) - G'_{xx}(\zeta) = 0 \tag{4.15}$$

Combined with Eq. (4.7), one gets

$$2\xi^2 F'_{yt}(\xi) + ({C_s}^{-2} - 2\xi^2)G'_{xt}(\xi) = 0 \tag{4.16}$$

Therefore, from Eq. (4.7) and (4.16), the number of independent functions is now further reduced to one. For example, it is verified from Eq. (4.7), (4.8) and (4.16) that the following equations hold at $y' = 0$, for the crack faces and the cohesive zone, respectively, in terms of the single analytical function $G_{xt}'(\xi)$ by

$$\begin{aligned}\frac{\partial \sigma_{yy}}{\partial \xi} &= \mathrm{Re}\left\{\frac{R_V(\xi)}{2\xi^2\sqrt{\xi^2 - C_d^{-2}}} G_{xt}'(\xi)\right\}, \\ \frac{\partial \sigma_{xx}}{\partial \xi} &= \mathrm{Re}\left\{\frac{2(C_s^{-2} - C_d^{-2})(C_s^{-2} - 2\xi^2) - R_V(\xi)}{2\xi^2\sqrt{\xi^2 - C_d^{-2}}} G_{xt}'(\xi)\right\}\end{aligned} \tag{4.17}$$

with

$$R_V(\xi) = (2\xi^2 - C_s^{-2})^2 - 4\xi^2\sqrt{\xi^2 - C_d^{-2}}\sqrt{\xi^2 - C_s^{-2}} \tag{4.18}$$

In particular, it is easily seen from Eq. (4.17) that σ_{yy} is constant on the cohesive zone implies that $G_{xt}'(\xi)$ must be purely imaginary on the cohesive zone, and thus σ_{xx} is also constant on the cohesive zone. On the other hand, since the normal traction suffers a discontinuity at the crack tip, it is seen from (4.17) that $G_{xt}'(\xi)$ has a simple pole at the crack tip. Thus, the final step is to determine $G_{xt}'(\xi)$ from the normal traction boundary conditions on the crack and cohesive zone. In what follows, this will be discussed for materials without or with strain hardening, respectively.

4.3 Materials defined by von Mises criterion without hardening

Let us first consider the materials without hardening defined by von Mises criterion with a constant yielding stress Y. Under plane stress condition, shear stress vanishes in the cohesive zone and the von Mises criterion in the cohesive zone is given by

$$\sigma_{xx}^2 + S_y^{\,2} - \sigma_{xx} S_y = Y^2 \tag{4.19}$$

As stated above, σ_{yy} is constant on the cohesive zone implies that σ_{xx} is constant on the cohesive

zone. Therefore, for materials without hardening defined by von Mises criterion (4.19) with a constant yielding stress Y, both S_y and σ_{xx} are constant on the cohesive zone. From Eq. (4.17) and the uniformity of normal traction on the crack faces and cohesive zone respectively, the real part of $G_{xt}'(\zeta)$ vanishes on the upper and lower faces of the crack and cohesive zone while $G_{xt}'(\zeta)$ has the crack tip as a simple pole. Thus the product $G_{xt}'(\zeta)(V_a^{-2}-\zeta^2)$ vanishes on the upper and lower faces of the crack and cohesive zone, without having the crack tip as a simple pole. This implies that on the faces of crack and cohesive zone

$$\begin{aligned}\left[\left(V_a^{-2}-\zeta^2\right)G_{xt}'(\zeta)\right]^+ + \left[\left(V_a^{-2}-\zeta^2\right)\overline{G_{xt}'}(\zeta)\right]^- = 0,\\ \left[\left(V_a^{-2}-\zeta^2\right)G_{xt}'(\zeta)\right]^- + \left[\left(V_a^{-2}-\zeta^2\right)\overline{G_{xt}'}(\zeta)\right]^+ = 0\end{aligned} \tag{4.20}$$

Thus, the product $G_{xt}'(\zeta)(V_a^{-2}-\zeta^2)$ is continuous across the crack and the cohesive zone

$$\left[\left(V_a^{-2}-\zeta^2\right)G_{xt}'(\zeta)-\left(V_a^{-2}-\zeta^2\right)\overline{G_{xt}'}(\zeta)\right]_-^+ = 0 \tag{4.21}$$

On the other hand, from Eq. (4.1), (4.4-4.7), similar as reference (Freund, 1990), one gets

$$\frac{\partial^2 u_y(\xi)}{\partial\xi\partial t} = -\operatorname{Im}\left\{\frac{C_s^{-2}}{2\mu\xi^2}G_{xt}'(\xi)\right\} \tag{4.22}$$

It follows from the fourth boundary condition in (4.3) that $\operatorname{Im}\{G_{xt}'(\xi)\}=0$ at $|\xi|\le V_c^{-1}$. Therefore, from the principle of analytical continuation, it follows from Eq. (4.21) that

$$\left(V_a^{-2}-\zeta^2\right)G_{xt}'(\zeta)-\left(V_a^{-2}-\xi^2\right)\overline{G_{xt}'}(\zeta)=0 \tag{4.23}$$

in the entire complex plane including the crack faces and cohesive zone. Substituting Eq. (4.23) into Eq. (4.20), one gets along the crack faces and cohesive zone

$$\left[\left(V_a^{-2}-\zeta^2\right)G_{xt}'(\zeta)\right]^+ + \left[\left(V_a^{-2}-\zeta^2\right)G_{xt}'(\zeta)\right]^- = 0 \tag{4.24}$$

This is a Hilbert problem for the product $G_{xt}'(\zeta)(V_a^{-2}-\zeta^2)$. In view of the continuous stress condition at wave front $r = C_d t$ for a linearly increasing force (Freund, 1990), the bounded solution for $G_{xt}'(\zeta)(V_a^{-2}-\zeta^2)$, which leads to $G_{xt}'(\zeta)$ having 1/2 singularity at the cohesive zone tips (while stress singularity at the cohesive zone tip is cancelled), is given by (Rice, 1968)

$$G_{xt}'(\zeta)=\frac{\zeta^2 P(\zeta)}{\sqrt{V_c^{-2}-\zeta^2}\left(V_a^{-2}-\zeta^2\right)} \tag{4.25}$$

where $P(\zeta)$ is an arbitrary polynomial of ζ with real coefficients. Furthermore, from the symmetric stress condition it can be verified that $P(\zeta)$ must be a symmetric polynomial. It can be verified from Eq. (4.22) and (4.25) that the single displacement condition can be met if $P(\zeta)$ is a symmetric polynomial. In addition, to ensure a finite particle velocity when $t\to\infty$, from Eq. (4.22), $P(\zeta)$ must be a constant C. Thus, noticing that $\sigma_{yy} = 0$ at the wave front, it follows from the first and second boundary condition in (4.3) that

$$\begin{aligned}
&\mathrm{Re}\left\{\int_{C_d^{-1}}^{V_a^{-1}-}\frac{R_V(\xi)C}{2\sqrt{\xi^2-C_d^{-2}}\sqrt{V_c^{-2}-\xi^2}\left(V_a^{-2}-\xi^2\right)}d\xi\right\}=S_y-T,\\
&\mathrm{Re}\left\{\int_{C_d^{-1}}^{V_a^{-1}+}\frac{R_V(\xi)C}{2\sqrt{\xi^2-C_d^{-2}}\sqrt{V_c^{-2}-\xi^2}\left(V_a^{-2}-\xi^2\right)}d\xi\right\}=-T
\end{aligned}\tag{4.26}$$

where, $V_a^{-1}-$ stands for the limit value from the left point of V_a^{-1}, and $V_a^{-1}+$ stands for the limit value from the right point of V_a^{-1}. Eq. (4.26) can be solved for the two constants C and V_c by applying Cauchy's integral theorem to an infinite closed rectangular path with a simple pole at $\xi = V_a^{-1}$ in upper-half plane (four integration limits are $\xi = 0$, $\xi = \infty$, $\xi = \infty+i\infty$, and $\xi = i\infty$). The purpose of selecting different integration path is to avoid the imaginary part of the integrand in (4.26). By using Jordan's lemma (Brown and Churchill, 1996) and the condition that stresses vanish along $\mathrm{Im}\{\xi\} = 0$, $|\xi| \le C_d^{-1}$, one gets

$$\begin{aligned}
&\mathrm{Re}\left\{\int_{0}^{C_d^{-1}}\frac{R_V(\xi)C}{2\sqrt{\xi^2-C_d^{-2}}\sqrt{V_c^{-2}-\xi^2}\left(V_a^{-2}-\xi^2\right)}d\xi\right\}=0,\mathrm{Re}\left\{\int_{\infty}^{\infty+i\infty}\frac{R_V(\xi)C}{2\sqrt{\xi^2-C_d^{-2}}\sqrt{V_c^{-2}-\xi^2}\left(V_a^{-2}-\xi^2\right)}d\xi\right\}=0,\\
&\mathrm{Re}\left\{\int_{\infty+i\infty}^{i\infty}\frac{R_V(\xi)C}{2\sqrt{\xi^2-C_d^{-2}}\sqrt{V_c^{-2}-\xi^2}\left(V_a^{-2}-\xi^2\right)}d\xi\right\}=0
\end{aligned}\tag{4.27}$$

Noticing the following integral results along small upper-half circle

$$\mathrm{Re}\left\{\int_{V_a^{-1}-}^{V_a^{-1}+}\frac{R_V(\xi)C}{2\sqrt{\xi^2-C_d^{-2}}\sqrt{V_c^{-2}-\xi^2}\left(V_a^{-2}-\xi^2\right)}d\xi\right\}=-\pi\frac{R_V(V_a^{-1})C}{4\sqrt{V_a^{-2}-C_d^{-2}}\sqrt{V_a^{-2}-V_c^{-2}}V_a^{-1}}\tag{4.28}$$

it then follows from Cauchy's integral theorem and Eq. (4.26-4.28) that

$$\int_0^\infty \frac{R_V(i\xi)C}{2\sqrt{\xi^2+C_d^{-2}}\sqrt{V_c^{-2}+\xi^2}\left(V_a^{-2}+\xi^2\right)}d\xi+\pi\frac{R_V(V_a^{-1})C}{4\sqrt{V_a^{-2}-C_d^{-2}}\sqrt{V_a^{-2}-V_c^{-2}}V_a^{-1}}=S_y-T$$
$$\int_0^\infty \frac{R_V(i\xi)C}{2\sqrt{\xi^2+C_d^{-2}}\sqrt{V_c^{-2}+\xi^2}\left(V_a^{-2}+\xi^2\right)}d\xi=-T \tag{4.29}$$

For given V_a, S_y and T, the two conditions (4.29) determine the two constants C and V_c. In particular, it follows from Eq. (4.29) that,

$$C=\frac{4S_y\sqrt{V_a^{-2}-C_d^{-2}}\sqrt{V_a^{-2}-V_c^{-2}}V_a^{-1}}{\pi R(V_a^{-1})} \tag{4.30}$$

From Eq. (4.18) and (4.29), it can be seen that when crack speed V_a is equal to Rayleigh wave speed C_R, $R_V(C_R^{-1}) = 0$ and Eq. (4.29) has no solution. Therefore, the theoretical limit crack speed is C_R. On the other hand, if V_c and V_a and S_y are all given, the remote loading T can be solved numerically from Eq. (4.29). The numerical results can be checked in the following two special cases.

i) For a static crack when both the crack tip speed and cohesive zone tip speed $V_a\to 0$ and $V_c\to 0$, then $V_c^{-1}\to\infty$ and $V_a^{-1}\to\infty$ (but $t\to\infty$ so that the crack length V_at is not zero), it can be shown that $R_V(i\xi)\to 2(C_s^{-2}-C_d^{-2})\xi^2$ when $\xi\to\infty$. Thus from Eq. (4.29), one gets

$$\frac{(C_s^{-2}-C_d^{-2})C}{\sqrt{V_a^{-2}-V_c^{-2}}}\operatorname{arc\,cot}\frac{V_c^{-1}}{\sqrt{V_a^{-2}-V_c^{-2}}}-\frac{\pi(C_s^{-2}-C_d^{-2})C}{2\sqrt{V_a^{-2}-V_c^{-2}}}=S_y-T$$
$$\frac{(C_s^{-2}-C_d^{-2})C}{\sqrt{V_a^{-2}-V_c^{-2}}}\operatorname{arc\,cot}\frac{V_c^{-1}}{\sqrt{V_a^{-2}-V_c^{-2}}}=-T \tag{4.31}$$

Therefore

$$\operatorname{arc\,cot}\frac{V_at}{\sqrt{(V_ct)^2-(V_at)^2}}=\frac{\pi T}{2S_y} \tag{4.32}$$

which is identical to the classical result of a static crack (Dugdale, 1960).

ii) When $V_a > 0$, $S_y = Y$, the relation between the relative cohesive zone length $l_c = (V_c - V_a)/V_c$ and T under different crack speeds are determined by Eq. (4.29). The results are shown in Fig. 4.2, which agree well with the Fig. 3 in (Embley and Sih, 1972) derived by a different approach

based on the 1D yielding condition $S_y = Y$.

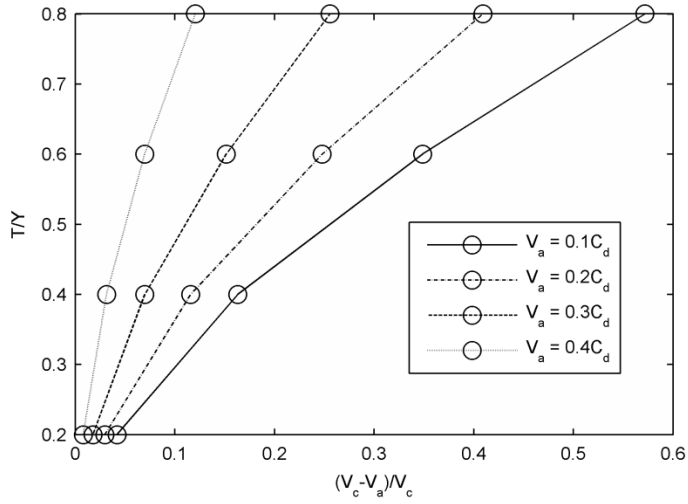

Fig. 4.2 Relation between relative cohesive zone length $l_c = (V_c - V_a)/V_c$ and remote loading T at different crack speed V_a given by the classical Dugdale model with constant yielding stress Y. ($\nu = 0.3$, plane stress)

In this chapter, we consider the 2D von Mises yielding criterion (4.19) without hardening. Thus, from Eq. (4.17), (4.19) and (4.25), similar as Eq. (3.17) in chapter 3, one gets, under plane stress condition,

$$S_y = \frac{2R_a{}^2T - R_aT + \sqrt{(R_aT - 2R_a{}^2T)^2 - 4(R_a{}^2 - R_a + 1)(R_a{}^2T^2 - Y^2)}}{2(R_a{}^2 - R_a + 1)} \tag{4.33}$$

with

$$R_a(V_a, T) = \frac{\sigma_{xx}}{S_y - T} = \frac{\mathrm{Re}\left\{\int_{C_d^{-1}}^{V_c^{-1}} \frac{2(C_s^{-2} - C_d^{-2})(C_s^{-2} - 2\xi^2) - R(\xi)}{2\sqrt{\xi^2 - C_d^{-2}}\sqrt{V_c^{-2} - \xi^2}\left(V_a^{-2} - \xi^2\right)} d\xi\right\}}{\mathrm{Re}\left\{\int_{C_d^{-1}}^{V_c^{-1}} \frac{R(\xi)}{2\sqrt{\xi^2 - C_d^{-2}}\sqrt{V_c^{-2} - \xi^2}\left(V_a^{-2} - \xi^2\right)} d\xi\right\}} \tag{4.34}$$

The values of R_a and S_y under different crack speed are shown in Fig. 4.3-4.4. In Fig. 4.3, the black dot-line is the R_a value near the crack tip at $y' = 0$ predicted by LEFM (Freund, 1990). It can be seen from Fig. 4.3 that R_a increases with increasing crack speed. This confirms that at high crack speed, the normal stress parallel to the crack faces σ_{xx} can be even larger than the normal traction S_y on the cohesive zone and cannot be ignored. This justifies the necessity of including the normal stress σ_{xx} in the yielding condition especially at high crack speed, as studied in this chapter. In addition, R_a increases with remote loading T. If $T << S_y$, the second

equation in (4.29) can be neglected and Eq. (4.29) is reduced to

$$R_a = \frac{2(C_s^{-2} - C_d^{-2})(C_s^{-2} - 2V_a^{2}) - R_V(V_a)}{R_V(V_a)}, \quad T << S_y \tag{4.35}$$

which is identical to the near tip results given by LEFM (Freund, 1990). Thus, from Fig. 4.3 it can be seen that the inertia effect becomes even more important in the cohesive zone model as compared with LEFM.

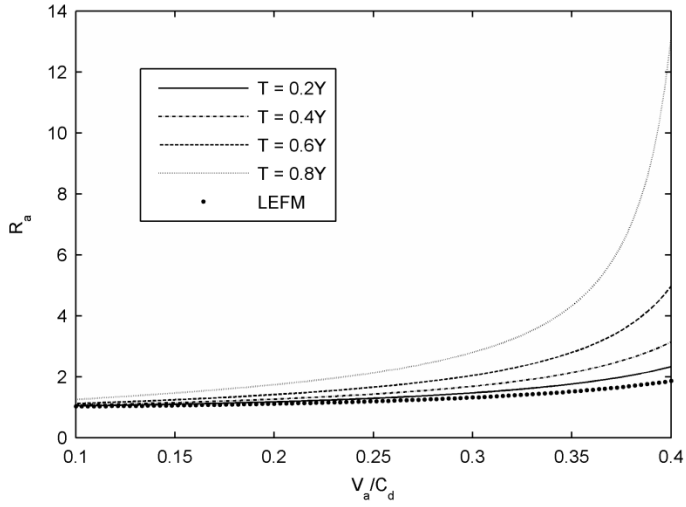

Fig. 4.3 Relation between the ratio R_a and crack speed V_a under different loading T. (v = 0.3, plane stress, C_d is the longitudinal elastic wave speed)

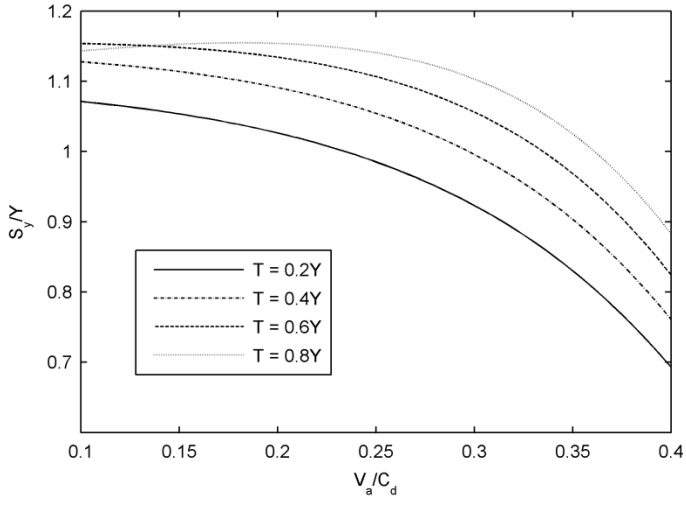

Fig. 4.4 Relation between uniform traction force S_y and crack speed V_a under different loading T. (v = 0.3, plane stress)

From Fig. 4.4 it can be seen that under moderate and low remote loading $T \leq 0.6Y$, with the inertia effect, the traction force S_y on cohesive zone decreases monotonously with crack speed,

but when $T = 0.8Y$ as shown in Fig. 4.4, the traction force attains maximum at around $V_a = 0.2C_d$ and then decreases to about $0.9Y$ at $V = 0.4C_d$. Finally, it should be clarified that in common, the maximum fracture speeds for ductile materials such as metals is around $0.2C_d$. However, the present high-speed model is also applicable for materials experiencing yielding in cohesive zone while propagating, such as small scale yielding in brittle fracture. In what follows, the implications of the present model for the cohesive zone length, crack tip open displacement and energy releases rate are examined in more detail.

4.3.1 Cohesive zone length

Taking Eq. (4.33) into (4.29), the relation between crack speed V_a and relative cohesive zone length $l = (V_c - V_a)/V_c$ under different mode-I loading T can be obtained and shown in Fig. 4.5. From Fig. 4.5, the present model predicts that the cohesive zone length decreases with increasing crack speed, in consistency with the classical Dugdale model (Atkinson, 1968; Embley and Sih, 1972; Wu and Huang, 2013) based on 1D yielding condition $S_y = Y$. However, the cohesive zone length given by the present model decreases with crack speed slowly as compared to the classical Dugdale model, as a result of the inertia effect. The differences between these two models are shown in Fig. 4.6. From Fig. 4.6 it can be seen that the present model predicts a larger cohesive zone length at high crack speed especially under low remote mode-I loading. For example, the relative zone length given by the present model is larger than 2 times the zone length give by classical Dugdale model at $V_a = 0.4C_d$ and $T = 0.2Y$.

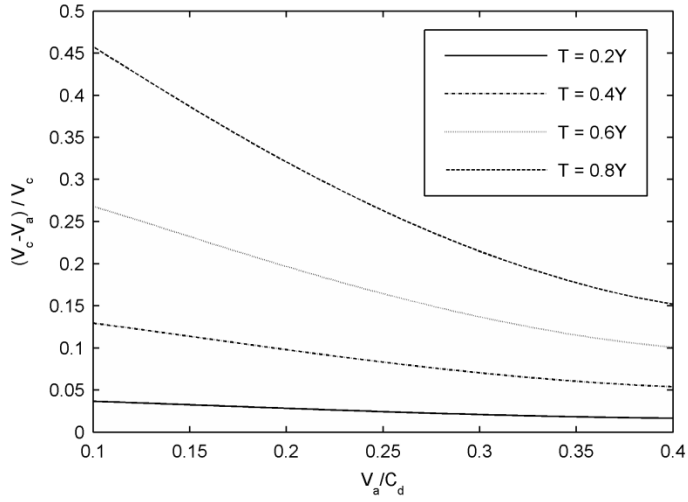

Fig. 4.5 Relation between relative cohesive zone length $l = (V_c - V_a)/V_c$ and crack speed V_a under different remote loading T given by the present model. (v = 0.3, plane stress)

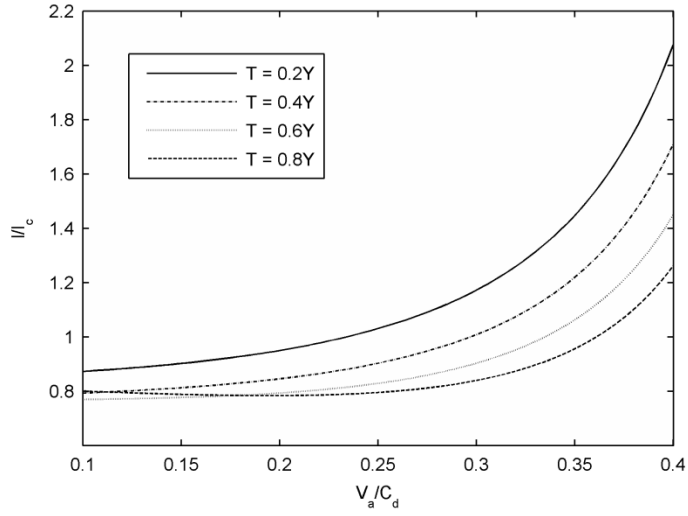

Fig. 4.6 The relative cohesive zone length predicted by the present model (l) and classical Dugdale model (l_c) at different crack speed V_a. (v = 0.3, plane stress)

4.3.2 Crack tip opening displacement (CTOD) and energy release rate

From Eq. (4.1), (4.4-4.7), (4.22), (4.25), for an expanding crack under remote loading T and cohesive force S_y, one gets at $y = 0$, along the upper cohesive zone face

$$\frac{\partial u_y(\xi)}{\partial t} = -\frac{C}{4\mu C_s{}^2 V_a^{-1}\sqrt{V_a^{-2}-V_c^{-2}}}\ln\left(\frac{\xi\sqrt{V_a^{-2}-V_c^{-2}}+V_a^{-1}\sqrt{\xi^2-V_c^{-2}}}{\xi\sqrt{V_a^{-2}-V_c^{-2}}-V_a^{-1}\sqrt{\xi^2-V_c^{-2}}}\right) \tag{4.36}$$

which gives

$$u_y(\xi) = -\frac{Cx'}{4\mu C_s{}^2 V_a^{-1}\sqrt{V_a^{-2}-V_c^{-2}}}\left[\xi \ln\left(\frac{\xi\sqrt{V_a^{-2}-V_c^{-2}}+V_a^{-1}\sqrt{\xi^2-V_c^{-2}}}{\xi\sqrt{V_a^{-2}-V_c^{-2}}-V_a^{-1}\sqrt{\xi^2-V_c^{-2}}}\right)\right.$$
$$\left. - V_a^{-1}\ln\left(\frac{\sqrt{V_a^{-2}-V_c^{-2}}+\sqrt{\xi^2-V_c^{-2}}}{\sqrt{V_a^{-2}-V_c^{-2}}-\sqrt{\xi^2-V_c^{-2}}}\right)\right] \tag{4.37}$$

here the constant term has been ignored. At the crack tip, when $\xi \to V_a^{-1}$, from Eq. (4.37), in view of the symmetry of the displacement, one gets the CTOD δ

$$\delta = \frac{4S_y(1-\beta_2{}^2)\beta_1 x'}{\pi\mu\left[4\beta_1\beta_2-(1+\beta_2{}^2)^2\right]}\ln\left(\frac{V_c}{V_a}\right) \tag{4.38}$$

where, $\beta_1 = (1-V_a{}^2/C_d{}^2)^{1/2}$, $\beta_2 = (1-V_a{}^2/C_s{}^2)^{1/2}$ as shown in chapter 3. Under the same crack length $x' = V_a t$, the relation between CTOD and crack speed given by the present model is shown in Fig. 4.7. From Fig. 4.7 it can be seen that the CTOD given by the present model decreases with crack speed, in consistency with classical Dugdale model (Wu and Huang, 2013). The ratio between CTOD given by the present model δ and the classical Dugdale model δ_c is shown in Fig. 4.8. From Fig. 4.8, it can be seen that at low crack speed, the present model predicts a smaller CTOD as compared with the classical Dugdale model, because the present model predicts a larger traction force on cohesive zone (see Fig. 4.4). However, the ratio between the present model and the classical Dugdale model increases with crack speed and becomes larger than 1.4 at $V_a = 0.4C_d$ and $T = 0.2Y$.

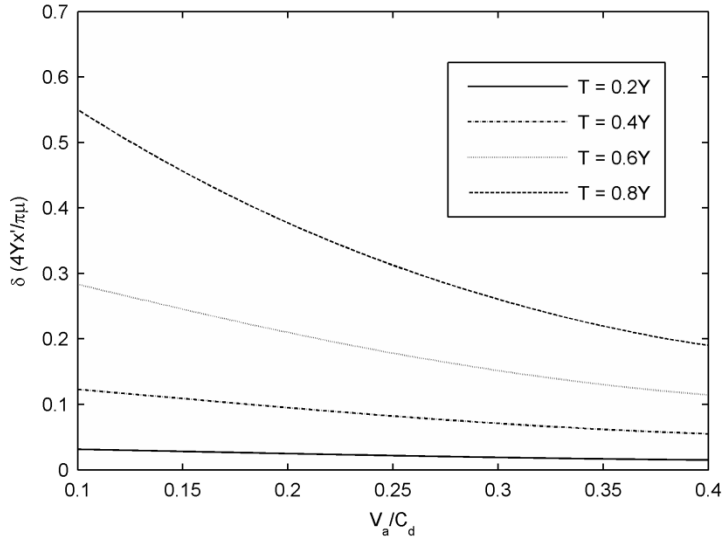

Fig. 4.7 Relation between CTOD δ and crack speed V_a given by the present model. (ν = 0.3, plane stress)

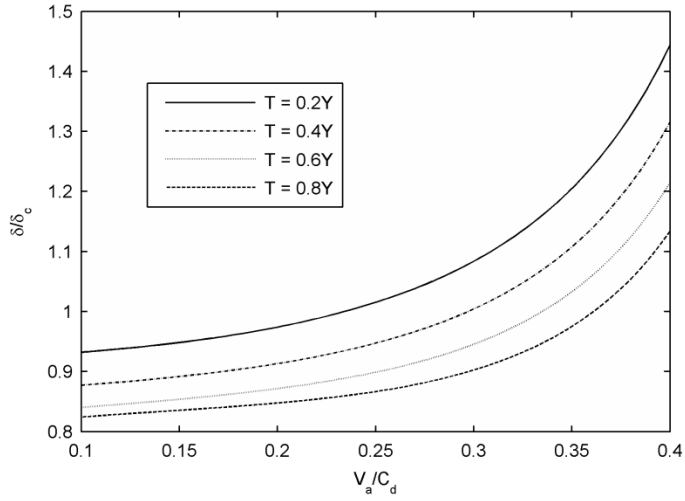

Fig. 4.8 CTOD given by the present model (δ) and the classical Dugdale model (δ_c) at different crack speed V_a. (ν = 0.3, plane stress)

In addition, the energy release rate G is given by (Embley and Sih, 1972)

$$G = \frac{2S_y}{V_a}\int_{V_a t}^{V_c t}\frac{\partial u_y}{\partial t}dx' \tag{4.39}$$

From Eq. (4.36) and (4.39), one gets

$$G = \frac{4S_y{}^2(1-\beta_2{}^2)\beta_1 V_a t}{\pi\mu\left[4\beta_1\beta_2-(1+\beta_2{}^2)^2\right]}\left[\sqrt{\left(\frac{V_c}{V_a}\right)^2-1}\arccos\left(\frac{V_a}{V_c}\right)-\ln\left(\frac{V_c}{V_a}\right)\right] \tag{4.40}$$

Let us consider the energy release rate normalized by the energy release rate G_0 in elastostatic case (Embley and Sih, 1972) with $G_0 = (\kappa+1)\pi V_a t T^2/8\mu$. The normalized energy release rate G/G_0 at different remote loading T is shown in Fig. 4.9 as a function of crack speed. From Fig. 4.9 it can be seen that the normalized energy release rate decreases with crack speed, and its dependence on the remote loading T becomes insignificant at high crack speed, in consistency with the classical Dugdale model (Embley and Sih, 1972; Wu and Huang, 2013). The energy release rate given by the classical Dugdale model (G_c) is compared with the present model (G) in Fig. 4.10. From Fig. 4.10, it can be seen that differences between these two models are relatively small, especially when crack is under low remote loadings. The ratio between G/G_c increases with crack speed, which means that the inertia effect with high crack speed in cohesive zone has

the potential to increase the energy release rate for a high-speed expanding crack.

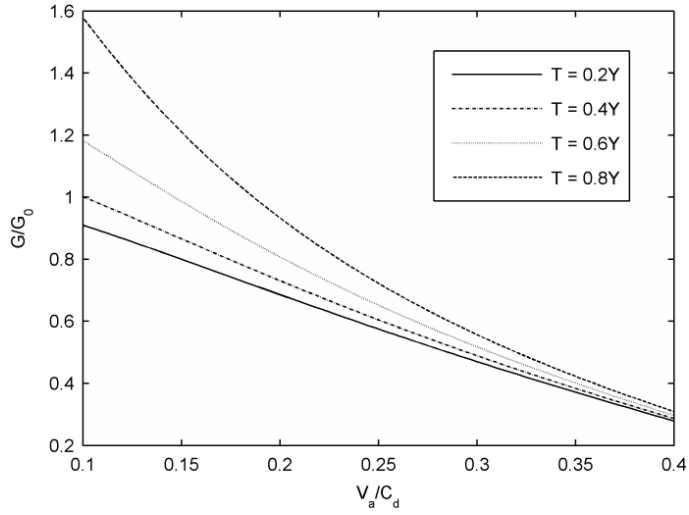

Fig. 4.9 The normalized energy release rate G/G_0 at different crack speed V_a given by the present model. (v = 0.3, plane stress)

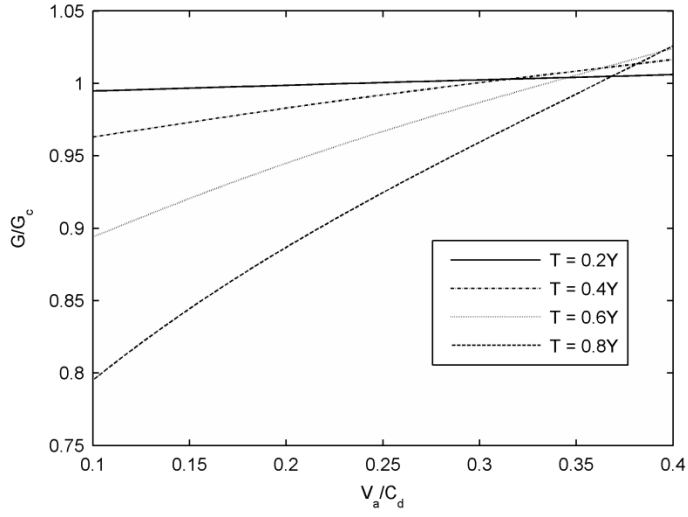

Fig. 4.10 Energy release rate given by the present model (G) and classical Dugdale model (G_c) at different crack speed V_a. (v = 0.3, plane stress)

4.4 Strain hardening with non-uniform traction distribution in the cohesive zone

Strain hardening (or softening) of materials are often involved in cohesive zone thus the traction usually are not constant along the zone (Siegmund and Brocks, 2000). Therefore, in the present paper, non-uniform traction distribution is employed to describe the strain hardening effect in the cohesive zone. More specifically, the traction force in cohesive zone is assumed to be a symmetric function $S_y(t/x')$ of variable t/x'. For elastic mode-I crack without a cohesive zone, a distributed pressure on the crack faces described by a polynomial of t/x' has been studied in some previous works (Georgiadis, 1991) by an integral equation approach. However, to the best of the present author's knowledge, no attempts have been made to an expanding crack with variable traction force in cohesive zone. In this section, the non-uniform traction is solved numerically by replacing the continuous traction distribution by a group of constant traction force along cohesive zone (Theocaris and Gdoutos, 1974). This method was employed in reference (Theocaris and Gdoutos, 1974) to solve a static crack problem and now is extended to dynamic problem in this thesis. Therefore, the solution of $G_{xt}'(\xi)$ can be expressed by the superposition of n solutions of expanding cracks each of which is under a uniform traction force in a cohesive zone ($V_c^{-1} < \xi < \xi_j$, $j = 1,2\ldots n$, see Eq. (4.42)) and remote mode-I loading. Thus, compared with Eq. (4.25), one gets

$$G_{xt}'(\xi) = \sum_{j=1}^{n} \frac{\xi^2 Q_j(\xi)}{\left(V_c^{-2} - \xi^2\right)^{3/2} \left(\xi_j^{\,2} - \xi^2\right)} \tag{4.41}$$

with

$$\xi_j = V_a^{-1} - \left(V_a^{-1} - V_c^{-1}\right)(j-1)/n \tag{4.42}$$

where, $Q_j(\xi)$ is a symmetric polynomial with real constant to be determined by boundary conditions. In particular, considering the cancelation of singularity at the cohesive zone tip and finite particle velocity at infinity in ζ plane, Eq. (4.41) can be expressed by

$$G'_{xt}(\xi)=\sum_{j=1}^{n}\frac{D_j}{\sqrt{V_c^{-2}-\xi^2}\left(\xi_j^{\,2}-\xi^2\right)} \tag{4.43}$$

where, D_j is a real constant to be determined by boundary conditions. Thus, from the first and second boundary condition in (4.3) and Eq. (4.29), one gets

$$\begin{aligned}
&\sum_{j=1}^{n}\int_0^{\infty}\frac{R_V(i\xi)D_j}{2\sqrt{\xi^2+C_d^{-2}}\sqrt{V_c^{-2}+\xi^2}\left(\xi_j^{\,2}+\xi^2\right)}d\xi+\sum_{j=1}^{k}\pi\frac{R_V(\xi_j)D_j}{4\sqrt{\xi_j^{\,2}-C_d^{-2}}\sqrt{\xi_j^{\,2}-V_c^{-2}}\,\xi_j}=S_y(\xi_k)-T\\
&\sum_{j=1}^{n}\int_0^{\infty}\frac{R_V(i\xi)D_j}{2\sqrt{\xi^2+C_d^{-2}}\sqrt{V_c^{-2}+\xi^2}\left(\xi_j^{\,2}+\xi^2\right)}d\xi=-T
\end{aligned} \tag{4.44}$$

with k = 1, 2, ...n. Eq. (4.44) is a set of n+1 linear equations with n+1 unknowns D_j and T, so can be solved numerically. In particular, when $V_a\rightarrow 0$, similar as Eq. (4.31), from Eq. (4.32), one gets

$$\begin{aligned}
&\sum_{j=1}^{n}\frac{(C_s^{-2}-C_d^{-2})D_j}{\sqrt{\xi_j^{\,2}-V_c^{-2}}}\operatorname{arc\,cot}\frac{V_c^{-1}}{\sqrt{\xi_j^{\,2}-V_c^{-2}}}-\sum_{j=1}^{k}\frac{\pi(C_s^{-2}-C_d^{-2})D_j}{2\sqrt{\xi_j^{\,2}-V_c^{-2}}}=S_y(\xi_k)-T\\
&\sum_{j=1}^{n}\frac{(C_s^{-2}-C_d^{-2})D_j}{\sqrt{\xi_j^{\,2}-V_c^{-2}}}\operatorname{arc\,cot}\frac{V_c^{-1}}{\sqrt{\xi_j^{\,2}-V_c^{-2}}}=-T
\end{aligned} \tag{4.45}$$

which enable us to compare our numerical results with existing analytical results in static case. For example, we consider the case that $S_y(t/x') = q_1(t/x')^{-2}$, where q_1 is a real constant. This is equivalent to the problem of a static crack with crack length $2V_a$ and cohesive zone length (V_c-V_a) in the $(x'/t, y)$ plane under traction force $S_y(x'/t) = q_1(x'/t)^2$ in cohesive zone and remote tensile loading T, which has an analytic solution given in reference (Harrop, 1978) derived by weight function method

$$T=\frac{q_1}{\pi}\left(V_c^{\,2}\arccos\frac{V_a}{V_c}+V_a\sqrt{V_c^{\,2}-V_a^{\,2}}\right) \tag{4.46}$$

Theoretically, the accuracy of numerical results increases with increasing n. Thus, our numerical results from Eq. (4.45) with n = 1000 is compared to the analytic results (Harrop, 1978) and errors are shown in table 4.1. From table 4.1, it can be seen that good accuracy can be achieved by the present numerical method when n is sufficiently large. Therefore, Eq. (4.43) provides a

simple and accurate way to consider the non-uniform traction force in cohesive zone for a high-speed expanding crack.

Table 4.1 Validation of numerical results of an expanding crack under non-uniform traction force $S_y(t/x') = q_1(t/x')^{-2}$ in cohesive zone.

	V_a=0.05C_d, V_c=0.1C_d	V_a=0.08C_d, V_c=0.1C_d	V_a=0.02C_d, V_c=0.1C_d
numerical	$0.004707q_1C_d^2$	$0.003575q_1C_d^2$	$0.004965q_1C_d^2$
analytic	$0.004712q_1\ C_d{}^2$	$0.003576q_1C_d^2$	$0.004983q_1C_d^2$
relative error	0.11%	0.03%	0.36%

From Eq. (4.17) and (4.43), the distribution of normal stress σ_{xx} in cohesive zone can be derived as

$$\sigma_{xx}(\xi_k) = M_1 f(\xi_k) - M_2 T \tag{4.47}$$

with

$$M_1(\xi_k) = \frac{\sum_{j=1}^{k} \frac{\left[2(C_s^{-2} - C_d^{-2})(C_s^{-2} - 2\xi_j^{\ 2}) - R_V(\xi_j)\right] D_j}{4\sqrt{\xi_j^{\ 2} - C_d^{-2}}\sqrt{\xi_j^{\ 2} - V_c^{-2}}\,\xi_j}}{\sum_{j=1}^{k} \frac{R_V(\xi_j) D_j}{4\sqrt{\xi_j^{\ 2} - C_d^{-2}}\sqrt{\xi_j^{\ 2} - V_c^{-2}}\,\xi_j}},\quad M_2 = \frac{\sum_{j=1}^{n} D_j \int_0^{\infty} \frac{2(C_s^{-2} - C_d^{-2})(C_s^{-2} + 2\xi^2) - R_V(i\xi)}{2\sqrt{\xi^2 + C_d^{-2}}\sqrt{V_c^{-2} + \xi^2}\left(\xi_j^{\ 2} + \xi^2\right)} d\xi}{\sum_{j=1}^{n} D_j \int_0^{\infty} \frac{R_V(i\xi)}{2\sqrt{\xi^2 + C_d^{-2}}\sqrt{V_c^{-2} + \xi^2}\left(\xi_j^{\ 2} + \xi^2\right)} d\xi} \tag{4.48}$$

Therefore, from Eq. (4.47) and (4.48) it can be seen that, different from the Yoffe-type moving crack model of constant crack length which predicts that the ratio R_a between σ_{xx} and σ_{yy} is a constant in the cohesive zone and independent of the form of traction distribution (Kanninen, 1968), the present self-similar expanding crack model predicts that R_a varies along cohesive zone and depends on the specific form of traction distribution. For example, variations of R_a along cohesive zone at different crack speed V_a and cohesive zone tip speed V_c under non-uniform traction $S_y(t/x') = q_1(t/x')^{-2}$ is shown in Fig. 4.11. From Fig. 4.11 it can be seen that R_a varies along cohesive zone under non-uniform traction $S_y(t/x') = q_1(t/x')^{-2}$ and tends to a constant at low crack speed when $V_a = 0.08C_d$.

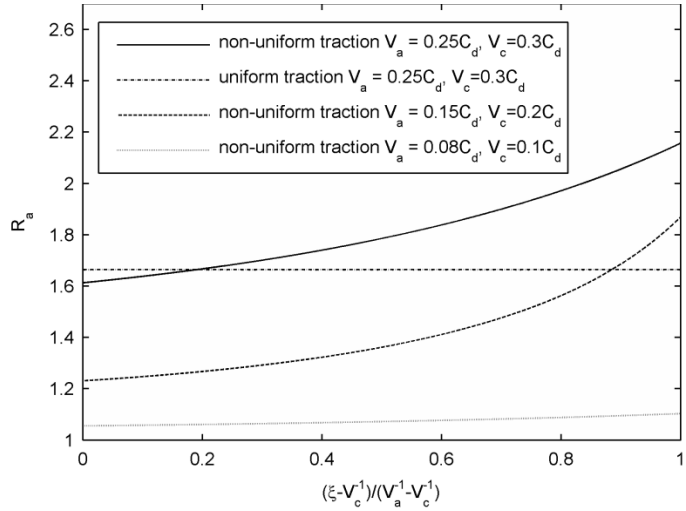

Fig. 4.11 Variations of R_a along cohesive zone at different crack speed V_a and cohesive zone tip speed V_c under non-uniform traction force $S_y(t/x') = q_1(t/x')^{-2}$.

Finally, the displacement u_y in cohesive zone and energy release rate G under non-uniform traction can be obtained from Eq. (4.36-4.40), (4.43)

$$u_y(\xi) = -\sum_{j=1}^{n} \frac{D_j x'}{4\mu C_s^{\,2}\xi_j\sqrt{\xi_j^{\,2}-V_c^{-2}}}\left[\xi \ln\left(\frac{\xi\sqrt{\xi_j^{\,2}-V_c^{-2}}+\xi_j\sqrt{\xi^2-V_c^{-2}}}{\xi\sqrt{\xi_j^{\,2}-V_c^{-2}}-\xi_j\sqrt{\xi^2-V_c^{-2}}}\right) - \xi_j \ln\left(\frac{\sqrt{\xi_j^{\,2}-V_c^{-2}}+\sqrt{\xi^2-V_c^{-2}}}{\sqrt{\xi_j^{\,2}-V_c^{-2}}-\sqrt{\xi^2-V_c^{-2}}}\right)\right] \tag{4.49}$$

$$G = -\sum_{k=1}^{n} f(\xi_k)\left\{\sum_{j=1}^{n} \frac{D_j}{2\mu C_s^{\,2} V_a \xi_j\sqrt{\xi_j^{\,2}-V_c^{-2}}}\left[x' \ln\left(\frac{t\sqrt{\xi_j^{\,2}-V_c^{-2}}+\xi_j\sqrt{t^2-x'^2V_c^{-2}}}{t\sqrt{\xi_j^{\,2}-V_c^{-2}}-\xi_j\sqrt{t^2-x'^2V_c^{-2}}}\right)\right.\right.$$
$$\left.\left. +2\xi_j^{-1}t\sqrt{\frac{\xi_j^{\,2}}{V_c^{-2}}-1}\arctan\frac{x'}{\sqrt{V_c^{\,2}t^2-x'^2}}+\xi_j^{-1}t\ln\left(\frac{tx'\sqrt{\xi_j^{\,2}-V_c^{-2}}-t\sqrt{t^2-x'^2V_c^{-2}}}{tx'\sqrt{\xi_j^{\,2}-V_c^{-2}}+t\sqrt{t^2-x'^2V_c^{-2}}}\right)\right]\right\}\Bigg|_{x'=t/\xi_{k+1}}^{x'=t/\xi_k} \tag{4.50}$$

4.5 Comparison between the self-similar expanding crack and steady-state moving crack

From Fig. 3.2 and 4.4 it can be seen that based on von Mises criterion, under low and moderate remote loading, the modified cohesive zone model predicts a decreasing traction force with increasing crack speed for both steady-state moving crack and self-similar expanding crack. Thus, in this section, the traction force ahead of a self-similar expanding crack tip is compared with that head of a moving crack tip, as shown in Fig. 4.12. It can be seen from Fig. 4.12 that the effect of crack speed on traction force is more significant for a self-similar expanding crack compared with a steady-state moving crack of constant length. Actually, at low crack speed when $V_a < 0.15C_d$, the different between these two types of moving cracks is small. At higher crack speed, the traction force ahead of a self-similar expanding crack tip decreases more severely with increasing crack speed. However, the predicted traction decreases with increasing crack speed for both types of moving cracks studied in chapter 3 and 4. This indicates although Yoffe-type model (studied in chapter 3) is an over-simplified mathematical model for moving cracks, the stress state in cohesive zone given by the Yoffe-type model is similar to that given by a self-similar expanding crack model (studied in this chapter). Thus the Yoffe-type model is still of physical interest for moving crack problems.

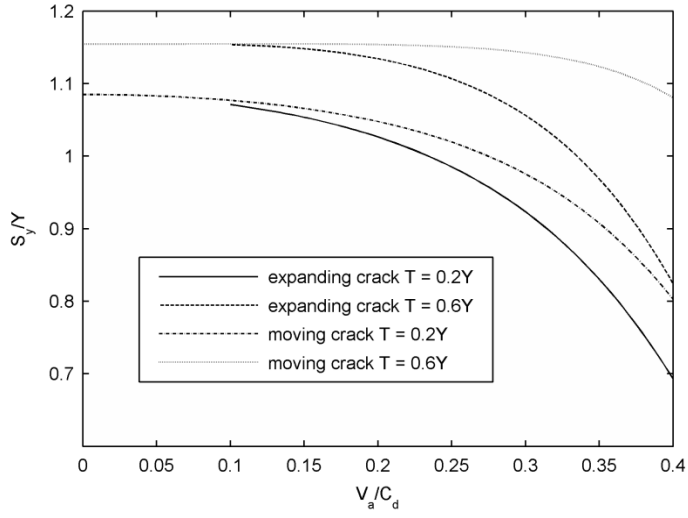

Fig. 4.12 Relation between uniform traction force S_y and crack speed V_a under different loading T for

self-similar expanding and Yoffe-type moving cracks. ($\nu = 0.3$, plane stress)

4.6 Conclusions

Self-similar crack propagation is studied with a modified cohesive zone model, in which the effects of the normal stress parallel to the crack faces σ_{xx} and strain hardening are included. It is shown that the normal stress parallel to the crack faces, which has been ignored in all previous related models, is even larger than the normal traction on the cohesive zone at high crack speed, which justifies the necessity of including it in the yielding condition on the cohesive zone. Based on von Mises criterion without hardening, it is shown that different from classical Dugdale model for an expanding crack, the traction force on cohesive zone predicted by the present model decreases with increasing crack speed under moderate or low mode-I remote loading, but attains maximum when crack speed is around 0.2 of longitudinal elastic wave speed under high mode-I remote loading. By considering the inertia effect, the present model predicts a larger cohesive zone length and CTOD at high crack speed as compared to the classical Dugdale model, while the difference between the energy release rate given by the present model and classical Dugdale model is relatively small. These results indicate that the inertia effect cannot be ignored at high crack speed and a speed-dependent traction force is required in analytic and numerical analysis in dynamic fracture. Finally, strain hardening effect is studied with a non-uniform traction distribution in cohesive zone solved numerically by replacing the continuous traction distribution by a group of step functions. The accuracy of this method is verified by good agreement with known analytic results in static case.

Chapter 5: Inertia effect of cohesive zone on a high-speed moving crack

5.1 Introduction

The cohesive zone models, first proposed by Barenblatt (Barenblatt, 1959) and Dugdale (Dugdale, 1960) for a static crack, have successfully been employed in analytical and numerical studies of crack propagation in nonlinear or ductile materials (Costanzo and Walton, 2002; Kubair et al., 2002; Scheider, 2009; Tvergaard and Hutchinson, 1994; Xu and Needleman, 1994; Zhang et al., 2003). In all of these studies, the cohesive zone is simplified as a line segment without a volume and mass. The constitutive law in cohesive zone is modeled by linear or nonlinear springs distributed along the cohesive zone (Volokh, 2004; Williams and Hadavinia, 2002) and the surrounding bulk materials are often assumed to be linearly elastic (Costanzo and Walton, 2002; Kubair et al., 2002; Zhang et al., 2003). Apparently, all of the above-mentioned existing cohesive zone models have completely ignored the mass and inertia of the cohesive zone. Since the cohesive zone actually represents a region near the crack tip in which plastic or nonlinear deformation dominates (Livne et al., 2010; Rosakis and Freund, 1982), the mass of this region, which has been ignored in the existing cohesive zone models (Costanzo and Walton, 2002; Kubair et al., 2002; Scheider, 2009; Tvergaard and Hutchinson, 1994; Volokh, 2004; Williams and Hadavinia, 2002; Xu and Needleman, 1994; Zhang et al., 2003), could have a significant effect on dynamic fracture of a high-speed moving crack. Therefore, it is of great interest to study the inertia effect of cohesive zone on a moving crack in a ductile or nonlinear material. To the best of my knowledge, this issue has not been well addressed in the literature.

This chapter aims to study the inertia effect of the cohesive zone on a mode-I Yoffe-type steady-state moving crack of constant length. The cohesive zone of mass and inertia is modeled as distributed springs with concentrated mass attached at the two ends of each spring, as shown in Fig. 5.1. This new cohesive zone model for a steady-state moving crack of Yoffe-type is described in section 5.2. Determination of the mass distribution function in cohesive zone is

discussed in section 5.3. In particular, the mass distribution along cohesive zone is defined by a simple function which vanishes at the two ends of the cohesive zone and ensures that traction remains finite at both crack tips and cohesive zone tips. Iteration method and an alternative numerical method are described and tested in section 5.4. Traction distribution surrounding the cohesive zone and speed-dependent fracture energy are then solved numerically and discussed in section 5.5. Finally, main conclusions are summarized in section 5.6.

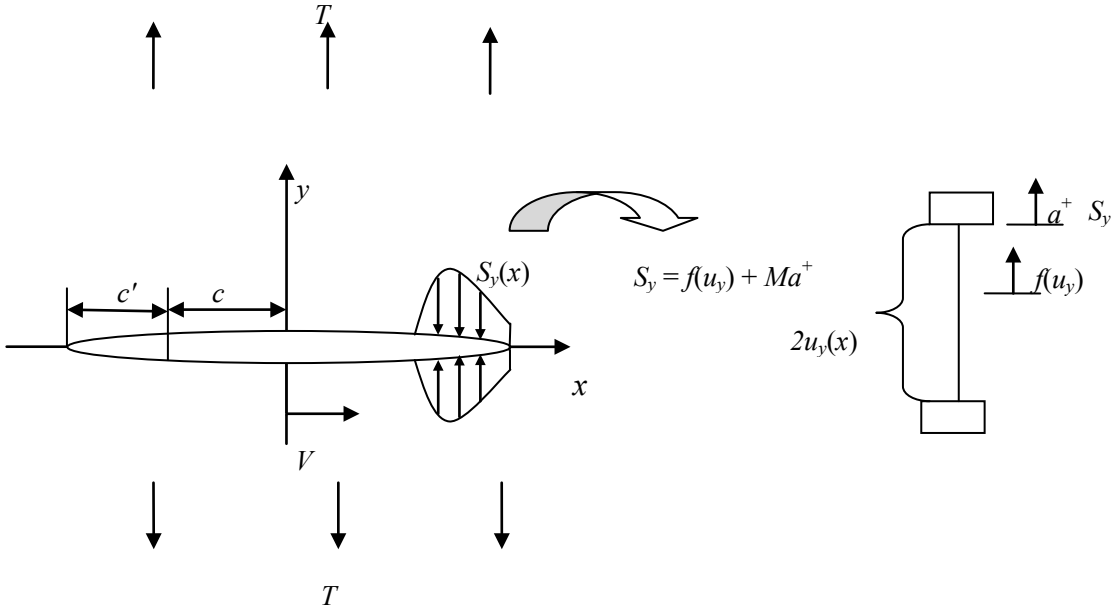

Fig. 5.1 A crack of constant length 2c moving along the x-axis at speed V in the moving coordinate system (x, y) with a cohesive zone characterized by distributed mass-springs, where T is the remote mode-I loading, c' is the cohesive zone length, S_y is the outer traction surrounding the cohesive zone, M is the distributed mass attached on the two ends of each spring, u_y is the half of cohesive zone separation and a^+ is the y-directional acceleration of the upper end of the spring.

5.2 A mass-spring cohesive zone model

Let us consider a Yoffe-type steady-state moving crack. The crack of constant length 2c in an infinite elastic sheet or plane, subjected to the mode-I remote tensile loading T, is moving at a

constant speed V along the x-axis in a moving coordinates system (x, y). The cohesive zone is defined as a line segment and have a length c' ahead of each crack tip (see the left figure in Fig. 5.1). However, different from the traditional cohesive zone models in which the mass of the cohesive zone is ignored, in the present paper, the cohesive zone is modeled by a mass-spring system in which a distributed mass $M(x)$ (per unit length along the cohesive zone, whose specific form is to be determined below) is attached to the two ends of the distributed springs in the cohesive zone (see the right figure in Fig. 1). Thus, the outer traction S_y surrounding the cohesive zone is given by

$$S_y(x) = f(u_y) + M(x)a^+(x), \ c \le |x| \le c + c' \tag{5.1}$$

where, a^+ is y-directional acceleration of the upper cohesive zone face (at the upper end of the spring), u_y is the half of cohesive zone separation, and $f(u_y)$ is the inner traction inside the cohesive zone which defines the T-S law in the cohesive zone (Volokh, 2004; Williams and Hadavinia, 2002). In the present paper, we consider the T-S law inside the cohesive zone can be described by a bilinear model with 2 adjustable parameter $S_{\max}$ and u_0 (see Fig. 5.2) as follows

$$f(u_y) = \begin{cases} (S_{\max} - S_0)u_y(x)/u_0 + S_0 & u_y(x) \le u_0 \\ S_{\max}\left[u_y(c) - u_y(x)\right]/\left[u_y(c) - u_0\right] & u_y(x) \ge u_0 \end{cases} \tag{5.2}$$

where, S_0 is the initial yielding traction at the end of cohesive zone which is related with crack speed (see Eq. (3.35) in chapter 3 with $S_0 = S$), and $S_{\max}$ is the maximum traction in cohesive zone, u_0 is the half of cohesive zone separation at the location of maximum traction, and $u_y(c)$ is the half of cohesive zone separation at the crack tip. In the present study, the value of $S_{\max}/S_0$ and $u_0/u_y(c)$ are assumed independent of crack speed. When $u_0 = 0$, from the second equation in (5.2), the traction-separation law in cohesive zone reduces to a linear strain softening model (Kubair et al., 2002): $S_y(x) = S_{\max}[1 - u_y(x)/u_y(c)]$.

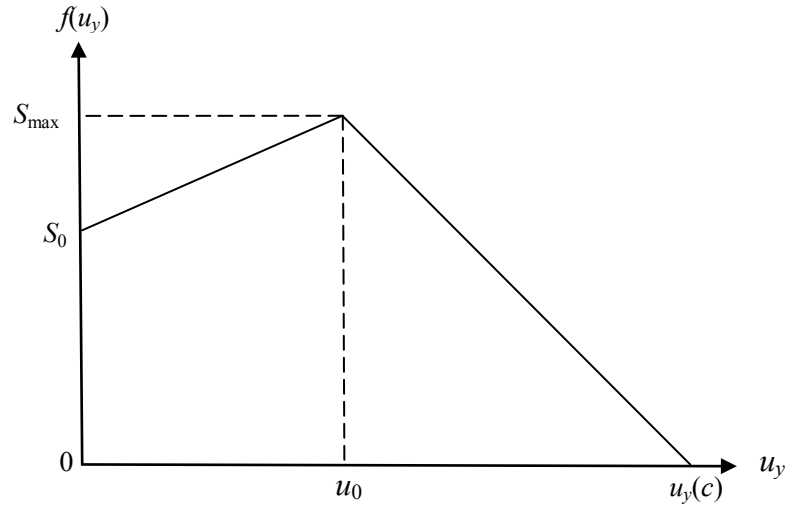

Fig. 5.2 A bilinear T-S law $f(u_y)$ employed in the present paper, where S_0 is the initial yielding traction at the end of the cohesive zone, S_{max} is the maximum traction in cohesive zone, and u_0 is the half of cohesive zone separation at the location of maximum traction.

To solve Eq. (5.1), one needs a relation between the outer traction $S_y(x)$ and the cohesive zone separation $2u_y(x)$. For this end, we consider that the traction $S_y(x)$, surrounding the cohesive zone, can be given in the form of symmetric polynomial $P(x)$ with $n/2+1$ real coefficients

$$S_y(x) = P(x) = A_n x^n + A_{n-2} x^{n-2} + \cdots + A_2 x^2 + A_0 \tag{5.3}$$

where, n is an even integer and A_0, A_2, ..., A_n are real constants and will be determined by Eq. (5.1). From Eq. (3.32) in chapter 3, the half of cohesive zone separation can be given by

$$u_y(x) = \int \frac{A(V)}{\pi\mu}\left[-P(x)\ln\frac{x\sqrt{(c+c')^2-c^2}+c\sqrt{(c+c')^2-x^2}}{x\sqrt{(c+c')^2-c^2}-c\sqrt{(c+c')^2-x^2}} + \frac{Q(x)}{\sqrt{(c+c')^2-x^2}} - \frac{\pi T x}{\sqrt{(c+c')^2-x^2}}\right] \mathrm{d}x \tag{5.4}$$

where, $A(V)$ is a speed dependent function shown in Eq. (3.33). In addition, $Q(x)$ in Eq. (5.4) is a polynomial of finite degree

$$Q(x) = B_n x^{n+1} + B_{n-2} x^{n-1} + \cdots + B_2 x^3 + B_0 x \tag{5.5}$$

where, B_0, B_2, ..., B_n are some real constants determined by the remote loading condition at the infinity, which depend on the traction $P(x)$ (see e.g. Appendix B). Actually, from the asymptotic

stress field at infinity when $x\to\infty$, one gets $n/2+1$ linear relations between A_0, A_2, ..., A_n and B_0, B_2, ..., B_n (see Eq. (3.27) and (3.28)).

$$P(x)-\frac{P(x)}{\pi}\left\{2\arctan\frac{c}{\sqrt{(c+c')^2-c^2}}+\sum_{i=1}^{n/2}\frac{g_1^{(i)}(0)}{i!}\left[\frac{(c+c')^2}{x^2}\right]^i\right\}-\frac{Q(x)}{\pi x}\left\{1+\sum_{i=1}^{n/2}\frac{g_2^{(i)}(0)}{i!}\left[\frac{(c+c')^2}{x^2}\right]^i\right\}=0 \tag{5.6}$$

where, $g_1^{(i)}(0)$ is the ith derivative of $g_1(x)$ at the point 0, $g_2^{(i)}(0)$ is the ith derivative of $g_2(x)$ at the point 0, with

$$g_1(x)=2\arctan\frac{c\sqrt{1-x}}{\sqrt{(c+c')^2-c^2}},\quad g_2(x)=\frac{1}{\sqrt{1-x}} \tag{5.7}$$

In addition, the y-directional acceleration of upper cohesive zone face can be determined by Eq. (5.4) and steady-state condition as follows

$$\begin{aligned}a(x)^+ &= V^2\frac{\partial^2 u_y}{\partial x^2}\\ &=\frac{V^2A(V)}{\pi\mu}\left\{-P'(x)\ln\frac{x\sqrt{(c+c')^2-c^2}+c\sqrt{(c+c')^2-x^2}}{x\sqrt{(c+c')^2-c^2}-c\sqrt{(c+c')^2-x^2}}+\frac{Q'(x)}{\sqrt{(c+c')^2-x^2}}-\frac{\pi T}{\sqrt{(c+c')^2-x^2}}\right.\\ &\left.-P(x)\frac{2c\sqrt{(c+c')^2-c^2}}{(c^2-x^2)\sqrt{(c+c')^2-x^2}}+\frac{Q(x)x}{\left[(c+c')^2-x^2\right]^{3/2}}-\frac{\pi Tx^2}{\left[(c+c')^2-x^2\right]^{3/2}}\right\}\end{aligned} \tag{5.8}$$

For given remote loading T, the length of cohesive zone can be determined by the stress singularity cancelation condition at the cohesive zone tip: $Q(x)=\pi Tx$ at the point $x=c+c'$. Alternatively, for a given length of cohesive zone, the remote loading T can be determined by the above singularity cancelation condition at the cohesive zone tip $Q(c+c')=\pi T(c+c')$. Finally, similar as Eq. (3.34), the fracture energy can be calculated by

$$G=-2\int_c^{c+c'}\frac{A(V)P(x)}{\pi\mu}\left[-P(x)\ln\frac{x\sqrt{(c+c')^2-c^2}+c\sqrt{(c+c')^2-x^2}}{x\sqrt{(c+c')^2-c^2}-c\sqrt{(c+c')^2-x^2}}+\frac{Q(x)}{\sqrt{(c+c')^2-x^2}}-\frac{\pi Tx}{\sqrt{(c+c')^2-x^2}}\right]\mathrm{d}x \tag{5.9}$$

5.3 The determination of mass distribution of cohesive zone

In the present study, we assume that the mass distribution $M(x)$ of cohesive zone is a function of x, determined by the thickness of cohesive zone at point x. From Eq. (5.8), it is seen that the acceleration has a logarithm singularity at crack tips and an inverse square-root singularity at cohesive zone tips. Thus, it follows from Eq. (5.1) that, to ensure a finite traction at both the crack tip and the cohesive zone tips, the mass $M(x)$ must vanish at both crack tips and cohesive zone tips. Here we assume that $M(x)$ is of a simple elliptical form

$$M(x) = \frac{\rho b\sqrt{(c+c')-x}\sqrt{x-c}}{c'},\ c \le x \le c+c' \tag{5.10}$$

where, ρ is the mass density of surrounding bulk material (per unit area), b is a positive constant of a dimension of length and determined by the maximum thickness of cohesive zone. Thus, the mass distribution $M(x)$ given by Eq. (5.10) is consistent with a reasonable assumption that the thickness of the cohesive zone vanishes at the ends of cohesive zone. In addition, consistent with the strip yielding assumption, the maximum thickness b cannot be much larger than the length c' of the cohesive zone. Thus, in the present paper, we assume that $b \le 2c'$.

5.4 Numerical scheme

It can be seen from Eq. (5.1) and (5.3) that the outer traction distribution function $P(x)$ surrounding the cohesive zone contains $n/2+1$ unknown coefficients (A_0, A_2, ..., A_n). Thus, $n/2+1$ collocation points are required to solve Eq. (5.1) based on collocation method (Iserles, 2009; Zhang et al., 2003). In this section, two different numerical approaches are presented

5.4.1 Successive iteration method

In successive iteration method, it is assumed that the Eq. (5.1) holds at $n/2+1$ collocation

points $x = \{x_1, x_2, \ldots, x_{n/2+1}\}$ in the cohesive zone. Combined with Eq. (5.2), (5.4), (5.7) and (5.8), Eq. (5.1) can be represented by a system of $n/2+1$ nonlinear equations with the $n/2+1$ unknowns A_0, A_2, ..., A_n. Given an initial assumed traction $P_{old}(x)$, the displacement and acceleration of cohesive zone faces can be calculated by Eq. (5.4) and (5.10). Then a new traction $P_{new}(x)$ can be obtained from the right hand side of Eq. (5.1), which is generally different than the assumed $P_{old}(x)$. The error is $\|P_{new}(x)-P_{old}(x)\|$. The iteration procedure continues with the new traction $P_{new}(x)$ until the relative error $\|P_{new}(x)-P_{old}(x)\|/\|P_{old}(x)\|$ is smaller than a prescribed tolerance (for example, in the present study, we take the tolerance as 10^{-4}).

5.4.2 An alternative numerical method

In the previous related researches, solving nonlinear equations seems inevitable for traditional spring cohesive zone models (Costanzo and Walton, 2002; Kubair et al., 2002; Zhang et al., 2003). However, the convergence of the solution of nonlinear equations is difficult and strongly depends on initial condition (Edwards and McRae, 1993; Zhang et al., 2003). Therefore, in the present paper, a new linear method is presented for the simple mass-spring cohesive zone model which is defined by a bilinear T-S law. First, let the displacement at crack tip $u_y(c) = \delta/2$ (where δ is the crack tip opening displacement), and the Eq. (5.1) holds at the other $n/2$ collocation points $x = \{x_2, x_3, \ldots, x_{n/2}\}$ in cohesive zone. Combined with the remote loading condition (5.6), a system of $n+2$ linear equations can be constructed and solved for the $n+2$ unknown coefficients $A_0, A_2, \ldots, A_n$ and $B_0, B_2, \ldots, B_n$. Finally, the value of δ can be determined by the condition that $P(c) = 0$.

5.5 Results and discussion

Numerical calculation of Eq. (5.1) was carried out using the two numerical methods described in section 5.4. In the present paper, the inertia effect of cohesive zone on dynamic fracture energy will be studied by examining the role of key thickness parameter b. In Eq. (5.10), $b = c'$ is assumed in section 5.5.1-5.5.3 (see Fig. 5.3-5.8) while variable value of b is examined

in section 5.5.4 (see Fig. 5.9a and Fig. 5.9b). Poisson's ratio ν = 0.3 and coefficients number n = 10 are used in all calculations, and the tolerance is set to be 10^{-4}. Numerical results at different crack speed are discussed in the following sections.

5.5.1. Comparison between the two numerical methods

The traction distribution $S_y(x)$ surrounding the cohesive zone at different crack speed is calculated by the above two methods in the case that $c' = 0.5c$. The results are shown in Fig. 5.3. From Fig. 5.3, it is seen that these two methods give almost identical results for different T-S law parameters at low crack speeds, which confirms the accuracy of these two numerical methods. However, the iteration method fails to converge at higher crack speeds ($V > 0.35C_s$ when $u_0 = 0$, and $V > 0$ when $u_0 > 0$, $S_{max} = 1.2S_0$) while a convergent solution can be obtained by the alternative numerical method proposed in section 5.4.2. Furthermore, our calculations show that other nonlinear iteration technique such as Newton-Raphson method (Kubair et al., 2002) also fails to converge at higher crack speed. Thus, for the present problem, the numerical method proposed in section 5.4.2 is more robust than widely used nonlinear techniques (Costanzo and Walton, 2002; Kubair et al., 2002; Zhang et al., 2003) and can be applied to the present problem even at high crack speed.

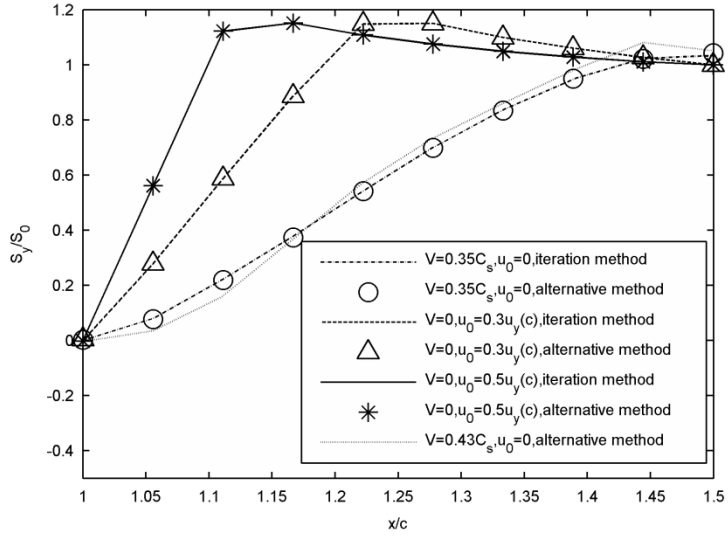

Fig. 5.3 Traction distributions $S_y(x)$ surrounding cohesive zone obtained by two different numerical methods at different crack speed V, when the cohesive zone thickness parameter $b = c'$, and the relative length of cohesive zone is given by $c' = 0.5c$. $S_{max} = 1.2S_0$ is assumed for $u_0 > 0$, and C_s is the transverse elastic wave speed.

5.5.2. Oscillatory and negative traction

It is verified from Eq. (5.8) that the acceleration of the upper cohesive zone faces can be either positive or negative. Thus negative traction $S_y(x)$ surrounding the cohesive zone emerges at higher crack speed ($V \approx 0.4C_s$), as shown in Fig. 5.4-5.7. In Fig. 5.4-5.7, traction $S_y(x)$ is calculated in the case that $c' = 0.5c$ at different crack speed for various T-S law parameters. Although traction distribution is quite smooth as shown in Fig. 5.4 for the strain softening model with $u_0 = 0$, traction oscillation at higher crack speed ($V \approx 0.4C_s$) is found for strain hardening-softening models in Fig. 5.5-5.7. In addition, from Fig. 5.4-5.7 it is seen that when crack speed exceeds a certain critical value, the outer traction surrounding cohesive zone may become negative. This critical value of crack speed depends on the T-S law parameters.

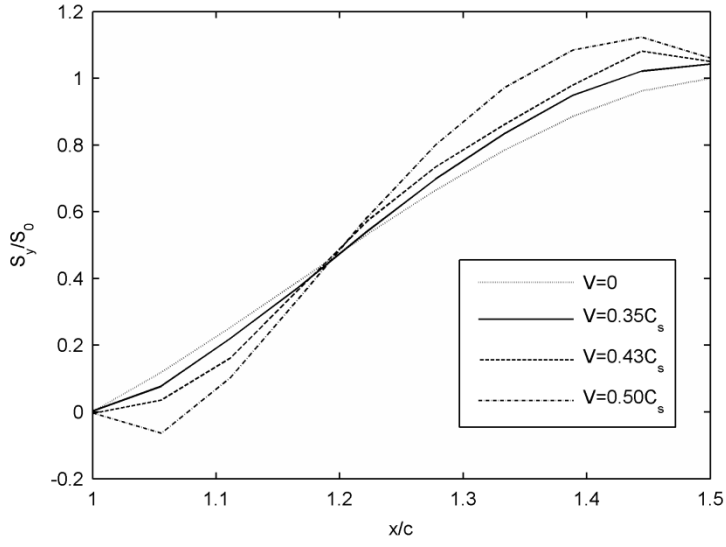

Fig. 5.4 Traction distributions $S_y(x)$ surrounding cohesive zone at different crack speed V when the cohesive zone thickness parameter $b = c'$, and the relative length of cohesive zone is given by $c' = 0.5c$, using a strain softening model with $u_0 = 0$.

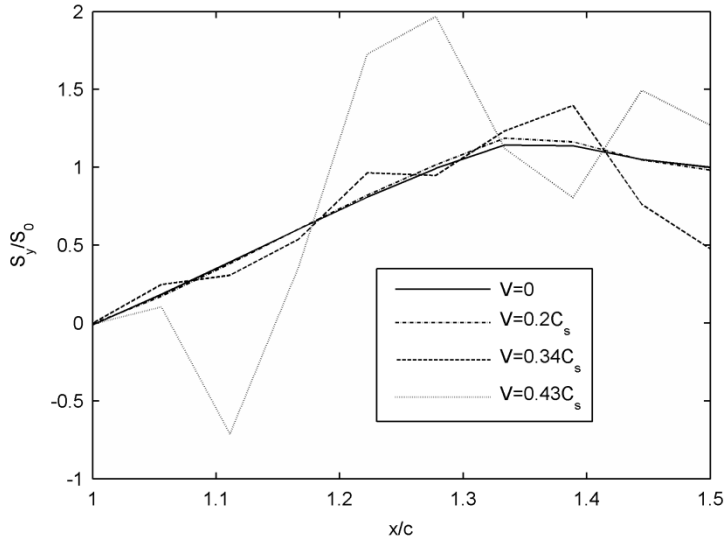

Fig. 5.5 Traction distributions $S_y(x)$ surrounding cohesive zone at different crack speed V when the cohesive zone thickness parameter $b = c'$, and the relative length of cohesive zone is given by $c' = 0.5c$, using a strain hardening-softening model with $u_0 = 0.1u_y(c)$, $S_{max}=1.2S_0$.

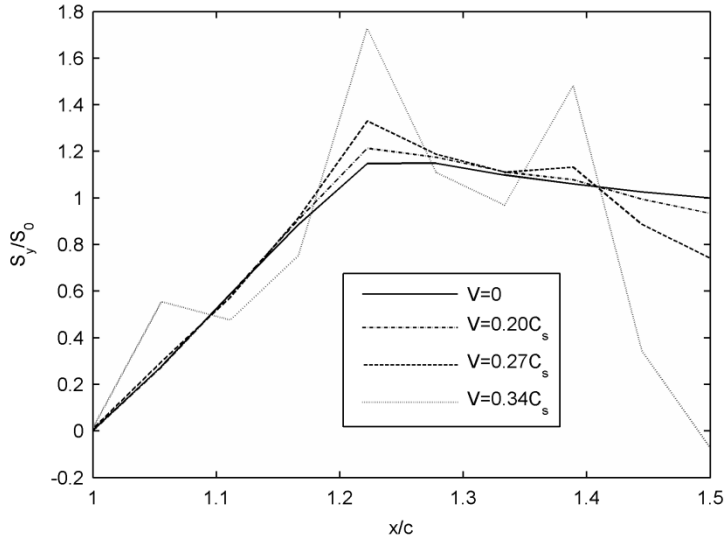

Fig. 5.6 Traction distributions $S_y(x)$ surrounding cohesive zone at different crack speed V when the cohesive zone thickness parameter $b = c'$, and the relative length of cohesive zone is given by $c' = 0.5c$, using a strain hardening-softening model with $u_0 = 0.3u_y(c)$, $S_{max}=1.2S_0$.

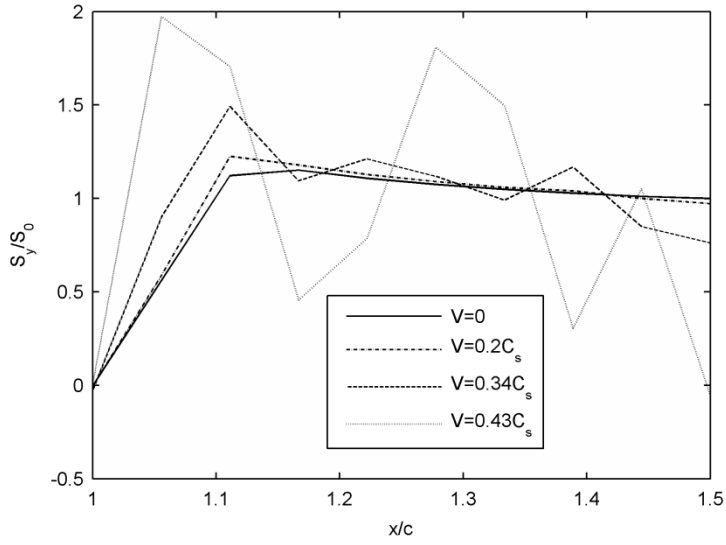

Fig. 5.7 Traction distributions $S_y(x)$ surrounding cohesive zone at different crack speed V when the cohesive zone thickness parameter $b = c'$, and the relative length of cohesive zone is given by $c' = 0.5c$, using a strain hardening-softening model with $u_0 = 0.5u_y(c)$, $S_{max}=1.2S_0$.

5.5.3 The effect of crack speed on the remote loading and cohesive zone length

For a given relative length of cohesive zone, the remote loading T depends on the crack speed. The variation of remote loading T at different crack speed is calculated in the case that $c' = 0.5c$ and shown in Fig. 5.8. From Fig. 5.8 it is seen that, different from the existing cohesive zone models (with ignored inertia of cohesive zone) which gives a constant T/S_0 at different crack speed (Kanninen, 1968), the present model predicts that T/S_0 increases with increasing crack speed V for all T-S law parameters. This speed-dependence of T/S_0 is attributed to increasing traction with increasing crack speed, as a result of the inertia effect of cohesive zone. Consequently, the present model predicts that, under a constant remote loading, the cohesive zone length decreases with increasing crack speed, in agreement with the existing cohesive zone model for a self-similar expanding crack (Atkinson, 1968; Embley and Sih, 1972).

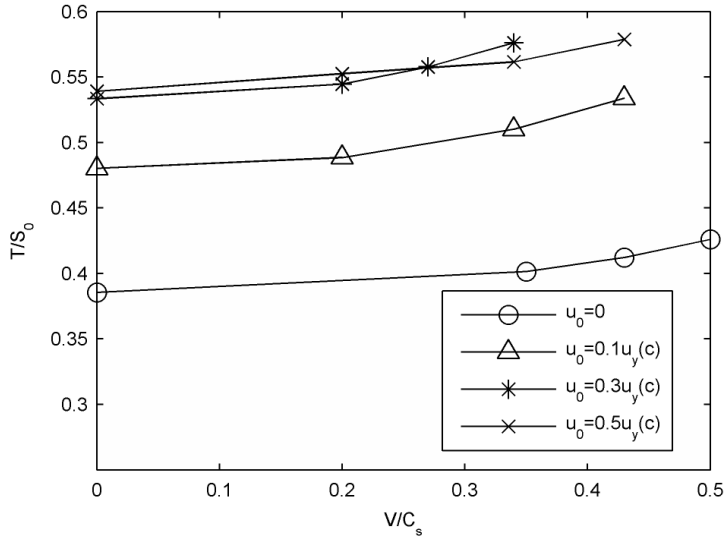

Fig. 5.8 Variations of remote loading T at different crack speed V when the cohesive zone thickness parameter $b = c'$, and the relative length of cohesive zone is given by $c' = 0.5c$.

5.5.4. The inertia effect on dynamic fracture energy

What is of major interest is the inertia effect of cohesive zone on speed-dependent fracture energy. From Eq. (5.10), it is evident that the present model reduces to the traditional cohesive zone model when $b = 0$. In this section, the inertia effect of cohesive zone is studied by examining the speed-dependent fracture energy as a function of the cohesive zone thickness parameter b.

To study fracture energy of steady-state cracking, a critical condition for steady-state crack propagation is needed. In (Kubair et al., 2002; Zhang et al., 2003), the crack propagates steadily when $u_y(c)$ reaches a critical value. Thus, in the present paper, the fracture energy are calculated based on the steady-state crack propagation condition: $u_y(c) = 0.008c'_0$ (Zhang et al., 2003), where c'_0 is the cohesive zone length at $V = 0$, and $c'_0 = 0.5c$ and $c'_0 = 0.5c$ are used in this calculation (our calculation shows that the choose of c'_0 has negligible influence on the numerical results, as shown in Fig. 5.9a and 5.9b). The numerical results are shown in Fig. 5.9a and 5.9b with the strain softening model with $u_0 = 0$. In Fig. 5.9a and 5.9b, initial yielding traction S_0 at variable crack speed is calculated from Eq. (3.35) in chapter 3 and $\mu/Y = 20$ is used, where Y is the yielding stress of material. From Fig. 5.9a and 5.9b, it is seen that, as a result of the inertia effect of cohesive zone, the dynamic fracture energy G predicted by the present model

first varies gently with increasing crack speed at lower speed. However, when the crack speed approaches a critical value, the fracture energy predicted by the present model increases dramatically and becomes practically infinite (10 times larger than static fracture energy G_0), which could define a limiting terminal crack speed in dynamic fracture (Lee and Prakash, 1998; Zhou et al., 2005). In particular, this limiting crack speed decreases with increasing cohesive zone thickness parameter b. On the other hand, when the inertia effect of the cohesive zone is ignored and thus $b = 0$, the predicted fracture energy will decrease with increasing crack speed and a finite limiting crack speed does not exist, as shown in Fig. 5.9a and 5.9b.

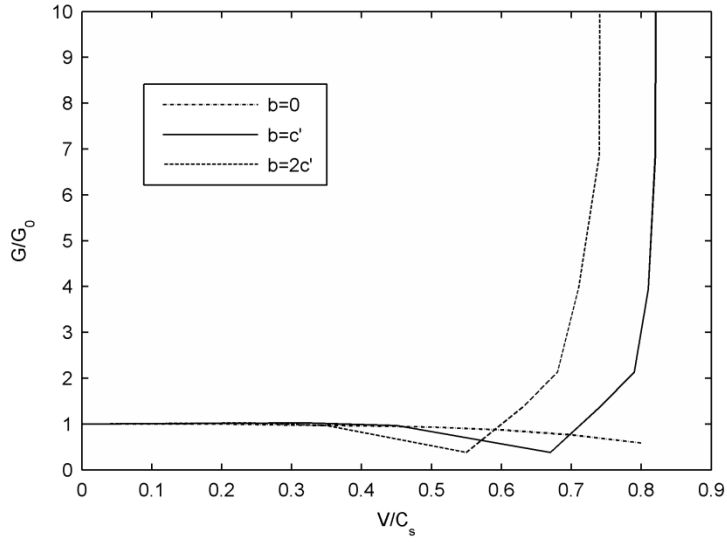

Fig. 5.9a Fracture energy G calculated by the present model based on different cohesive zone thickness parameter b using a strain softening model with $u_0 = 0$, when $c'_0 = 0.5c$. G_0 is the fracture energy at $V = 0$.

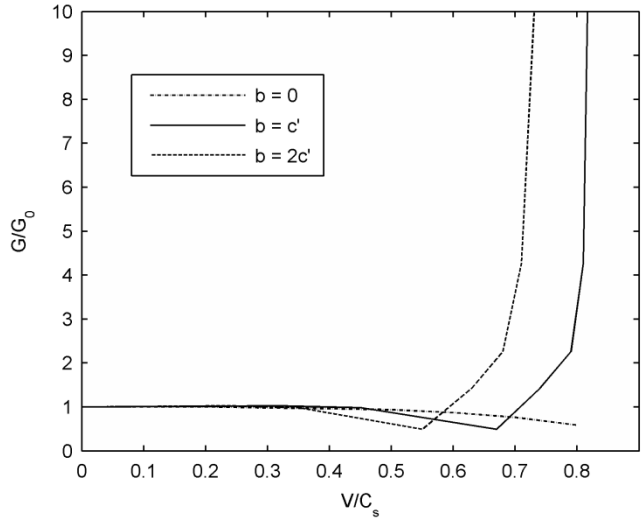

Fig. 5.9b Fracture energy G calculated by the present model based on different cohesive zone thickness

parameter b using a strain softening model with $u_0 = 0$, when $c'_0 = 0.3c$.

It is worth notice that the dramatically increasing fracture energy at high crack speed predicted by the present model agrees qualitatively with experimental observations (Rosakis and Zehnder, 1985; Zhou et al., 2005) although the specific value of the limiting crack speed predicted by the simplified present model, which is about $0.7C_s$ when $b = 2c'$, is slightly higher than the experimental data (about $0.6C_s$ for PMMA and $0.4C_s$ for structural steels) (Rosakis and Zehnder, 1985; Zhou et al., 2005). This indicates that the inertia effect of cohesive zone, as depicted in the present model, could play an essential role at high-speed crack propagation.

5.6 Conclusions

All existing cohesive zone models have assumed cohesive zone as a line segment and ignored mass and inertia of the cohesive zone. The present work proposed a simple mass-spring model to examine the inertia effect of cohesive zone on a high-speed moving crack. A bilinear T-S (traction-separation) law is employed inside the cohesive zone, and the mass distribution of cohesive zone is defined by a simple function so that traction remains finite at the ends of cohesive zone. Our results show that, as a consequence of the inertia of cohesive zone, the fracture energy predicted by the present model increases dramatically when a critical value of crack speed is approached, which could define a limiting terminal crack speed above that fracture energy practically tends to infinity. Agreement of these predictions with known experimental observations suggests that the present model has the potential to catch inertia effects of cohesive zone on a high-speed moving crack.

Chapter 6: Conclusions and future works

6.1 Conclusions

In this thesis, new theoretical models are developed to study the speed effect on moving cracks in nonlinear and ductile materials. The main conclusions of this research are summarized below:

1) A hyperelastic model is employed to study a mode-I steadily moving crack in a finite strain compressible material under plane strain condition. The asymptotic crack tip stress and deformation fields are derived up to the third order to meet the condition for strict positivity of Jacobian determinant. Results show that:

1.1) the near tip crack face profiles at different crack speed predicted by the present model are in good agreement with experimental data for a nonlinear gel material;

1.2) the fracture energy and its dependence on the crack speed predicted by the present model are in reasonable agreement with those given by several existing nonlinear elastic models;

1.3) crack branching angle at high crack speed predicted by the present model is in reasonable agreement with some known experimental data which cannot be explained by the classical Yoffe's solution based on linear elastic fracture mechanics.

2) A modified cohesive zone model is presented to study the speed effect on a mode-I Yoffe-type steady-state moving crack of constant length. Main features of this new model and associated results are:

2.1) instead of assuming the traction force in cohesive zone to be equal to the yielding stress of material, the present modified model predicts a speed-dependent traction force determined by the specific yielding criterion imposed in the cohesive zone;

2.2) strain hardening in cohesive zone is studied by assuming a non-uniform traction distribution given by an unknown polynomial to be determined as part of the solution;

2.3) the present model predicts that the normal traction force decreases with increasing crack speed under lower or moderate remote mode-I loading. As a consequence, unlike the classical Dugdale model of a moving crack which predicts a speed-independent cohesive zone length, the present model predicts that the cohesive zone length increases with increasing crack speed under lower or moderate remote mode-I loading;

2.4) comparison with some known experimental data shows that fracture energy at high crack speed given by the present model is in more reasonable agreement with experiments than the classical Dugdale model of a moving crack.

3) The modified cohesive zone model is further extended to the basic problem of a mode-I self-similar expanding crack. The results obtained show that:

3.1) the normal stress component parallel to the crack faces, which has been ignored in all previous related cohesive zone models, is even larger than the normal traction on the cohesive zone at high crack speed, which justifies the necessity of including the normal stress parallel to the crack faces in the yielding condition in the cohesive zone;

3.2) the present modified model predicts a larger cohesive zone length and CTOD at high crack speed as compared to the classical Dugdale model of a self-similar expanding crack;

3.3) strain hardening effect is studied with a non-uniform traction distribution in cohesive zone which is solved numerically by replacing the continuous traction distribution by a group of step functions, and the accuracy of this method is verified by good agreement with known analytic results in the case of static cracks.

3.4) the dependence of traction on crack speed near a self-similar expanding crack tip is similar to the one near the tip of a Yoffe-type steady-state moving crack of constant length.

4) A simple mass-spring model is presented to examine the inertia effect of cohesive zone on a high-speed mode-I Yoffe-type moving crack. Main results include:

4.1) instead of ignoring the mass and inertia of cohesive zone, in the present model, the

mass distribution of cohesive zone is defined by a simple function which ensures that traction remains finite at the ends of cohesive zone;

4.2) the fracture energy predicted by the present model increases dramatically when a finite critical value of crack speed is approached, which could define a limiting terminal crack speed above that fracture energy practically tends to infinity;

4.3) the predicted values of limiting crack speed are in reasonable agreement with some known experimental data. This remarkable agreement of theoretical predictions with known experimental observations suggests that the present model has the potential to catch inertia effect of cohesive zone on a high-speed moving crack.

In summary, to study the speed-effect of moving cracks and its implication to dynamic fracture, different types of nonlinear models for specific materials are employed or modified in the present research. Compared with existing models, high-speed effects are accounted more carefully in the present models and some results predicted by the present models provide plausible explanations for some important phenomena of dynamic fracture at high crack speed which have not been well explained by the existing models. The main achievements in the thesis are: 1) crack branching in brittle fracture is explained by a hyperelastic model and the predicted branching angle is in good agreement with experimental data; 2) in modified cohesive zone models, the relation between normal traction and crack speed is addressed and the obtained fracture energy is shown in good agreement with experimental data; 3) dramatically increasing fracture energy at high crack speed is explained by a new proposed cohesive zone model which considered the inertia effect of the cohesive zone and the predicted crack limiting speed is in reasonable agreements with experimental data. Therefore, theoretical models presented and numerical results achieved in this thesis contribute new ideas and insights into the study of high-speed dynamic fracture of nonlinear and ductile materials. It is hoped that the present study has the potential to stimulate further research interest in high-speed dynamic fracture of nonlinear and ductile materials.

However, in the present research, strain-rate effects are not considered, so the results achieved in this thesis may not be relevant for materials in which strain-rate effects dominate. And strip-yielding condition is assumed in the present thesis for ductile materials.

6.2 Future works

Based on research results achieved in the present thesis, the following topics are recommended for further studies:

1) **Study the asymptotic field near a moving oblique crack tip in a hyperelastic material:**

How to extend the asymptotic approach in chapter 2 to a moving oblique crack under mixed mode loading raises an interesting subject.

2) **Apply the modified speed-dependent cohesive zone model in numerical simulations of high-speed moving cracks**:

Chapter 3 and 4 have shown that the inertia effect of bulk materials significantly influences the traction in cohesive zone at high crack speed. Thus, a modified speed-dependent cohesive zone model was presented for a Yoffe-type steady-state moving crack and a self-similar expanding crack in chapter 3 and 4, respectively, and the predicted speed-dependent fracture energy is in better agreement with experimental data than the classical Dugdale model. It is of great interest to further extend the analytic model presented in chapter 3 and 4 to numerical simulations of high-speed moving cracks in ductile materials.

3) **Further explore the inertia effect of cohesive zone on high-speed moving cracks**:

Chapter 5 has shown that the inertia of cohesive zone leads to a limiting crack speed above

that the fracture energy practically tends to infinity. To better understand the effect of inertia of cohesive zone on high-speed moving cracks, further studies are suggested:

3.1) study the influence of mass distribution of cohesive zone: in chapter 5, mass distribution of cohesive zone is given by a simple elliptical function. It is of great interest to study the effect of different mass distributions of cohesive zone on speed-dependent fracture energy for high-speed moving cracks;

3.2) study inertia effect of cohesive zone for other types of moving cracks: the Yoffe-type moving crack of constant length employed in chapter 5 is a simplified model, how to extend the new model proposed in chapter 5 to a semi-infinite steady-state moving crack or a self-similar expanding crack raises an interesting and challenging subject for future study.

4) **Study the effect of other factors on high-speed moving cracks**:

For example, chapter 3 and 4 have shown that the non-singular T-stress influences the traction and fracture energy in cohesive zone. Therefore, the role of other factors in high-speed fracture of ductile materials, such as T-stress and material anisotropy, could be explored in future studies.

Reference

Adams, M.J., Allan, A., Briscoe, B.J., Doyle, P.J., Gorman, D.M., Johnson, S.A., 2001. An experimental study of the nano-scratch behaviour of poly (methyl methacrylate). Wear 251, 1579-1583.

Alpa, G., Bozzo, E., Gambarotta, L., 1979. Validity limits of the Dugdale model for thin cracked plates under biaxial loading. Engng. Fract. Mech. 12, 523-529.

Anthony, S.R., Chubb, J.P., Congleton, J., 1970. The crack-branching velocity. Philos. Mag. 22, 1201-1216.

Atkinson, C., 1968. A simple model of relaxed expanding crack. Ark. Fys. 35, 469-476.

Atkinson, C., Kanninen, M.F., 1977. A simple representation of crack tip plasticity: the inclined strip yield superdislocation model. Int. J. Fract. 13, 151-163.

Barenblatt, G.I., 1959. The formation of equilibrium cracks during brittle fracture. General ideas and hypotheses. Axially-symmetric cracks. J. Appl. Math. Mech. 23, 622-636.

Baumberger, T., Caroli, C., Martina, D., 2006. Solvent control of crack dynamics in a reversible hydrogel. Nat. Mater. 5, 552-555.

Becker, W., Gross, D., 1988. About the Dugdale crack under mixed mode loading. Int. J. Fract. 37, 163-170.

Bhargava, R., Bansal, P., 2002. Crack Arrest Model for a Plate Weakened by Internal and External Cracks-a Modified Dugdale Approach. Mech. Compos. Mater. 38, 429-434.

Bouchbinder, E., Livne, A., Fineberg, J., 2008. Weakly nonlinear theory of dynamic fracture. Phys. Rev. Lett. 101, 264302.

Bouchbinder, E., Livne, A., Fineberg, J., 2010. Weakly nonlinear fracture mechanics: experiments and theory. Int. J. Fract. 162, 3-20.

Broberg, K.B., 1960. The propagation of a brittle crack. Ark. Fys. 18, 159-192.

Brown, J.W., Churchill, R.V., 1996. Complex variables and applications. McGraw-Hill, New York.

Bucaille, J.-L., Gauthier, C., Felder, E., Schirrer, R., 2006. The influence of strain hardening of polymers on the piling-up phenomenon in scratch tests: experiments and numerical modelling. Wear 260, 803-814.

Costanzo, F., Walton, J.R., 2002. Steady growth of a crack with a rate and temperature sensitive cohesive zone. J. Mech. Phys. Solids 50, 1649-1679.

Cotterell, B., 1965. On brittle fracture paths. Int. J. Fract.Mech. 1, 96-103.

Craggs, J.W., 1960. On the propagation of a crack in an elastic-brittle material. J. Mech. Phys. Solids 8, 66-75.

Craggs, J.W., 1963. Fracture criteria for use in continuum mechanics, in: Drucker, D.C., Gliman, J.J. (Ed.), Fracture of solids. Wiley, New York, pp. 51-63.

Daniewicz, S.R., 1994. A closed-form small-scale yielding collinear strip yield model for strain hardening materials. Engng. Fract. Mech. 49, 95-103.

Döll, W., 1983. Optical interference measurements and fracture mechanics analysis of crack tip craze zones, Crazing in Polymers. Springer, pp. 105-168.

Dugdale, D.S., 1960. Yielding of steel sheets containing slits. J. Mech. Phys. Solids 8, 100-104.

Edwards, J.R., McRae, D.S., 1993. Nonlinear relaxation/quasi-Newton algorithm for the compressible Navier-Stokes equations. AIAA. J. 31, 57-60.

Embley, G.T., Sih, G.C., 1972. Plastic flow around an expanding crack. Engng. Fract. Mech. 4, 431-442.

England, A., 1965. A crack between dissimilar media. J. Appl. Mech. 32, 400-402.

Freund, L.B., 1990. Dynamic fracture mechanics. Cambridge University Press, Cambridge.

Georgiadis, H.G., 1991. An integral equation approach to self-similar plane-elastodynamic crack problems. J. Elast. 25, 17-30.

Geubelle, P.H., 1995. Finite deformation effects in homogeneous and interfacial fracture. Int. J. Solids Struct. 32, 1003-1016.

Geubelle, P.H., Knauss, W.G., 1994. Finite strains at the tip of a crack in a sheet of

hyperelastic material: I. Homogeneous case. J. Elast. 35, 61-98.

Goodier, J.N., Field, F.A., 1963. Plastic energy dissipation in crack propagation, in: Drucker, D.C., Gliman, J.J. (Eds.), Fracture of solids. Wiley, New York, pp. 103-118.

Gurson, A.L., 1977. Continuum theory of ductile rupture by void nucleation and growth: Part I—Yield criteria and flow rules for porous ductile media. J. Eng. Mater. Technol. 99, 2-15.

Harrop, L.P., 1978. Application of a modified Dugdale model to the K vs COD relation. Engng. Fract. Mech. 10, 807-816.

Hildebrand, F.B., 1987. Introduction to numerical analysis. Courier Dover Publications.

Irwin, G.R., 1957. Analysis of stresses and strains near the end of a crack traversing a plate. J. Appl. Mech. 24, 361-364.

Iserles, A., 2009. A first course in the numerical analysis of differential equations. Cambridge University Press.

Isherwood, D.P., Williams, J.G., 1970. The effect of stress-strain properties on notched tensile failure in plane stress. Engng. Fract. Mech. 2, 19-35.

Jayadevan, K.R., Narasimhan, R., Ramamurthy, T.S., Dattaguru, B., 2003. The effect of T-stress on plane strain dynamic crack growth in elastic–plastic materials. Fatigue Fract. Engng. Mater. Struct. 26, 647-660.

John, F., 1960. Plane strain problems for a perfectly elastic material of harmonic type. Commun. Pure Appl. Math. 13, 239-296.

Kanninen, M.F., 1968. An estimate of the limiting speed of a propagating ductile crack. J. Mech. Phys. Solids 16, 215-228.

Knowles, J.K., Sternberg, E., 1975. On the singularity induced by certain mixed boundary conditions in linearized and nonlinear elastostatics. Int. J. Solids Struct. 11, 1173-1201.

Knowles, J.K., Sternberg, E., 1983. Large deformations near a tip of an interface-crack between two Neo-Hookean sheets. J. Elast. 13, 257-293.

Kubair, D.V., Geubelle, P.H., Huang, Y.Y., 2002. Analysis of a rate-dependent cohesive model for dynamic crack propagation. Engng. Fract. Mech. 70, 685-704.

Lang, S., 1999. Complex analysis. Springer.

Lee, Y., Prakash, V., 1998. Dynamic fracture toughness versus crack tip speed relationship at lower than room temperature for high strength 4340VAR structural steel. J. Mech. Phys. Solids 46, 1943-1968.

Li, X., Steigmann, D.J., 1993. Finite plane twist of an annular membrane. Q. J. Mech. Appl. Math. 46, 601-625.

Livne, A., Bouchbinder, E., Svetlizky, I., Fineberg, J., 2010. The near-tip fields of fast cracks. Science 327, 1359-1363.

Lu, T.J., Chow, C.L., 1990. A modified Dugdale model for crack tip plasticity and its related problems. Engng. Fract. Mech. 37, 551-568.

Mooney, M., 1940. A Theory of Large Elastic Deformation. J. Appl. Phys. 11, 582-592.

Murphy, N., Ali, M., Ivankovic, A., 2006. Dynamic crack bifurcation in PMMA. Engng. Fract. Mech. 73, 2569-2587.

Needleman, A., 1987. A continuum model for void nucleation by inclusion debonding. J. Appl. Mech. 54, 525-531.

Neimitz, A., 2004. Modification of Dugdale model to include the work hardening and in-and out-of-plane constraints. Engng. Fract. Mech. 71, 1585-1600.

Ramulu, M., Kobayashi, A.S., Kang, B.S.-J., 1982. Dynamic crack curving and branching in line-pipe. J. Pressure Vessel Technol. 104, 317-322.

Ramulu, M., Kobayashi, A.S., Kang, B.S.-J., 1984. Dynamic Crack Branching—A Photoelastic Evaluation, Fracture Mechanics: Fifteen Symposium. Ed. by RJ Sanford. ASTM STP, pp. 130-148.

Rice, J.R., 1968. Mathematical analysis in the mechanics of fracture, in: Liebowitz, H. (Ed.), Fracture: an advanced treatise. Academic Press, New york, pp. 191-311.

Rice, J.R., 1974. Limitations to the small scale yielding approximation for crack tip plasticity. J. Mech. Phys. Solids 22, 17-26.

Rivlin, R.S., 1948. Large elastic deformations of isotropic materials. IV. Further

developments of the general theory. Philosophical Transactions of the Royal Society of London. Series A, Mathematical and Physical Sciences 241, 379-397.

Rosakis, A.J., Freund, L.B., 1982. Optical measurement of the plastic strain concentration at a crack tip in a ductile steel plate. J. Eng. Mater. Technol. 104, 115-120.

Rosakis, A.J., Zehnder, A.T., 1985. On the dynamic fracture of structural metals. Int. J. Fract. 27, 169-186.

Ru, C.Q., 1997. Finite strain singular field near the tip of a crack terminating at a material interface. Math. Mech. Solids 2, 49-73.

Ru, C.Q., 2002. On complex-variable formulation for finite plane elastostatics of harmonic materials. Acta Mech. 156, 219-234.

Scheider, I., 2009. Derivation of separation laws for cohesive models in the course of ductile fracture. Engng. Fract. Mech. 76, 1450-1459.

Siegmund, T., Brocks, W., 2000. A numerical study on the correlation between the work of separation and the dissipation rate in ductile fracture. Engng. Fract. Mech. 67, 139-154.

Sousa, R.A., Castro, J.T.P., Lopes, A.A.O., Martha, L.F., 2013. On improved crack tip plastic zone estimates based on T-stress and on complete stress fields. Fatigue Fract. Engng. Mater. Struct. 36, 25-38.

Tanaka, Y., Fukao, K., Miyamoto, Y., 2000. Fracture energy of gels. Eur. Phys. J. E 3, 395-401.

Tarantino, A.M., 2005. Crack propagation in finite elastodynamics. Math. Mech. Solids 10, 577-601.

Theocaris, P.S., Gdoutos, E.E., 1974. The modified Dugdale-Barenblatt model adapted to various fracture configurations in metals. Int. J. Fract. 10, 549-564.

Tvergaard, V., Hutchinson, J.W., 1994. Effect of T-stress on mode I crack growth resistance in a ductile solid. Int. J. Solids Struct. 31, 823-833.

Varley, E., Cumberbatch, E., 1980. Finite deformations of elastic materials surrounding cylindrical holes. J. Elast. 10, 341-405.

Vitek, V., 1976. Yielding on inclined planes at the tip of a crack loaded in uniform tension. J. Mech. Phys. Solids 24, 263-275.

Volokh, K.Y., 2004. Comparison between cohesive zone models. Commun. Numer. Methods Engng. 20, 845-856.

Williams, J.G., Ewing, P.D., 1972. Fracture under complex stress—the angled crack problem. Int. J. Fract.Mech. 8, 441-446.

Williams, J.G., Hadavinia, H., 2002. Analytical solutions for cohesive zone models. J. Mech. Phys. Solids 50, 809-825.

Williams, M.L., 1957. On the stress distribution at the base of a stationary crack. J. Appl. Mech. 24, 109-114.

Wnuk, M.P., Legat, J., 2002. Work of fracture and cohesive stress distribution resulting from triaxiality dependent cohesive zone model. Int. J. Fract. 114, 29-46.

Wnuk, M.P., Mura, T., 1983. Effect of microstructure on the upper and lower limits of material toughness in elastic-plastic fracture. Mech. Mater. 2, 33-46.

Wu, K.C., Huang, S.M., 2013. Dugdale model for an expanding crack under shear stress. Engng. Fract. Mech. 104, 198-207.

Xu, X.-P., Needleman, A., 1994. Numerical simulations of fast crack growth in brittle solids. J. Mech. Phys. Solids 42, 1397-1434.

Yao, Y., Huang, Z., 2011. A new nonlocal cohesive stress law and its applicable range. Engng. Fract. Mech. 78, 1101-1113.

Yoffe, E.H., 1951. LXXV. The moving griffith crack. Philos. Mag. 42, 739-750.

Zehnder, A., Rosakis, A., 1990. Dynamic fracture initiation and propagation in 4340 steel under impact loading. Int. J. Fract. 43, 271-285.

Zhang, X., Mai, Y.-W., Jeffrey, R.G., 2003. A cohesive plastic and damage zone model for dynamic crack growth in rate-dependent materials. Int. J. Solids Struct. 40, 5819-5837.

Zhou, F., Molinari, J.-F., Shioya, T., 2005. A rate-dependent cohesive model for simulating dynamic crack propagation in brittle materials. Engng. Fract. Mech. 72, 1383-1410.

Appendix A

Here, we prove that Eq. (3.23) in chapter 3 is the general solution of (3.22) for any real polynomial traction force $P(x)$ of finite degree n given in Eq. (3.18). Actually, it is well known (Rice, 1968) that the general solution of Riemann-Hilbert problem (3.22) is given by

$$-\left(1+\beta_2^2\right)\Phi'(z)+2\beta_2\Psi'(z)=\frac{1}{i2\pi\sqrt{z^2-(c+c')^2}}\int_{-c-c'}^{c+c'}\frac{\left[\sqrt{x^2-(c+c')^2}\right]^+ 2P(x)H(|x|-c)}{x-z}\mathrm{d}x+\frac{R_3(z)}{\sqrt{z^2-(c+c')^2}} \tag{A.1}$$

where, $R_3(z)$ is an arbitrary polynomial with complex coefficients, to be determined by remote conditions imposed at infinity, and within the interval from $(-c-c')$ to $(c+c')$,

$$\left[\sqrt{x^2-(c+c')^2}\right]^+ = i\sqrt{(c+c')^2-x^2} \tag{A.2}$$

To evaluate the integral on RHS of (A.1) with an arbitrary real polynomial $P(x)$, first, we notice that

$$\begin{aligned}\int\frac{\sqrt{(c+c')^2-x^2}\,2A_0}{x-z}\mathrm{d}x &= 2A_0\left\{\sqrt{(c+c')^2-x^2}-z\arctan\frac{x}{\sqrt{(c+c')^2-x^2}}\right.\\ &\left.-\sqrt{(c+c')^2-z^2}\ln\left[\frac{-2xz+2(c+c')^2+2\sqrt{(c+c')^2-z^2}\sqrt{(c+c')^2-x^2}}{x-z}\right]\right\}\\ &=\left\{2A_0g_0(x)+f_0(z)h_0(x)-\sqrt{(c+c')^2-z^2}\ln\left[\frac{-2xz+2(c+c')^2+2\sqrt{(c+c')^2-z^2}\sqrt{(c+c')^2-x^2}}{x-z}\right]\right\}\end{aligned} \tag{A.3}$$

where $g_0(x)$ and $h_0(x)$ are two real bounded functions of x, $f_0(z)$ is a real polynomial of z, and specific forms of $g_0(x)$, $h_0(x)$ and $f_0(z)$ are not important for our purpose. Now, in order to use mathematical induction, let us assume that

$$\int \frac{\sqrt{(c+c')^2 - x^2}\, 2A_{n-1}x^{n-1}}{x-z}\mathrm{d}x = 2A_{n-1}\left[g_{n-1}(x) + f_{n-1}(z)h_{n-1}(x)\right]$$
$$-2A_{n-1}z^{n-1}\left\{\sqrt{(c+c')^2 - z^2}\,\ln\left[\frac{-2xz + 2(c+c')^2 + 2\sqrt{(c+c')^2 - z^2}\sqrt{(c+c')^2 - x^2}}{x-z}\right]\right\} \quad \text{(A.4)}$$

where $g_{n-1}(x)$ and $h_{n-1}(x)$ are two real bounded functions of x, $f_{n-1}(z)$ is a real polynomial of z. Thus it can be shown that

$$\int \frac{\sqrt{(c+c')^2 - x^2}\, 2A_n x^n}{x-z}\mathrm{d}x = x\int \frac{\sqrt{(c+c')^2 - x^2}\, 2A_n x^{n-1}}{x-z}\mathrm{d}x - \int\int \frac{\sqrt{(c+c')^2 - x^2}\, 2A_n x^{n-1}}{x-z}\mathrm{d}x\mathrm{d}x$$
$$= 2A_n x\left[g_{n-1}(x) + f_{n-1}(z)h_{n-1}(x)\right]$$
$$-2A_n xz^{n-1}\left\{\sqrt{(c+c')^2 - z^2}\,\ln\left[\frac{-2xz + 2(c+c')^2 + 2\sqrt{(c+c')^2 - z^2}\sqrt{(c+c')^2 - x^2}}{x-z}\right]\right\}$$
$$-2A_n\left[\int g_{n-1}(x)\mathrm{d}x + f_{n-1}(z)\int h_{n-1}(x)\mathrm{d}x\right]$$
$$+2A_n z^{n-1}\sqrt{(c+c')^2 - z^2}\left\{x\ln\left[\frac{-2xz + 2(c+c')^2 + 2\sqrt{(c+c')^2 - z^2}\sqrt{(c+c')^2 - x^2}}{x-z}\right]\right.$$
$$\left. -z\ln\left[\frac{-2xz + 2(c+c')^2 + 2\sqrt{(c+c')^2 - z^2}\sqrt{(c+c')^2 - x^2}}{x-z}\right] + \sqrt{(c+c')^2 - z^2}\,\arctan\frac{x}{\sqrt{(c+c')^2 - x^2}}\right\}$$
$$= 2A_n\left[g_n(x) + f_n(z)h_n(x)\right]$$
$$-2A_n z^n\left\{\sqrt{(c+c')^2 - z^2}\,\ln\left[\frac{-2xz + 2(c+c')^2 + 2\sqrt{(c+c')^2 - z^2}\sqrt{(c+c')^2 - x^2}}{x-z}\right]\right\}$$

(A.5)

where $g_n(x)$ and $h_n(x)$ are two real bounded functions of x, $f_n(z)$ is a real polynomial of z. Thus, on using mathematical induction, it follows from (A.3-A.5) that

$$\int \frac{\sqrt{(c+c')^2-x^2}\,2P(x)}{x-z}\mathrm{d}x = 2\sum_{i=0}^{n} A_i\left[g_i(x)+f_i(z)h_i(x)\right]$$
$$-2P(z)\left\{\sqrt{(c+c')^2-z^2}\,\ln\left[\frac{-2xz+2(c+c')^2+2\sqrt{(c+c')^2-z^2}\sqrt{(c+c')^2-x^2}}{x-z}\right]\right\} \tag{A.6}$$

where $g_i(x)$ and $h_i(x)$ are two real bounded functions of x, $f_i(z)$ is a real polynomial of z (i = 0,1,2…n).

Now the definite integral on RHS of (A.1) can be written as

$$-\left(1+\beta_2^2\right)\Phi'(z)+2\beta_2\Psi'(z) = \frac{1}{2\pi\sqrt{z^2-(c+c')^2}}\int_{-c-c'}^{-c}\frac{\sqrt{(c+c')^2-x^2}\,2P(x)}{x-z}\mathrm{d}x$$
$$+\frac{1}{2\pi\sqrt{z^2-(c+c')^2}}\int_{c}^{c+c'}\frac{\sqrt{(c+c')^2-x^2}\,2P(x)}{x-z}\mathrm{d}x+\frac{R_3(z)}{\sqrt{z^2-(a+c)^2}} \tag{A.7}$$

Applying the indefinite integral (A.6) to the two definite integrals of (A.7), one gets

$$-\left(1+\beta_2^2\right)\Phi'(z)+2\beta_2\Psi'(z) = \frac{1}{\pi}\frac{\sum_{i=0}^{n} A_i\left[g_i(x)\big|_{-c-c'}^{-c}+g_i(x)\big|_{c}^{c+c'}+f_i(z)h_i(x)\big|_{-c-c'}^{-c}+f_i(z)h_i(x)\big|_{c}^{c+c'}\right]}{\sqrt{z^2-(c+c')^2}}$$
$$+\frac{1}{\pi i}P(z)\left(i\pi+\ln\frac{\left[-2cz+2(c+c')^2-2i\sqrt{z^2-(c+c')^2}\sqrt{(c+c')^2-c^2}\right](-c-z)}{\left[2cz+2(c+c')^2-2i\sqrt{z^2-(c+c')^2}\sqrt{(c+c')^2-c^2}\right](c-z)}\right)+\frac{R_3(z)}{\sqrt{z^2-(c+c')^2}} \tag{A.8}$$

It can be verified that Eq. (A.8) is valid in entire z plane. Furthermore, Eq. (A.8) can be simplified as

$$-\left(1+\beta_2^2\right)\Phi'(z)+2\beta_2\Psi'(z) = \frac{1}{\pi i}P(z)\left(i\pi+\ln\frac{z\sqrt{(c+c')^2-c^2}-ic\sqrt{z^2-(c+c')^2}}{z\sqrt{(c+c')^2-c^2}+ic\sqrt{z^2-(c+c')^2}}\right)$$
$$+\frac{1}{\pi}\frac{\sum_{i=0}^{n} A_i\left[g_i(x)\big|_{-c-c'}^{-c}+g_i(x)\big|_{c}^{c+c'}+f_i(z)h_i(x)\big|_{-c-c'}^{-c}+f_i(z)h_i(x)\big|_{c}^{c+c'}\right]}{\sqrt{z^2-(c+c')^2}}+\frac{R_3(z)}{\sqrt{z^2-(c+c')^2}} \tag{A.9}$$

Putting the second term into the third terms on RHS of (A.9), we get the general solution Eq.

(3.23), where $Q(z)$ is an arbitrary polynomial of finite degree, and a T-related term has been separated from $Q(z)$ just for convenience. As indicated in the text, it is easily verified that the present solution reduces to the result of classical Dugdale model when $P(x)$ is a constant and reduces to the result of (Harrop, 1978) (see Eq. (7) in (Harrop, 1978)) when $P(x)$ is a quadratic even function of x.

Appendix B

The four coefficients of $Q(z)$ in chapter 3 determined by Eq. (3.28) are

$$
\begin{aligned}
&B_6 = 2\arccos\left(\frac{c}{c+c'}\right)A_6,\quad B_4 = 2\arccos\left(\frac{c}{c+c'}\right)A_4 + \left[c\sqrt{(c+c')^2-c^2} - (c+c')^2\arccos\left(\frac{c}{c+c'}\right)\right]A_6 \\
&B_2 = 2\arccos\left(\frac{c}{c+c'}\right)A_2 + \left[c\sqrt{(c+c')^2-c^2} - (c+c')^2\arccos\left(\frac{c}{c+c'}\right)\right]A_4 \\
&\quad + \left[\frac{c^3\sqrt{(c+c')^2-c^2}}{2} - \frac{c(c+c')^2\sqrt{(c+c')^2-c^2}}{4} - \frac{(c+c')^4}{4}\arccos\left(\frac{c}{c+c'}\right)\right]A_6 \\
&B_0 = 2\arccos\left(\frac{c}{c+c'}\right)A_0 + \left[c\sqrt{(c+c')^2-c^2} - (c+c')^2\arccos\left(\frac{c}{c+c'}\right)\right]A_2 \\
&\quad + \left[\frac{c^3\sqrt{(c+c')^2-c^2}}{2} - \frac{c(c+c')^2\sqrt{(c+c')^2-c^2}}{4} - \frac{(c+c')^4}{4}\arccos\left(\frac{c}{c+c'}\right)\right]A_4 \\
&\quad + \left[\frac{c^5\sqrt{(c+c')^2-c^2}}{3} - \frac{c^3(c+c')^2\sqrt{(c+c')^2-c^2}}{12} - \frac{c(c+c')^4\sqrt{(c+c')^2-c^2}}{8}\right. \\
&\quad \left. - \frac{(c+c')^6}{8}\arccos\left(\frac{c}{c+c'}\right)\right]A_6
\end{aligned}
\tag{B.1}
$$